Title
The Dynamics of Precipitation Variability in the Asian Monsoon

Author
Day, Jesse Alexander

Publication Date
2016

The Dynamics of Precipitation Variability in the Asian Monsoon

by

Jesse Alexander Day

A dissertation submitted in partial satisfaction of the

requirements for the degree of

Doctor of Philosophy

in

Earth and Planetary Science

in the

Graduate Division

of the

University of California, Berkeley

Committee in charge:

Professor Inez Y. Fung, Chair
Assistant Professor David M. Romps
Professor John C. Chiang

Spring 2016

The Dynamics of Precipitation Variability in the Asian Monsoon

Abstract

The Dynamics of Precipitation Variability in the Asian Monsoon

by

Jesse Alexander Day

Doctor of Philosophy in Earth and Planetary Science

University of California, Berkeley

Professor Inez Y. Fung, Chair

The Asian summer monsoon supplies around 3 billion people with much of their yearly supply of freshwater, necessary for human consumption as well as in agriculture and industry. In many regions, particularly along the Ganges River in India and in northern China, use of freshwater far exceeds natural recharge rates. Given the high population density of these regions, a substantial fraction of Asia's population is therefore critically sensitive to interannual changes in the supply of freshwater by the monsoon, as well as potential future change under 21st century warming. This dissertation focuses on understanding the atmospheric dynamics of the leading mode of July-August Asian Monsoon rainfall variability, which links two major subsystems: the South Asian and East Asian monsoons.

In summer, two distinct rainfall régimes are observed: Convective storms over India, Bangladesh and Nepal (the South Asian monsoon), and frontal rainfall over China, Japan and Korea (the East Asian monsoon). In addition, the Himalayas and other orography, including the Arakan Mountains, Ghats and Yunnan Plateau, create smaller precipitation domains separated by sharp gradients. My research has revealed a previously unrecognized mode of continental precipitation variability that spans both South and East Asia during July and August. A dipole between the Himalayan Foothills and the Monsoon Zone of central India dominates July-August interannual variability in South Asia, and is also associated in East Asia with a tripole between the Yangtze Corridor and North and South China. By performing lag-lead correlation of rainfall, I show that this covariation does not correspond to the spatial pattern of July-August storm tracks. Instead, I hypothesize that interannual change in the strength of moisture transport from the Bay of Bengal to the Yangtze Corridor across the northern Yunnan Plateau induces widespread precipitation anomalies. Abundant moisture transport along this route requires both cyclonic monsoon circulation over India and sufficient heating over the Bay of Bengal, which occurs only during July and August, as I also show by analyzing existing runs with a zoomed, nested version of the LMDZ5 model nudged to reanalysis.

In China, a growing body of work identifies a régime shift in rainfall occurring in the late 1970s known as the "South Flood-North Drought." However, this phenomenon has not

previously been described in terms of the complex seasonal cycle of the East Asian monsoon. During the peak interval of rainfall, known as Meiyu season, a persistent but meandering front (the “Meiyu Front”) delivers strong bouts of rainfall over a narrow latitude band. The preferred latitude of this front shifts throughout the year and shifts abruptly from May to July. I have developed an image processing algorithm, the Rainband Detection Algorithm (RDA), that produces a 57-year (1951-2007) daily catalog of frontal rainfall events in China, reporting latitude, intensity and zonal extent. This result allows for a quantitative assessment of Meiyu change between 1951-1979 and 1980-2007, which has never previously been performed on an event-by-event basis. I find that the greatest change in frontal behavior has occurred during May, when events have strongly decreased over the Yangtze River valley. In addition, a statistically significant southward shift has occurred in July-August Meiyu events. The rainfall changes associated with South Flood-North Drought can be attributed specifically to changes in banded rainfall. A suite of alternative simple metrics of China rainfall cannot capture all of the characteristics of the South Flood-North Drought in one succinct measure. Another distinct change occurred between 1979-1993 and 1994-2007 featuring intensification of Meiyu rainbands, possibly reflecting a different causal mechanism. Our RDA catalog is available to other East Asian monsoon researchers.

The leading Asian monsoon mode described in Chapter 2 (hereafter All-Asia EOF1) not only describes a key mode of Asian monsoon variability, but is also associated with climate anomalies across the entire Northern Hemisphere. We find an association between strong All-Asia EOF1 years and the Circumglobal Teleconnection (CGT), a high-latitude standing wave pattern with wavenumber 5 or 6 implicated in Northern Hemisphere heat wave events, which we further investigate through compositing with JRA-55 reanalysis. JRA-55 captures changes in water vapor transport across the Yunnan Plateau associated with All-Asia EOF1 as hypothesized in Chapter 2, and suggests that they correspond to an anomalous band of diabatic heating of amplitude 100 W m^{-2}. We propose that this heating can force the CGT and participates in the phase-locking of the CGT, which is further amplified by the configuration of high topography. Over China and East Asia, All-Asia EOF1 is manifested as a meridional jet shift. Using the RDA catalog from Chapter 3, we test whether rainfall shifts across the entire East Asian monsoon also correspond to jet changes. We find that the South Flood-North Drought robustly corresponds to a southward shift in the East Asian tropospheric jet. Thus, although IPCC5 projections of the 21^{st}-century Asian monsoon remain inconclusive, future changes may be more predictable by further studying the effects of global warming on Bay of Bengal moisture transport, the CGT and the East Asian jet.

Contents

List of Figures

List of Tables

Acknowledgments

Before all else, none of what I have achieved would be possible without the unconditional love of my mom Catherine and my dad Clayton. I consider them the two most exceptional humans I know. They have sacrificed for me and my education in ways that have taken me many years to comprehend. From my first day in California, they have been incessant listeners, believers, reviewers and unpaid editors. I could not have made it this far without you. Finishing this dissertation seems like the least that I can achieve in repayment. I love you both.

Inez has been an incredible mentor. From the first day that I walked into her office, she has believed in my potential even when I had little faith in my own. I believe that Inez is the embodiment of a true scientist, committed to simplicity and truth and to educating the next generation. She has an eagerness to learn and belief in the scientific process that is infectious, and the gift of reducing complex systems to their hidden key filaments. She selflessly dedicates time to others, whether to graduate students from other groups, former students or undeclared undergraduates, all with their best interest in mind and no regard to her own benefit. I have also benefited from Inez's ability to place current research in historical context, explaining the decades of key discoveries and false turns that led to the current consensus. Working with Inez has been a privilege that I will bear with me for the rest of my life. I hope that I can mentor others as she has done for me.

I have benefited from the guidance of many other great scientists. Thank you first to John Chiang. I highly respect your even-keeled approach to scientific discussion and compassionate mentorship. Thank you to David Battisti, Peter Molnar, Shang-Ping Xie, Camille Risi and Yanjun Cai for believing in my work and investing the time to understand my research. I would also like to thank Peter, Marin Clark, Zhisheng An and others for organizing the series of Tibetan Plateau schools and workshops, which provided an essential forum for my development as a scientist. Thank you to David Romps, Walter Alvarez and Phil Marcus for serving as members of my qualifying exam. Thank you to Jun Korenaga, Steve Lamoreaux, Yilong Han and Vinny Manoharan for fostering my first steps in science as an undergraduate. Thank you to Fung alumni Zan Stine and Jung-Eun Lee and to Prabhat for your help and encouragement, and also to my peers Lydia Staisch, Petr Yakovlev, Xiaojuan Liu, Jinqiang Chen and Anna Merrifield.

I would like to thank all of the members of the Fung group over my years at Berkeley. Percy Link, thank you for welcoming me to 301. Thank you to Ju-Mee Ryoo, Stephanie Wuerth, Jiabin Liu, Holly Maness, Michail Vrettas, Meghan Thurlow, Mark Yashar, Octavia Crompton, Teresa Bilir and Jeremy Randolph-Flagg for making McCone a warmer place. Thank you also to the broader Berkeley atmospheric community, in particular Tripti Bhattacharya, Wenwen Kong, my coauthor Jake Edman, Yuwei Liu, Andrew Friedman, Jelena Lukovic, Yoshi Mondal, Nadir Jeevanjee, Jake Seeley, Ben Fildier, Da Yang, Leif Swenson, Megan Vieira, Ben Nault and Xueling Liu. Thank you to our group manager David Elvins for tirelessly helping us, and to Margie Winn and the McCone administrative staff, including Chrystel Catambay, Jann Michael Pandanganan and Nadine Spingola-Hutton.

Thank you to my peers from my incoming EPS class, Shuo Zhang, Andrea Chiang, Carolina Muñoz, Ana Martinez-Poza and Jenn Frederick, and my friends in the department, including David Mangiante, my partner-in-crime Noah Randolph-Flagg, Chelsea 'Charks' Willett, Seth Saltiel, Pam Kaercher, Mong-Han Chen, Daniella Rempe, Mike Antonelli, Jordan Mizerak, Sanne Cottaar, Brent Delbridge, William Hawley, Nick Knezek, Marissa Tremblay, Courtney Sprain, Tom Smart, Liz Mitnick, Alex Bryk, Steve Breen, Hannah Bourne, Elizabeth Niespolo, Laura MacLean, Qingkai Kong, Shuai Zhang, Cheng Cheng, Heidi Fuqua, Jesse Hahm, Chris Johnson, Avinash Nayak, Katie Wooddell, Eloisa Zepeda-Alarcon and many I've omitted, for making the journey to this point much more fun.

Thank you to my friends from Yale who led me to this point. Ian, in the 10+ years since we were freshman roommates, I have fed off of your intellectual curiosity and been inspired to follow your footsteps, first into the physics major, and then to EPS at Berkeley. Robert and Dan, thank you for preserving my sanity as we each navigated the eddies of our respective graduate school experiences. Minh, thank you for your generosity. By inviting me to stay with your family in Saigon in 2007, you set me on the course that eventually led to this dissertation. Thank you also to Yale's Richard U. Light Fellowship for funding me to spend a year in Beijing learning Chinese intensively, during which time I became resolved to use my undergraduate degree in physics on issues of the environment.

As part of my double life as competitive Scrabble player, I belong to an exceptional community of brilliant, fun people who have reminded me of what matters in life even through the hard times. Thanks to XP, KC, Ed, César, James, Kate, Gab, Cecilia, John, Conrad and Doug for reminding me on a weekly basis how lucky I am. Thank you also to the broader community for making me feel welcome no matter where in the world I go.

I would like to thank the University of California-Berkeley's ultimate frisbee B team, better known as Thugmo. Both as teammate and coach, the team allowed me to stay connected to a sport that I love and provided a counterweight to my academic pursuit. Thank you to those that I coached for being good friends, working hard and making my job easy. Thank you to my former students in EPS50, many of whom are already blooming into great scientists. Thank you to my Thai language teacher Supatraa Chowchuvech for treating me as seriously as her other students. Thank you to my surgeon Dr. Bob Eppley and my physical therapist Mike Branzel for allowing me to recover from my torn ACL and meniscus in time for me to pass my qualifying exam. In the same vein, thank you to José, Naso and Jesús for letting me use Caffe Nefeli as my surrogate office during quals prep when being on crutches prevented me from transporting coffee. Thank you also to the fine folks at Stuffed Inn, Hummingbird Cafe and Abe's Cafe for always making me feel welcome no matter how long the absence.

Lastly, thank you to Berkeley's Counseling and Psychological Services division, and in particular to my therapist Amy Honigmann for helping me through the last few years. In an academic climate where 47% of UC Berkeley Ph. D. students report experiencing depression, I feel that it is too important for me not to acknowledge my own struggles, and the love of my family and friends that brought me back to happiness. Finally, my love to Sonya for believing in me and helping me push through to the finish line.

Chapter 1

Introduction

‘The river! The river is coming!’ I shouted, in broken Marathi.

Sensing my distress but not really understanding me, the villagers gathered around and then called Prabaker, plying him with questions.

‘What is your matter, Lin? The people are very upset for you.’

‘The river! It’s coming up fast. It’ll wipe the village out!’

Prabaker smiled.

‘Oh, no, Lin. That will not be happening.’

‘I’m telling you! I’ve seen it. I’m not joking, Prabu. The fucking river’s in flood!’

Prabaker translated my words for the others. Everyone laughed...

The river, only a few hundred meters away, was a deluge: a vast muddy concrescence that tore through the valley in heaving waves and boiling eddies. The rain redoubled its intensity as we stood there, our clothes as drenched as the yielding soil. And still the tumid river grew, consuming new land with each thumping heartbeat.

‘You see those sticks, Lin,’ Prabaker said, in his most irritating attempt at a soothing tone. ‘Those sticks are the flood-game sticks. Do you remember, when the people put them in the ground? Satish and Pandey, Narayan and Bharat...do you remember?’

I did remember. Days before, there’d been a lottery of some kind ... As we stood in the numbing, drumming rain and watched the prowling advance of the river, Prabaker explained that the wooden stakes were part of a flood-game that was played every year. The oldest men in the village, and six lottery winners, were given the chance to predict the point to which the river would rise. Each wooden stick, with its flag of yellow silk, represented a best guess.

‘You see, this one little flag?’ Prabaker asked, pointing to the stake that was furthest from where we stood. ‘This one is almost gone. The river will reach to him, and cover him, tomorrow or tonight.’

He translated what he’d told me for the crowd, and they pushed Satish, a heavy-set cowherd, to the front of the group. The almost submerged stick was his, and he accepted, with shy laughter and downcast eyes, the good-natured jeers of his friends and the sneers of the older men.

> ‘And this one here,’ Prabaker went on, pointing to the stake nearest to our position. ‘This one is the river will never be touching. The river never comes more far than this place. Old Deepakbhai has picked for himself this place, for the putting of his stick. He thinks this year will be a very heavy monsoon ...’
>
> ‘But ... how do you know that the river won’t rise past this point?’
>
> ‘We are here a long time, Lin. Sunder village has been in this place for two thousands of years. The next village, Natinkerra, has been there for much longer, about three thousands of years. In some other places - not near to here - the people do have a bad experiences, with the floods, in monsoon time. But not here. Not in Sunder. Our river has never come to this far. This year, also, I don’t think it will come to this far, even so old Deepakbhai says it will. Everybody knows where the river will stop, Lin.’
>
> Gregory David Roberts, *Shantaram*, 133-135

Clearly, atmospheric dynamicists are not the only ones to engage in the art of monsoon prognostication. Nonetheless, in spite of a century of work, forecasts of present-day monsoon seasonal variability and of future changes under global warming remain nebulous. The purpose of this dissertation is to elucidate the atmospheric dynamics implicated with the leading mode of Asian summer monsoon variability and reveal connections to other important modes of climate variability. The ultimate vision is that increasingly skillful projections of these other climate components will also be used to improve projection of changes in the 21^{st} century monsoon.

An overview of the current consensus on monsoon dynamics and other information on the spatiotemporal variability of rainfall in the Asian monsoon are presented in the introduction to Chapter 2. Instead, I include here short overviews of several topics that are not addressed in any of the following chapters: the history of the monsoon on paleoclimatic timescales, human impacts of monsoon variability, and the consensus of current projections on the future of the monsoon. These are not intended to be exhaustive reviews, but rather background information that justifies the importance of the material in following chapters.

1.1 The Asian Paleomonsoon

The study of rainfall variability in the Asian monsoon suffers from the limited duration of available records. Satellite observations provide an even spacial distribution of rainfall as well as instantaneous snapshots of the same region at different points in its diurnal cycle. The satellite record has continued to expand thanks to the unexpected longevity of the Tropical Rainfall Measuring Mission (TRMM) and the relatively recent Global Precipitation Measurement (GPM) satellite, but unfortunately extends back only to 1997. Instead, we rely on rain gauge data for decadal time series, assembled from daily collection of precipitation at weather stations around the globe, often with very basic apparatus. Unlike satellite observations, records are available only over land and are highly heterogeneous with space and time, and also subject to observational errors. Data sets such as APHRODITE, a rain gauge data set focused on the Asian monsoon region, attempt to weed oust spurious observations with quality control algorithms and then present users with a refined product (Yatagai et al., 2012). This dissertation could not have been written without the efforts of APHRODITE's compilers; they are further acknowledged in subsequent chapters.

We would also like to consider how the monsoon operates under substantially altered climates. The planet is on the verge of reaching a global mean temperature unseen in recent Earth history, and it could be useful to have information on how the monsoon behaved under altered insolation conditions, and how much it can be perturbed from its present form in general. Fortunately, remarkable records exist that can provide information about rainfall on a precessional time scale: cave speleothems, which are stalagmites featuring tens of thousands of years of continuous deposition[1] from which a $\delta^{18}O$ time series can then be compiled, often by stitching together records from multiple stalagmites. Since 2001, dozens of speleothem sites have been developed across East and South Asia, particularly in the East Asian monsoon region (Wang et al., 2001; Dykoski et al., 2005; Wang et al., 2008), but also near the Tibetan Plateau (Cai et al., 2010), Yunnan Plateau (Cai et al., 2015), Altay Mountains(Cheng et al., 2012) and numerous other locations. There are fewer of such records in India, partially because caves are often holy sites in local folklore.

Beyond the difficulty in obtaining such records, their interpretation poses a major challenge. East Asian speleothem $\delta^{18}O$ records tend to feature remarkable agreement across thousands of kilometers, most notably demonstrating simultaneous abrupt transitions on the time scale of precessional forcing (Chiang et al., 2015). Past authors have interpreted these coherent changes as variations in Asian monsoon "intensity", and therefore local rainfall (Wang et al., 2001; Liu et al., 2014), based on the concept of the "amount effect" wherein the $\delta^{18}O$ of precipitation from a parcel will decrease over time as heavier isotopes rain out, a process referred to as Rayleigh distillation (Dansgaard, 1964).

However, in present day observations, the climatological distribution of precipitation $\delta^{18}O$ is poorly explained by Rayleigh distillation, and furthermore monthly variations in precipitation $\delta^{18}O$ across China are poorly correlated with local precipitation and temperature (Dayem et al., 2010; Lee et al., 2012). Instead, China $\delta^{18}O$ is weakly correlated with Indian monsoon rainfall amounts upstream (Lee et al., 2012). Therefore, recent interpretations have turned to alternative mechanisms, such as changes in moisture source region, variations in Indian monsoon rainfall intensity and changes in transport pathway (Maher, 2008; Dayem et al., 2010; Pausata et al., 2011; Baker et al., 2015). That being said, no single theory has explained the abrupt jumps in East Asian speleothem records in a fully satisfactory way, or proven whether they correspond to abrupt changes in Asian monsoon rainfall or not.

On a time scale of millions to tens of millions of years, the Asian monsoon region can be viewed as a geophysical fluid dynamics laboratory. The Tibetan Plateau rose to its full height of 5,000+ meters some time in the past 50 Ma after the collision of the Indian sub-continent, with massive climate impacts. Based on geological evidence, it was previously proposed that a surge in Tibetan Plateau elevation around ~10 Ma may have triggered a sudden

---

[1] At some sites such as in Oman, stalagmite deposition is intermittent, also taken as an indicator of paleomonsoon change (Burns et al., 2001; Fleitmann et al., 2003).

intensification of the Indian monsoon (Harrison et al., 1992; Molnar et al., 1993). However, recent work suggests that a sudden jump in preserved *G. bulloides* deposits in the Arabian Sea around 8.5 Ma, previously attributed to monsoon intensification, likely resulted instead from uplift of the Indian Ocean seafloor (Rodriguez et al., 2014). In addition, theoretical studies suggest that a strong monsoon should exist as long as there remains a region of strong off-equatorial heating, provided by the presence of the Indian subcontinent since 50 Ma (Privé and Plumb, 2007b; Bordoni and Schneider, 2008; Molnar et al., 2010).

One other intriguing multi-million year record exists: northern China's Loess Plateau, the longest continuous depositional basin on the planet. By preserving millions of years of silt and dust from surrounding deserts and the rest of the Northern Hemisphere, the Loess Plateau stores invaluable information about paleoclimate and in particular glacial-interglacial cycles, since the planet tends to be dustier during glacials (Sun et al., 2006). However, like the speleothem records, its interpretation remains a point of contention (Roe, 2009).

1.2 Human Impacts

In summer, monsoonal regions experience bouts of steady, heavy rainfall interspersed by occasional "breaks," and much drier conditions during the rest of the year. In many parts of Asia, this yearly supply is used to grow two crops per year; in India, these two crops are the summer *kharif* and the winter *rabi*, both of whose fruition depends on rainfall supply from the monsoon (Gadgil and Kumar, 2006). The majority of Indian land in the 2000s remained unirrigated and depended directly on rainfall (Krishna Kumar et al., 2004). Therefore, the timing and intensity of the summer monsoon control agricultural outcomes.

An early or delayed Indian monsoon onset can interfere with the transplantation of rice seedlings from their nursery beds (Gadgil and Kumar, 2006). Most Indian crop yields are correlated with June-September All-India monsoon rainfall above a 99% confidence level (Krishna Kumar et al., 2004), and severe drought All-India Monsoon Rainfall years were found to induce cuts to Indian GDP of 2-5% (Gadgil and Gadgil, 2006). Aside from agriculture, extreme rainfall events can inflict massive damages through flooding (Li et al., 2012). The research literature estimating damages from monsoon-season flooding is sparse, although studies of cyclones find that long-term mortality can exceed immediate mortality by an order of magnitude (Anttila-Hughes and Hsiang, 2013), and that countries experiencing 90th percentile cyclone events suffer from a per-capita income reduction of 7.4% 20 years later versus a scenario where the event did not happen (Hsiang and Jina, 2014).

It can be challenging to interpret the historical record of the past fifty years because humans have induced not only warming due to increasing CO_2 but also massive anthropogenic forcing from emissions of NOx, black carbon and other aerosols. It is estimated that high levels of near-surface ozone due to human activity lower India's crop yields by 9% each year, enough to feed roughly 94 million people (Ghude et al., 2014), and that all noxious emissions combined induce a 36% decline in wheat yields (Burney and Ramanathan, 2014). The massive injection of aerosols to East Asia also reduced the amount of insolation directly reaching the surface from 1961 to 1980 (so-called "solar dimming") and increased slowly while the rest of the planet has experienced a solar "brightening" (Norris and Wild, 2009). Over the 2000s in China, reduction of incoming shortwave radiation by aerosols at the surface was found to be -15.7 ± 8.9 W m^{-2} nationwide, and reached -61.2 ± 3.5 W m^{-2} locally in Beijing (Li et al., 2010). Observed climate change in China over the past half-century has been blamed on both aerosols and warming with no clear consensus (Menon et al., 2002; Yang et al., 2015; Yu et al., 2016; Yang et al., 2016).

1.3 21$^{\text{st}}$ Century Projections

The water vapor content of the atmosphere obeys the Clausius-Clapeyron relation and will increase at a rate of roughly 7% per °C of warming. The size and intensity of storms is fundamentally constrained by the available supply of water vapor (Trenberth et al., 2003). However, models consistently project a slower rate of increase of about 2-3%/°C (Allen and Ingram, 2002), potentially due to a slowdown in the overturning circulation in the Hadley Cells (Held and Soden, 2006). The distribution of changes is highly heterogeneous, roughly obeying a "rich get richer" distribution where convective regions become rainier and arid regions drier (Chou et al., 2009). However, particular regions may experience abrupt transitions under further warming, for instance via the template of "convective margin" shifts (Lintner and Neelin, 2007). Both shifts in mean and in the tails of the distribution need to be characterized Pendergrass and Hartmann, 2014. Theory and idealized models suggest that the globally averaged rainfall extremes will increase at roughly 4% per °C, more than the rate of increase of mean rainfall but still below Clausius-Clapeyron, and that rainfall extremes may increase more rapidly in the Tropics (O'Gorman and Schneider, 2009; Muller et al., 2011; O'Gorman, 2012).

Future changes in monsoon rainfall may conform to simple templates such as the rich-get-richer, but the distribution of topography across the Asian monsoon may also make its response unique. For instance, it has been argued that the circulation response to Indo-Pacific warm pool heating has led to an overall drying of South Asia (Annamalai et al., 2013). Examining the past 50 years, Turner and Annamalai (2012) suggested that anthropogenic aerosols countered an increase in rainfall due to increased CO_2 that would have been anticipated in most models. Some authors have speculated that the monsoon could undergo an abrupt régime shift (Zickfeld et al., 2005), while others project a linear increase in rainfall with warming (Boos and Storelvmo, 2016). In models simulating increased CO_2 conditions, Chen (2016) decomposed future East Asian rainfall changes into a fast and slow component of response, and found that the two terms were of opposite sign, with long-term warming and rainfall increase due to heightened sea surface temperature eventually prevailing over a short-term cooling and rainfall decrease due to circulation change.

Many have begun to investigate the impact of future warming on agriculture and economy. Rising nighttime temperature has been indicated as a threat to agricultural productivity, decreasing yields by as much as 10%/°K (Peng et al., 2004). Many crops are found to have a critical temperature, wherein yields will rise steadily up until that temperature and then decline severely if it is exceeded (Schlenker and Roberts, 2009). In Indonesia, global warming in the IPCC4 model suite was suggested to raise the probability of a 30-day delay in monsoon initiation from 9-18% to 30-40% by 2050 (Naylor et al., 2007). Auffhammer et al. (2012) found that agricultural productivity in India was 4% lower during 1966-2002 had monsoon conditions from 1960 persisted through that era. A novel literature focuses on linking climate more directly to human impacts. For instance, Burke et al. (2015) showed that economic productivity is nonlinear with temperature across the globe, with peak productivity occurring at 13°C and decreasing nonlinearly at higher temperature. Hsiang and Jina (2014) suggested that previous estimates of the total cost of global warming had undercounted by $9.7 trillion by neglecting the full economic damage from cyclones under warmer conditions. The field is ripe for the application of such techniques to the South Asian and East Asian monsoon regions, but to our knowledge no efforts to date have focused specifically on those regions.

1.4 Thesis Structure

Chapter 2 presents an analysis of observational evidence from rain gauge precipitation data suggesting that a link exists between interannual variability in the South Asian and East Asian monsoons, and studies the propagation of rainfall anomalies on a daily scale to see if this reproduces leading modes of monthly variability. We propose that the variability of the two monsoons is linked by monthly variations in moisture transport from the Bay of Bengal to the Yangtze River valley across the Yunnan Plateau, a spur of terrain to the southeast of the Tibetan Plateau. Dynamical theory and preliminary model data support major elements of this theory. These results were previously presented in Day et al. (2015).

Chapter 3 develops the Rainband Detection Algorithm (RDA), a recursive image processing tool to analyze daily patterns of frontal rainfall in China. We discover that banded rainfall contribute a large fraction of yearly total precipitation to Central China and describe the seasonal progression of banded rainfall. Our algorithm also allows a novel characterization of the South Flood-North Drought, a known pattern of decadal change wherein central China has experienced increased rainfall and northern China severe droughts beginning in the 1980s. Most notably, rainbands have become *less frequent* in May and *shifted southward* in July-August. Finally, we show that the pattern of decadal change in yearly rainfall totals is due specifically to change in banded rainfall.

Lastly, Chapter 4 returns to the leading mode of Asian summer rainfall variability and shows robust links with two other important climatic components: The Circumglobal Teleconnection, a high-wavenumber Northern Hemisphere standing wave responsible for heat waves, and the East Asian tropospheric jet. Using JRA-55 reanalysis data, we find that changes in westerly moisture transport across the Yunnan Plateau drive a zonal band of heating spanning the Himalayan Foothills and Yangtze River valley, which we propose can then stimulate the CGT mode and contributes to its phase-locking. Also associated with these changes are meridional shifts of the East Asian jet. Using the RDA catalog from Chapter 3, we are able to show that the two major changes in rainbands associated with the South Flood-North Drought also corresponded to southward shifts of the East Asian jet. We suggest that these findings have the potential to improve projection of the 21^{st}-century Asian monsoon.

1.5 Future Directions

Studying rainfall is intrinsically challenging because correlation length scales are short relative to other atmospheric fields. Rainfall results from ascent, which is in turn the residual of much larger-magnitude differences in wind fields. Thus, reproducing its distribution in a computer model presents a massive challenge. The advent of high resolution global climate modeling (below $1^\circ \times 1^\circ$) will therefore change how we can analyze rainfall patterns in the Asian monsoon. Existing studies already show that low, narrow orographic barriers greatly impact the monsoon's climatology (Xie et al., 2006). Studies with high resolution to date already show that resolving low topography and high-resolution features can alter the hydrologic balance and circulation of the monsoon (Risi et al., 2010; Boos and Hurley, 2013; Wu et al., 2014; Wu and Hsu, 2016). A central claim of this dissertation is that moisture transport across the Yunnan Plateau couples the variability of the South Asian and East Asian monsoons. The existence of high-resolution global climate modeling now allows us to test this hypothesis with idealized scenarios. What would happen to moisture transport from South Asia to East Asia, or alternatively if there were no high topography southeast of the Tibetan Plateau at all? Without computer modeling, we struggle to distinguish stimulus from the response. High-resolution modeling can test whether moisture transport from the Bay of Bengal can provide a plausible trigger for intense diabatic heating over the Yangtze River valley, and furthermore whether such heating can drive a CGT-like response.

The response of the Asian monsoon to warming remains a holy grail. Although the CMIP5 suite from the IPCC5 report consistently predicts a stronger Indian monsoon, it is not clear that individual models can simulate the mean state of the Indian monsoon well. This is an even larger problem with the East Asian monsoon, where almost none of the CMIP5 models can produce a climatology showing the northward march of the Meiyu front across spring and summer. My work in this dissertation focuses on particular mechanisms that are important to the rainfall variability of the South Asian and East Asian monsoons, in particular the East Asian jet, the CGT and moisture transport across the Yunnan Plateau. I argue that these mechanisms are more likely to be captured by models because their spatial scale is larger and they lack the heterogeneity over short distances that is intrinsic to rainfall patterns. Given this belief, the best way forward on predicting the future Indian and East Asian monsoon may be to focus on the effects of further warming on each of these climate components individually, and then to deduce later what alterations they may produce in the seasonal cycle of the South and East Asian monsoons.

Lastly, our growing knowledge of the fluid dynamics of the East Asian monsoon should be turned back to the paleoclimate record. Chiang et al. (2015) found a novel way to juxtapose our knowledge of present-day dynamics with the analysis of speleothems by considering the $\delta^{18}O$ of rainfall during different Meiyu stages, and considering what the isotopic signature would be if the timing of those stages was altered. Given our improving knowledge of different East Asian monsoon stages and the ability to model them reasonably, we should discard the idea of a coherent East Asian monsoon "intensity." Instead, we ought to focus on describing changes in rainfall during specific Meiyu stages under altered climates and the $\delta^{18}O$ variations that should result. In addition, the interpretation of the Loess Plateau should be revisited. Its first appearance is often interpreted as the timing of initiation of the East Asian monsoon. However, I suggest that the rise of the Altay Mountains north of the Taklamakan Desert may be a more likely candidate for the trigger of the Loess Plateau's creation, since the presence of the Tibetan Plateau after 50 Ma likely also entails an East Asian monsoon. Given the ability to model jet shifts induced by transient forcing (Liu and Chiang, 2012), we may be able to say something more specific about the change in circulation that first gave rise to the Loess Plateau.

Chapter 2

Coupling of South and East Asian monsoon precipitation in July-August

The following chapter includes work previously published in:

Day, Jesse A., Inez Fung and Camille Risi (2015). "Coupling of South and East Asian monsoon precipitation in July-August". Journal of Climate, **28**, 5419-5433.
`http://dx.doi.org/10.1175/JCLI-D-14-00393.1`

2.1 Abstract

The concept of the "Asian monsoon" masks the existence of two separate summer rainfall régimes: Convective storms over India, Bangladesh and Nepal (the South Asian monsoon), and frontal rainfall over China, Japan and Korea (the East Asian monsoon). In addition, the Himalayas and other orography, including the Arakan Mountains, Ghats and Yunnan Plateau, create smaller precipitation domains with abrupt boundaries. We find a mode of continental precipitation variability that spans both South and East Asia during July and August. Point-to-point correlations and EOF analysis with APHRODITE, a 57-year rain gauge record, show that a dipole between the Himalayan Foothills (+) and the "Monsoon Zone" (Central India, -) dominates July-August interannual variability in South Asia, and is also associated in East Asia with a tripole between the Yangtze Corridor (+) and North and South China (-). July-August storm tracks, as shown by lag-lead correlation of rainfall, remain mostly constant between years and do not explain this mode. Instead, we propose that interannual change in the strength of moisture transport from the Bay of Bengal to the Yangtze Corridor across the northern Yunnan Plateau induces widespread precipitation anomalies. Abundant moisture transport along this route requires both cyclonic monsoon circulation over India and a sufficiently warm Bay of Bengal, which coincide only in July and August. Preliminary results from the LMDZ5 model, run with a zoomed grid over Asia and

circulation nudged to ECMWF reanalysis, support this hypothesis. Improved understanding of this coupling may help to project 21^{st} century precipitation changes in East and South Asia, home to over 3 billion people.

2.2 Introduction

The word "monsoon," once used to denote the winds over the Arabian Sea that reverse seasonally, has migrated in meaning over the centuries to refer to the accompanying period of high rainfall. From June to September, heavy rains over the Indian subcontinent sustain agriculture (Gadgil and Gadgil, 2006) and bring devastating floods. In turn, peak rainfall intervals in other regions are also referred to as monsoons, most occurring during the summer months of peak insolation (the East Asian, African, North American and Australian monsoons) but not all (the East Asian winter monsoon). The South and East Asian monsoons are often referred to jointly as the Asian summer monsoon, even though they differ in month of onset and decay, precipitation amount, diurnal cycle of rainfall, and fraction of local yearly rainfall supplied (Zhou et al., 2008; Molnar et al., 2010; Biasutti et al., 2011).

The core months of the South Asian monsoon (July and August) together deliver over 50% of yearly precipitation to most of India and Nepal, and upwards of 20 mm day^{-1} of rainfall to coastal Bangladesh, according to APHRODITE rain gauge data (described below). In summer, episodes of convective storms last for several weeks at a time, regulated by a strong diurnal cycle (Romatschke and Houze, 2011), and are interspersed by rainfall hiatuses of several days known as monsoon breaks (Krishnan et al., 2000). A core swath of central India including the states of Madhya Pradesh, Chhatisgarh and Odisha, previously named the "Monsoon Zone" by Gadgil (2003), receives about 10 mm day^{-1} of rainfall averaged over summer (shown in Figure 2.1). Daily totals reach as much as 50 mm day^{-1} in Meghalaya north of Bangladesh. The season of intense rainfall starts abruptly, first over southern India in May, next over the "Monsoon Zone" in June and then over northern India in July, and ends over most of India by September. Traditionally, these characteristics are attributed to strong contrast between the low thermal capacity of land and high thermal capacity of the surrounding ocean, a theory dating back to the original study of the monsoon by Halley, 1686. However, it has long been known that surface temperature over India maximizes in May-June, well ahead of peak rainfall (Gadgil, 2003). 20^{th} and 21^{st} century researchers have invoked an alternative thermal argument, which emphasizes the intense summer heating of the high Tibetan Plateau as the primary driver of the continental-scale Asian monsoon (Yeh et al., 1959; Li and Yanai, 1996; Wu et al., 2007). However, Rajagopalan and Molnar, 2013 found that heating of the Tibetan Plateau (measured by near-surface moist static energy) is correlated with Indian rainfall before and after the monsoon (May 20-June 15 and September 1-October 15 respectively), but uncorrelated during its peak (15 June-31 August).

In recent years, a new body of work has strengthened our understanding of the fluid dynamics of the South Asian monsoon. The delay between peak solar forcing and rainfall response and the sudden onset of heavy rainfall have been ascribed to nonlinearity in Hadley cell transitions and reproduced in idealized models (Plumb and Hou, 1992; Schneider and Bordoni, 2008; Bordoni and Schneider, 2008). Furthermore, according to the framework of subcloud moist static energy and convective quasi-equilibrium (Emanuel, 1995; Privé and Plumb, 2007a; Privé and Plumb, 2007b), the strong Indian monsoon exists primarily because the Himalayas shield India from cold inland air (Boos and Kuang, 2010). The debate over the relative importance of Tibetan Plateau heating and topographic blocking continues in the literature (Wu et al., 2012; Boos and Kuang, 2013; Qiu, 2013).

The East Asian summer monsoon manifests unique characteristics compared to its South Asian counterpart and other tropical monsoons. From early June to mid-July, a persistent but migrating zonal front over China, Japan and Korea delivers about 30 mm day^{-1} of rain along its axis. This period of peak frontal activity is known in China as Meiyu season, in Japan as Baiu season and in Korea as Changma season. The preferred position of the Meiyu front shifts northward during this season, with apparent jumps between preferred latitudes (Ding and Chan, 2005). The current debate on the dynamics of Meiyu season rainfall centers around the relative importance of downstream advection of Tibetan Plateau heating (Sampe and Xie, 2010) versus meridional energy convergence induced by topographic forcing of stationary eddies (Molnar et al., 2010; Chen and Bordoni, 2014). Meiyu season generally supplies a lower percentage of yearly rainfall to East Asia compared with the South Asian monsoon: Cumulative May-July rainfall constitutes under 50% of yearly rainfall in southern China, and at most 70% in the northeast (from APHRODITE). The yearly rainfall climatology of China also includes the East Asian "winter monsoon" (Jhun and Lee, 2004), spring persistent rains (Tian and Yasunari, 1998) and post-Meiyu rainfall (cf "midsummer" in Kosaka et al., 2011). Finally, many authors have reported a "South Flood-North Drought" trend in the East Asian summer monsoon since the late 1970s (Gong and Ho, 2002; Ding et al., 2008), attributed either to anthropogenic influence or natural variability (Song et al., 2014; Lei et al., 2014).

In summary, the South and East Asian monsoons share a name, but they are dissimilar in phenomenology and dynamics. Summer daily rainfall rates in India are about twice those of East Asia (10 mm day^{-1} over the "Monsoon Zone" and Himalayan Foothills versus 5 mm day^{-1} over central China, Figure 2.1). In the climatological mean, Meiyu rainfall in central China peaks around June 15-25. Rainfall rates over India increase sharply around this time, but the climax of the South Asian monsoon occurs only a month later during the period July 15-August 5. Summer storms over the Bay of Bengal show a weak midday peak, and storm occurrence along the Himalayan Foothills peaks at night when upslope winds reverse (Romatschke and Houze, 2011), whereas station data from China show a complex diurnal cycle of precipitation that varies regionally (Zhou et al., 2008). The physics of the South Asian monsoon bear more in common with other summer circulations such as the African, North American or Australian monsoons than with the East Asian monsoon (Rodwell and Hoskins, 2001). The most pertinent shared characteristic of the Asian monsoon may instead be sociological: The reliance of the region's dense population on heavily stressed freshwater resources that may be vulnerable to 21$^{\text{st}}$ century climate change (Gleeson et al., 2012; Jiménez Cisneros et al., 2014).

The South and East Asian monsoon, aside from their large-scale differences, each contain many precipitation subdomains. Precipitation has a correlation length scale of about 300 km (Dai et al., 1997), shorter than that of temperature (about 1000 km) and eddies (about 700 km) (Hansen and Lebedeff, 1987; Barnes and Hartmann, 2012). In the South Asian monsoon region, orography can induce transitions across short distances, as seen previously in Xie et al., 2006, Biasutti et al., 2011 and in our Figure 2.1. The Himalayas, less than 100 km wide and above 5 km high, function as a barrier that separates heavy precipitation at the Himalayan Foothills (~30 mm day^{-1}) from the arid Tibetan Plateau ($<$3 mm day^{-1}). Lower ranges such as the Arakan Mountains on the western border of Myanmar[1] (~2000m of altitude) and the Ghats (just ~700m) anchor coastal bands of abundant rainfall ($>$25 mm day^{-1}) on their windward western slope through a combination of forced ascent and diabatic feedback (Xie et al., 2006), and also induce aridity (2 to 5 mm day^{-1}) on their leeward eastern flank.

We focus throughout this work on the impact on rainfall of another region of high topography, the Yunnan Plateau, a north-south spur of the southeastern Tibetan Plateau that descends from over 3 km of altitude in northern Myanmar and southern China to below 1 km further south. The Yunnan Plateau anchors rainfall rates of 20-30 mm day^{-1} to its west, but only about 6 mm day^{-1} on its summit (see Figure 2.1). Thus, the Yunnan Plateau functions as a barrier on the climatological distribution of summer rainfall, similar to other regional orography. However, in our subsequent results, we find that *deviations* from mean rainfall - monthly rainfall anomalies - demonstrate a spatial signature that crosses the Yunnan Plateau in July and August. Not only are northeastern India and the Sichuan Basin on either side of the Yunnan Plateau linked, but points across the entire Asian monsoon domain show robust correlation of rainfall anomalies in these months, even when separated by thousands of kilometers. The goal of the rest of this work is to investigate the coupled interannual variability of the South and East Asian monsoons, and the dynamic role of intervening high topography in this linkage.

In Section 2, we introduce APHRODITE, a 57-year historical precipitation record used in our analysis. Section 3 shows the results of point-to-point correlations and uses an agreement map methodology to display their associated spatial pattern. In Section 4, we use empirical orthogonal function (EOF) analysis over different regions and months to further study the interannual variability of Asian precipitation. Section 5 proposes several local rainfall indices that replicate the large-scale signal. Section 6 investigates storm tracks in the Asian monsoon. Section 7 proposes a mechanism that can explain our findings. In Section 8, we provide a first test our hypothesis using results from the LMDZ model. Section 9 offers some concluding remarks.

---

[1] The crescent-shaped mountains on Myanmar's western flank include the Patkai Hills to the north, the Chin Hills in their center and the Arakan Mountains to the south. In the interest of brevity, we hereafter use the term "Arakan Mountains" to refer to the entire band of high topography (marked by A in Figure 2.1).

2.3 APHRODITE

A Rain Gauge Data Set for Asia

In this study, we use a compilation of rain gauge data from weather stations, APHRODITE (Asian Precipitation - Highly-Resolved Observational Data Integration Towards Evaluation of the Water Resources) (Yatagai et al., 2012). The APHRO_MA_V1101 product includes 57 years (1951-2007) of daily precipitation (PRECIP product, units of mm day^{-1}) and station coverage (RSTN product) on either a .25° × .25° grid (roughly 25 km spacing) or .5° × .5° grid (~50 km spacing) within 60°E-150°E and 15°S-55°N. Subsequent analysis uses the .25° × .25° product unless otherwise indicated. Rainfall values are only available over land. Original station data are provided by national meteorological services, and do not always include all extant stations. Erroneous values are excised via a series of quality control algorithms. The data are then transferred to a fine .05° × .05° grid (roughly 5 km spacing) via topography-dependent spline interpolation, and finally upscaled to the .25° × .25° and .5° × .5° gridded products available to users. A complete description of the assimilation procedure is available in Yatagai et al., 2012. RSTN is expressed as the percentage of .05° × .05° subcells that contain a station within each .25° × .25° cell (cells usually contain either 0 or 1 stations, such that RSTN mostly equals 0 or 4%). We reexpress RSTN as a number of stations STN using the definition STN = RSTN/4 (shown in Figure 2.2).

APHRODITE roughly agrees with existing precipitation data sets, such as the 1° by 1° data set of Rajeevan et al., 2006, but features improved station coverage and accuracy in regions with sharp topography gradients, in particular around the Himalayan Foothills and the Ghats (Yatagai et al., 2012). Analysis of station data is challenging because the distribution of stations is spatially uneven and changes with time. There many also be inherent flaws in measurement due to potential equipment bias and discrepancies in collection intervals between countries. However, alternative precipitation data sets suffer from weaknesses of their own. Reanalysis products such as NCEP-DOE fail to reproduce the intensity and spatial pattern of observed precipitation during monsoon season (Peña-Arancibia et al., 2013). ERA-40 and the newer ERA-Interim product reproduce the seasonal cycle of rainfall distribution on the Tibetan Plateau, but struggle with the magnitude of rainfall relative to rain gauge and hydrological observations (Tong et al., 2014). Satellite precipitation products overestimate low precipitation rates and underestimate heavy precipitation, and also perform poorly in arid regions (Gao and Liu, 2013). TRMM satellite data struggles with quantification of intense precipitation over land (Iguchi et al., 2009). The TRMM 3B42v6 product was found to perform well over low terrain in China but worse over high terrain (Zhao and Yatagai, 2013). Mergers of rain gauge, satellite and reanalysis data exist (Peña-Arancibia et al., 2013; Shen et al., 2014), but for simplicity our analysis relies only on APHRODITE data.

Normalized Monthly Precipitation Anomalies

The daily PRECIP time series $d(x, y, day, year)$ at each terrestrial point (360 × 280 points per day for 20,819 days) are converted into monthly precipitation rates $P(x, y, month, year)$ in order to attenuate high-frequency variability. Choices of 15-day, 10-day (decad) and 5-day (pentad) bins were also tested, with similar results. In order to compare points with different means and standard deviations of rainfall, we find the precipitation anomaly in each month relative to monthly mean, defined as P', and also the normalized anomaly P'', obtained by dividing P' by the 57-year standard deviation σ_{mth} of precipitation in that month. P'' is therefore in units of standard deviation. The means and standard deviations used to calculate P' and P'' are different at each point (x, y). Equivalently in equation form we define the following variables, where σ denotes standard deviation:

$$\begin{aligned}
d(x, y, day, yr) &= \text{57-year daily time-series at point } (x, y) \\
P(x, y, mth, yr) &= d(x, y, day, yr) \text{ converted to monthly mean rate} \\
\overline{P_{mth}}(x, y) &= \overline{P(x, y, mth, yr)}^{\text{57 years}} \text{ for mth} = 1 \text{ to } 12 \\
\sigma_{mth}(x, y) &= \sigma(P(x, y, mth, yr)) \text{ for mth} = 1 \text{ to } 12 \\
P'(x, y, mth, yr) &= P(x, y, mth, yr) - \overline{P_{mth}}(x, y) \\
P''(x, y, mth, yr) &= \frac{P'(x, y, mth, yr)}{\sigma_{mth}(x, y)}
\end{aligned}$$

In all subsequent analysis, the normalized anomaly from each month is treated as a separate time point. For instance, when we discuss a July-August (or JA) anomaly time series over all 57 years, we refer to a time series with 114 points - 57 Julys and 57 Augusts. Similarly, a May-October (MJJASO) time series from 1951-2007 has $57*6 = 342$ independent time points. The autocorrelation of normalized rainfall anomalies between successive months is low, which supports the claim that each month in a normalized rainfall anomaly time series represents an independent observation.

Reference Points and Regions

In Section 3, we focus on the P'' monthly normalized rainfall anomaly time series at 22 reference points with good station coverage over the 57-year time period (Table 1). The nearest urban agglomeration to each point is listed for illustration. The results from Section 3 are robust to the replacement of chosen points with other nearby points. We also designate 6 reference regions, three each over South and East Asia (Figure 2.2). In South Asia, the three regions are the Himalayan Foothills + Bangladesh, the “Monsoon Zone,” and South India east of the Ghats. The three regions in East Asia are South China (which also includes Taiwan and northern Vietnam), the“Yangtze Corridor” stretching from Sichuan to Shanghai, and North China along the Yellow River.

P'' time series are calculated for each of the 22 points and 6 regions. All 22 reference points belong to one of the six regions, except for a point each in South Korea (Jinju) and

Japan (Tokyo). Both of these points are well correlated with the Yangtze Corridor in summer (Figures 2.3 and 2.4), but the correlation of the rest of Japan and South Korea with the Yangtze Corridor is weak. Precipitation anomalies within each region are highly correlated. Regional time series are defined as $P''_{region} = \overline{P''(x,y)}^{x,y}$, the mean standardized anomaly over the region, and are used to confirm that our results are not sensitive to the exact choice of reference points. We could also first construct a regional time series $P_{region} = \overline{P(x,y)}^{x,y}$ and calculate the corresponding mean and standard deviation, but such a procedure emphasizes points with high variance. In practice, the two methods produce highly similar time series except for the Himalayan Foothills + Bangladesh time series, which includes very rainy points near Meghalaya.

The density of observations in APHRODITE varies widely (Figure 2.2). Japan features a nationwide dense station network, whereas almost no data are available from the western Tibetan Plateau. Several of our reference points (Nyingchi on the eastern Tibetan Plateau and Karachi at the edge of the Thar Desert) contain the only station within a 100 km radius and should be interpreted with caution. Station density also changes with time. The number of available stations in India drops abruptly from over 3000 during 1951-1970 to <1000 in 1971 and thereafter. In China, the number of stations remains roughly constant in time (~700 stations). To limit the impact of station heterogeneity in space and time, we select reference points with good data, and adjust the methodology of our EOF analysis to account for station coverage.

2.4 Spatial Coherence of Precipitation Anomalies

Point-to-point Correlations

Formula

Between two monthly precipitation time series P_1 and P_2, we define the Pearson product-moment correlation coefficient, also referred to as the "correlation coefficient" or r, which also equals the mean product of monthly normalized anomaly time series P''_1 and P''_2:

$$r(P_1,P_2) = \frac{\sum\left(\left(P_1-\bar{P}_1\right)\left(P_2-\bar{P}_2\right)\right)}{n\sigma\left(P_1\right)\sigma\left(P_2\right)} = \frac{\overline{\left(P_1-\bar{P}_1\right)\left(P_2-\bar{P}_2\right)}}{\sigma\left(P_1\right)\sigma\left(P_2\right)} = \overline{P''_1 P''_2}$$

This formula assumes that monthly rainfall anomalies follow a normal distribution, whereas daily and monthly rainfall rates are more accurately described by a gamma distribution, both in Asia and elsewhere (Mooley, 1973; Aksoy, 2000; Husak et al., 2007). Monthly anomalies at the 22 reference points approach a normal distribution except for at Karachi, where the standard deviation exceeds the mean (Table 1). This results from occasional monthly surges of up to 8 mm day^{-1} superimposed on a hyperarid (1 mm day^{-1}) background. We persist in using the standard formula for r anyway in the interest of simplicity.

Results

We focus on summer rainfall, and in particular July-August when the South Asian monsoon peaks. In Figure 2.3, we show the 57-year intercorrelation of monthly rainfall anomalies P'' for each of our 22 reference points in July-August (JA, 114 time points; bottom-left), and also for summer half-year months (MJJASO, 342 time points; top-right). Correlations significant at a 95%/99% confidence levels are marked with single/double cross-hatching, estimated using Student's t-test with degrees of freedom $n = 112$ for July-August and $n = 340$ for summer half-year months. The number of effective degrees of freedom n in cross-correlation is reduced if both time series share nonzero autocorrelation at a particular time lag (Livezey and Chen, 1983), which can raise the threshold for statistical significance. However, the shared autocorrelation of both JA and MJJASO rainfall time series is found to be very low.

Intraregional correlations are generally strong for both July-August and for summer half-year months. In July-August, statistically significant correlations are also found between points in different regions, even though the amplitude and seasonality of summer rainfall vary greatly between sites, as noted by Wang and LinHo, 2002. For instance, July-August mean rainfall varies by an order of magnitude between Chittagong (16.55 mm day^{-1}) and Karachi (1.68 mm day^{-1}). Mean rainfall peaks in June in southern China, July-August in northern India and fall in southern India. Nevertheless, July-August precipitation anomalies are coherent over more than 5000 kilometers, from Tokyo and Karachi ($r = -.23$, significant at a 95% level) to pairs of points in between, whereas significant correlations during summer half-year months (May-October) are mostly limited to pairs of points within the same region.

To verify the robustness of these findings, we reproduced Figure 2.3 using different combinations of summer months, including June-September (JJAS). The choice of July-August was found to maximize interregional correlation strength. Correlations were also calculated between regional time series (not shown). Their magnitude mostly exceeds the 99% confidence level, with sign of correlation matching the overall pattern observed in Figure 2.3. The preceding analysis implicitly assumes that the spatial correlation fields associated with a positive and negative rainfall anomaly are mirror images of one another. This is not guaranteed to be true. For instance, the spatial pattern of El Niño and La Niña teleconnections are not exact inverses (Hoerling et al., 1997). To test for this possibility, we compile two composites of years: a "wet composite" only including the 5 most positive July-August anomaly years at Kathmandu and a "dry composite" with the 5 most negative years. We again reproduce Figure 2.3 with each composite, and obtain similar results for both composites (not shown).

The strongest July-August interregional correlation is a dipole between points in the Himalayan Foothills (hereafter defined as +) and "Monsoon Zone" (-) ($r = -.59$ using regional time series). This dipole structure over South Asia recurs throughout this study. South India also simultaneously tends to experience positive anomalies ($r = .52$ with Himalayan Foothills and -.20 with "Monsoon Zone"). This spatial pattern has been known to the Indian Meteorological Department since the 1960s (Krishnamurthy and Shukla, 2000). In East Asia, a tripole pattern emerges with precipitation increases over the Yangtze Corridor, Korean Peninsula and Japan and corresponding decreases over South China, Taiwan and

North Vietnam, as well as a smaller decrease in North China (from north to south, - + -). This pattern is also found in previous studies (Ding et al., 2008), and should not be conflated with the variability of the Meiyu front, since Meiyu season ends sometime in mid-July (Wang and LinHo, 2002). The relatively low correlation of reference points in North China with other regions may reflect chaotic forcing from the westerlies in that region (Kosaka et al., 2012). Finally, Figure 2.3 reveals that many points in South Asia are significantly correlated to points in East Asia during July-August. In particular, anomalies over the Himalayan Foothills correspond to anomalies over the Yangtze Corridor ($r = .35$ using regional time series). Previous authors have investigated potential connections between the South and East Asian summer monsoons (Lau et al., 2000; Liu and Ding, 2008). Krishnan and Sugi, 2001 found a correlation exceeding a 95% significance level between June-July integrated rainfall over the "Monsoon Zone" and Baiu intensity (the Meiyu front over Japan). A similar result is visible in Figure 2.3. The link between the two regions is investigated in following sections.

Agreement Map

According to Figure 2.3, July-August interannual precipitation anomalies are correlated across large distances. In order to elucidate their spatial structure, we employ an agreement map methodology that compares the pattern of anomalies predicted by each of our 22 reference points. The agreement $A(x, y)$ is defined via the following formulas:

$$\begin{aligned}
R_i(x,y) &= r(P_i, P(x,y)) \\
S_i(x,y) &= R_i(x,y) \times sgn(r(P_i, P_{Nepal})) \\
Q_i(x,y) &= \begin{cases} sgn(S_i(x,y)) & \text{if } |S_i(x,y)| > .2 \\ 0 & \text{if } |S_i(x,y)| < .2 \end{cases} \\
A(x,y) &= \sum_i Q_i(x,y)
\end{aligned}$$

For each reference point i with local time series P_i, we find the correlation of P_i with $P(x, y)$ for all x and y during July-August, defined as $R_i(x, y)$ (360 × 280 points for 114 months). In order to compare two different $R_i(x, y)$ maps, they must be defined with the same sign convention. We choose Kathmandu (85.4°E 27.6°N, reference point #2) as our frame of reference because of its strong correlations with other reference points and high station coverage. If reference point i is negatively correlated with Kathmandu ($r(P_i, P_{Nepal}) < 0$), we flip the sign of R_i. The R_i with adjusted sign are defined as $S_i(x, y)$ and can now be directly compared. The choice of other reasonable reference frames leads to similar results. We then isolate regions of robust correlation in each S_i with a magnitude threshold. $Q_i(x, y)$ is defined as the sign of $S_i(x, y)$ (+1 or -1) if the magnitude of S_i at that point exceeds .2, and 0 otherwise. The choice of .2 as threshold (roughly a 97 % confidence level using degrees of freedom $n = 112$) is arbitrary, and changing the threshold does not alter the overall pattern seen in Figure 2.4. Finally, the agreement $A(x, y)$ is obtained by summing all Q_i. A high magnitude of A at a point (x, y) indicates that a strong anomaly is predicted at (x, y) given the prior observation of an anomaly at each reference point.

Figure 2.4 shows a July-August agreement map using all 57 years. We also tested agreement maps using the composites of wet and dry years defined in section 3a, and find that results are not substantially altered in either case except for increased noise due to smaller sample size (not shown). A weak branch of positive anomaly extends northward from the Bay of Bengal, on the western flank of the Arakan Mountains. When this branch reaches the Himalayas, it strengthens and bifurcates into northwestward and northeastward trajectories. The northwestward branch runs along the Himalayan Foothills to Nepal without encroaching onto the Tibetan Plateau. The northeastward branch follows a channel between the Himalayas to the north and the Arakan Mountains to the southeast, fills the northeastern notch of the Himalayan Foothills, and spills onto the southeastern Tibetan Plateau. This branch also crosses the nothern Yunnan Plateau into Sichuan and the Yangtze Corridor of central China, and stretches weakly across South Korea and Japan. The tilt of this band resembles that of the Meiyu front, even though Meiyu season in central China ends during July.

In some places, sharp transitions between regions of positive and negative anomaly are collocated with orography, similar to the steep gradients in mean precipitation in Figure 2.2. For instance, both the Arakan Mountains and Ghats divide regions of opposite sign on their western and eastern flanks (+ and - respectively for the former, - and + for the latter). In contrast to these other topographic barriers, a continuous band of positive anomaly connects the southeastern Tibetan Plateau (~4 km of altitude) and northern Yunnan Plateau (~3 km) with the low terrain of Bangladesh and the Himalayan foothills. It is also known from observation of δ^{18}O isotopes in rainfall that moisture in summer storms on the southern and southeastern Tibetan Plateau originates from the Bay of Bengal (Yao et al., 2009; Gao et al., 2011; Yang et al., 2011a). Therefore, the Himalayas to the west of Nepal (80-86° E) function as an apparent barrier, but the eastern half of the Himalayas (east of 86° E) does not. The role of topography in blocking or allowing flow is not immediately explicable within existing monsoon theory. We propose a hypothesis explaining these features in Section 7.

2.5 Empirical Orthogonal Function (EOF) Analysis

Technique

We seek to confirm the results of our point-to-point correlations and agreement map method using an alternative technique. EOF analysis is commonly used in climate studies to reveal leading modes of variability in a set of time series without the assumption of periodicity or preselected basis functions. This is achieved by finding the eigenmodes of the correlation or covariance matrix of all of the time series with one another (Lorenz, 1956; Wilks, 2006). Each eigenmode consists of a paired space and time component, hereafter referred to as spatial and temporal EOFs. These modes are ordered by the percentage of total variance that each explains, and typically a subset of several important modes is isolated. These are not guaranteed to have have physical significance, but nonetheless can help to characterize a system. EOFs of precipitation have been calculated for India (Krishnamurthy and Shukla, 2000) and China (Ding et al., 2008), but to our knowledge not for the entire Asian monsoon or with APHRODITE.

Normalized anomaly time series P'' (units of standard deviation) are used throughout our EOF analysis in order to weight anomalies at all points evenly. The interpolation algorithm used to compile APHRODITE provides daily data at every spatial point even if no stations are nearby. Without some adjustment for station coverage, the EOF technique can therefore generate spurious modes with high amplitude in areas with few true data, such as the western Tibetan Plateau and Taklamakan Desert. Therefore, we implement a method to include data only if a station is nearby, as indicated by the STN product. We define s as the percentage of days in each month where there is an operating station within 100 km of a point (x, y). If $s < .5$, P" at (x, y) is reported as missing for the month. Subsequently, if more than half of monthly values are missing over the 57 years, the point is omitted entirely from the calculation of EOFs. This guarantees that all pairs of time series will overlap for at least one month according to the pigeonhole principle, permitting the calculation of their covariance. In practice, for Julys and Augusts from 1951 to 2007, 30.8% of time series overlap on all months, 90% of time series overlap on 75% of months, and 99.7% of time series overlap on at least 50% of months. Different proximity criteria for data inclusion were also tested, but the current 100 km criterion is sufficient to eliminate spurious modes. The resulting temporal EOFs do not include gaps because missing values are replaced with estimates that minimize expected error in a least-squares sense, as described in the appendix of Chelton and Davis, 1982.

In calculating EOFs, each monthly anomaly is treated as an independent time point, as described in Section 2 and consistent with the analysis in Section 3. EOFs are calculated for the months of June through September separately (57 time points), July-August (114 time points; also referred to as JA), each season (DJF, MAM, JJA, SON; 171 time points) and for the summer and winter half-year months (MJJASO and NDJFMA respectively; 342 time points). In addition, July-August EOFs are found for the entire Asian monsoon region ("All-Asia," 66°E-142°E, 5°N-45°N) as well as India (71°E-95°E, 10°N-30°N) and China (100°E-123°E, 20°N-40°N) separately. The India and China subregions as defined each include parts of other countries ("India" includes Bangladesh, Nepal, Bhutan, western Myanmar and southern Tibet, while "China" includes northern Vietnam and Laos), but are referred to by single country names for convenience. All-Asia EOFs are calculated at $.5^\circ \times .5^\circ$ resolution and regional EOFs are calculated at $.25^\circ \times .25^\circ$ resolution. Although APHRODITE also releases a $.5^\circ \times .5^\circ$ product, the All-Asia EOFs are instead obtained by calculating s at $.25^\circ \times .25^\circ$ resolution and then including one out of every two points in each direction. The calculation of EOFs at $.5^\circ \times .5^\circ$ resolution produces very similar results to our procedure.

Preisendorfer's "rule N" (Preisendorfer et al., 1981) and the North et al., 1982 "rule of thumb" are used to assess statistical significance and independence of EOFs. The modes of rainfall variability described below are all statistically significant by rule N. However, leading

EOFs are generally not well-separated, which indicates that their physical significance should be interpreted with caution. We also test the sensitivity of computed EOFs to varimax rotation (Kaiser, 1958), which has been claimed to produce modes with greater physical significance (Wilks, 2006).

Results

Leading modes of precipitation variability explain low percentages of variance relative to the leading modes of other atmospheric fields. For instance, EOF1 of global monthly rainfall, which is related to ENSO, explains only 6.3% of total variance (Dai et al., 1997). In South and East Asia, leading precipitation modes change greatly between seasons. During the winter half-year (NDJFMA), a north-south dipole with few local features dominates Asian precipitation variability (11.8% of variance explained, Figure 2.5a). In fall (SON), the leading mode of All-Asia variability contrasts China with the Yunnan Plateau (8.6%, Figure 2.5f). No statistically significant correlation is found between temporal EOF1s from different seasons, or between the summer and winter half-year EOF1 time series.

We begin by finding the leading All-Asia EOF of each month from June to September separately (Figure 2.6). July EOF1 closely resembles August EOF1, with a slight meridional displacement visible over China (centered pattern correlation of $r = .7$), but Figure 2.6 shows that June and September EOF1 are both rather different. Furthermore, in July and August, EOF1 explains 10.4% and 12.9% of variance each, versus 9.9% and 8.7% in June and September respectively. June and September EOFs 2-4 are also distinct from July and August EOFs 2-4 (not shown). In summary, July and August show distinct behavior which we further explore below through joint July-August EOFs (Figure 2.7).

July-August All-Asia spatial EOF1 (9.4% of variance explained, Figure 2.7a) closely resembles the agreement map in Figure 2.4. July-August spatial EOFs 2-4 (Figures 2.7b-d) all also feature competition between the “Monsoon Zone” and Himalayan Foothills, and either a north-south tripole or dipole pattern in China. In particular, EOF3 resembles EOF1 in South Asia but with flipped sign in East Asia (spatial correlation in South Asia: .32, in China: -.31; obtained by centered pattern correlation). The tripole and dipole pattern over East Asia are similar to SVDs 1 and 2 of East Asian summer rainfall in Kosaka et al., 2011. The first four All-Asia JA EOFs cumulatively account for 25.7% of total variance (9.4%, 6.8%, 5.2% and 4.2% respectively).

The choice of a large region for EOF analysis may lead to mixing of independent modes (Dai et al., 1997; Wilks, 2006). Therefore, we repeat our EOF analysis of July-August rainfall for India and China separately (Figure 2.8). India JA spatial EOF1 again displays a Himalayan Foothills-“Monsoon Zone” dipole, and is almost identical to the South Asian portion of Figures 2.4 and 2.7a. This mode dominates regional variability (22.5% of variance explained). Furthermore, spatial EOFs 2-5 also retain a similar dipole but shifted zonally or meridionally (not shown).

In China, three EOFs (hereafter referred to as C_1, C_2 and C_3) each explain over 10% of July-August variance, while no other mode surpasses 7%. C_1 and C_2 both feature tilted zonal bands and meridional contrast (16.1% and 14.9% of variance explained), while C_3 contrasts low terrain in southern and eastern China with elevated regions inland (11.2%, not shown). Neither C_1 nor C_2 matches the China component of All-Asia JA spatial EOF1 or EOF2, hereafter referred to as AA_1 and AA_2 (in contrast to All-Asia EOFs 1 and 2, which refer to the spatial patterns over the full domain seen in Figure 2.7). However, the application of a 45° rotation to the combination of C_1 and C_2 reproduces AA_1 and AA_2 very closely ($AA_1 = .59C_1 + .51C_2$, $AA_2 = -.51C_1 + .55C_2$; coefficients obtained by correlation of temporal EOFs). This implies that both sets of EOFs (C_1/C_2 and AA_1/AA_2) describe the same variability.

Leading July-August All-Asia EOFs capture similar patterns of variability as regional EOFs, but also show an interregional coupling similar to Figures 2.3 and 2.4. Specifically, positive anomalies along the Himalayan Foothills tend to correspond to positive anomalies along the Yangtze Corridor and vice-versa. In support of this claim, All-Asia JA EOF1 (+ over Himalayan Foothills, + over Yangtze Corridor) explains 9.4% of variance versus 5.2% explained by All-Asia JA EOF3 (+ over Himalayan Foothills, - over Yangtze Corridor). We create an AA_1 time series (China portion of All-Asia JA EOF1) by a linear combination of the C_1 and C_2 time series, and find a correlation with India temporal EOF1 of .46, which exceeds a 99.9% confidence level. We also repeat EOF analysis for the India and China subregions over different summer time periods - June-September (JJAS) and Meiyu season (mid-May to mid-July, 10-day bins). In each case, the resulting leading modes resemble India JA EOF1 and China JA EOFs 1 and 2 in Figure 2.8. The fixity of leading regional modes throughout summer suggests that June All-Asia EOF1 and September All-Asia EOF1 are different from their July and August counterparts because of a change or absence of coupling between India and China. Finally, we test the effect of large domain size by applying varimax rotation to leading July-August All-Asia EOFs. The resulting leading mode resembles either India JA EOF1 or AA_1, with no interregional coupling. However, this could reflect that the magnitude of regional variability within India or China is greater than that of the interregional signal.

In summary, the results of EOF analysis as shown in Figures 2.6- 2.8, in combination with the statistically significant point-to-point correlations and agreement map shown in Figures 2.3 and 2.4, support the existence of a July-August coupling of rainfall anomalies between India and China.

2.6 Indices of All-Asia JA EOF1: All-Nepal Rainfall and Yangtze Rainfall

We seek an index of July-August All-Asia EOF1 that can be calculated using a smaller region. All-India Monsoon Rainfall (AIMR) has been used in many previous studies (Parthasarathy et al., 1994), and is made freely available by the Indian Meteorological Department (IMD, cf Acknowledgments for website), but the national boundaries of India include subregions that are inversely correlated according to All-Asia JA EOF1 and India JA EOF1. Instead, we propose All-Nepal monsoon rainfall as a suitable index because of high positive amplitude of All-Asia JA EOF1 across the country and good station coverage from 1960 onward (Nepal borders shown in Figure 2.1). In subsequent sections, we argue that this high amplitude results from Nepal's sensitivity to changes in moisture transport from the Bay of Bengal. Previous authors have calculated All-Nepal monsoon rainfall time series (Kansakar et al., 2004), but the Nepal Department of Hydrology and Meteorology does not release such data publicly. APHRODITE contains a large subset of the 337 total precipitation stations in Nepal (number obtained from `http://dhm.gov.np`), and we have therefore compiled our own monthly time series (Supplementary Table 1).

As previously mentioned, July All-Asia EOF1 and August All-Asia EOF1 are very similar spatially. Furthermore, August All-Nepal rainfall is not significantly correlated with that in preceding July during 1951-2007 ($r = -.14$), which implies that successive July and August monthly rainfall anomalies in Nepal are independent from one another. Therefore, we treat each July and August anomaly as a separate point in a joint July-August All-Nepal monsoon rainfall time series with 114 time points. Our index is expressed in units of standard deviation, with July rainfall anomalies normalized using July mean and variance and the equivalent procedure for August.

In China, the Yangtze Corridor corresponds to a region of high AA_1 amplitude and AA_2 near zero. We define Yangtze rainfall as mean rainfall over the region bounded by the points (104.5°E 29°N), (108°E 32°N), (120°E 34°N) and (122°E 31.5°N) that includes parts of Sichuan, Hubei, Anhui and Jiangsu Provinces (Figure 2.1). We also compile a time series for the "Monsoon Zone" as defined in Gadgil, 2003, also shown in Figure 2.1. Each of these time series is compiled for July-August using the same procedure described in the previous paragraph.

Table 2 shows the correlation of July-August All-Nepal monsoon rainfall and Yangtze rainfall with All-Asia JA EOF1 and other time series of interest, calculated using all Julys and Augusts from 1951 to 2007 (114 time points total). Wang and Gillies, 2012 asserted that All-Nepal and All-India rainfall are uncorrelated, and thence claimed that Nepal rainfall undergoes a mode of decadal variability distinct from the rest of the South Asian monsoon. Instead, we find that All-Nepal monsoon rainfall matches India JA EOF1 closely, and is also significantly correlated with leading EOFs in China, even though its correlation with All-India Monsoon Rainfall is indeed near-zero. The "Monsoon Zone" time series shows even better correspondence to leading EOF modes, but the number of stations within the region drops precipitously from over 3000 for 1951-1970 to <800 beginning in 1971 due to delays in archiving data (Rajeevan et al., 2006). This leads us to prefer All-Nepal monsoon rainfall as an index of All-Asia JA EOF1. All-India Monsoon Rainfall remains strongly correlated with leading temporal EOFs because most of India lies in a region of negative All-Asia JA EOF1. However, All-India Monsoon Rainfall misses the connection to Yangtze monsoon rainfall that is revealed by the use of either All-Nepal monsoon rainfall or "Monsoon Zone" rainfall.

ENSO induces the leading mode of global interannual precipitation variability (Dai et al., 1997). Xie et al., 2009 showed that El Niño events, which peak in December, lead to robust changes in precipitation and atmospheric circulation in East Asia in the subsequent June to August through the Indian Ocean "capacitor effect." We would like to determine whether All-Asia JA EOF1 reflects this process or some other mechanism. Therefore, we test the correlation of the Oceanic Niño Index (ONI) in preceding December with the other time series in Table 2. ONI is a three-month running mean of the Niño 3.4 time-series (sea surface temperature (SST) anomalies averaged over the region 5°S-5°N and 120°W-170°W). SST measurements are derived from ERSSTv3b, identical to ERSSTv3 as described in Smith et al., 2008 but with satellite SST observations excluded due to known bias. This index matches that used in Xie et al., 2009. The baseline used to calculate anomalies by ONI is periodically adjusted to account for global increase in mean SST, but the difference in baseline between the 1950s and 2000s is only .3°C and does not influence results. ONI is correlated with All-India Monsoon Rainfall at a 95% confidence level, but not with any other time series. This suggests that All-Asia JA EOF1 is not a direct reflection of ENSO variability.

2.7 Storm Tracks with APHRODITE

Previous Work

In the search for a process that connects South and East Asia, we investigate the propagation of storms. A simple first hypothesis is that the patterns observed in Figure 4 and All-Asia JA spatial EOF1 correspond to interannual changes in the frequency or trajectory of storms. Storms in the Asian monsoon can propagate across thousands of kilometers, but interface with topography in complex ways (Romatschke and Houze, 2011). Luo et al., 2011 used CloudSat and CALIPSO satellite data to determine the horizontal and vertical length scales of storms in different regions (India, the Tibetan Plateau and East Asia), and found that storms on the Tibetan Plateau are shallower and have a shorter horizontal length scale than storms in India. One possible interpretation of this result is that storms do not cross between India and the Tibetan Plateau. However, it has been known for decades that vortices on the Tibetan Plateau may, depending on synoptic conditions, propagate downstream to eastern China, where they induce heavy rainfall and potential flooding (Tao and Ding, 1981; Murakami and Huang, 1984; Chen and Dell'Osso, 1984; Yasunari and Miwa, 2006; Xu and Zipser, 2011; Wang et al., 2012). Likewise, depressions from west Pacific tropical cyclones can cross Indochina and reach India from July to September depending on background circulation (Chen and Weng, 1999; Fudeyasu et al., 2006). Thus, storms can propagate between South and East Asia under some circumstances. We quantify this behavior below.

Technique

Past studies have used HYSPLIT (Hybrid Single Particle Lagrangian Integrated Trajectory) analysis to create back-trajectories of air parcels in Asia during monsoon season (Medina et al., 2010; Cai et al., 2012; Gao et al., 2013). However, HYSPLIT uses circulation obtained from reanalysis products, which struggle to produce realistic frequency distributions of precipitation in the region (Peña-Arancibia et al., 2013). As an alternative, we use lag-lead correlation with APHRODITE to extract the propagation of precipitation anomalies across days. This analysis cannot show all storms, for instance storms that do not produce rainfall or that do not propagate across multiple days, but suffices to study the passage of storms between South and East Asia, which is our focus.

For a reference point i with normalized anomaly time series P''_i and a phase lag of λ days, the lag-lead correlation $c_i^\lambda(x, y, yr)$ with rainfall at another point x, y is given by:

$$c_i^\lambda(x, y, yr) = \sum_{days} P''_i(day, yr) * P''(x, y, day + \lambda, yr),$$
$$\text{for } \lambda = \text{-5 to +5 days and year} = 1951 \text{ to } 2007$$

This is identical to the formula for the correlation coefficient r with an offset of λ days between time series (a lag or lead depending on the sign of λ). APHRODITE cannot provide information on sub-daily variation, propagation over oceans, or different mechanisms of propagation. However, the 57 years of data can be used to extract both mean storm trajectories and their interannual variability. The c_i^λ require further processing to isolate propagation because there tends to be a nonzero positive background field *independent of the value of* λ. This background field, different for each reference point i, results from several effects, including the false positive correlation of two points without rain, even if they are distant from one another, and also the deviation of precipitation anomalies from a normal distribution. We define the background field $b_i(x, y)$ as the mean lag-lead correlation averaged over all λ and years, and thereafter analyze the *anomaly* from this background, $C_i^\lambda(x, y, yr)$, and the 57-year mean anomaly $K_i^\lambda(x, y)$:

$$\begin{aligned} b_i(x, y) &= \overline{c_i^\lambda(x, y, yr)}^{\text{57 years, } \lambda=\text{-5 to +5}} \\ C_i^\lambda(x, y, yr) &= c_i^\lambda(x, y, yr) - b_i(x, y) \\ K_i^\lambda(x, y) &= \overline{C_i^\lambda(x, y, yr)}^{\text{57 years}} \end{aligned}$$

We calculate $C_i^\lambda(x, y, yr)$ and $K_i^\lambda(x, y)$ at every reference point for λ = -5 to 5 and from 1951 to 2007. Figure 8 shows K_i^λ for reference points i = 2, 6, 13, 16 and 21 (Kathmandu, Durg, Shenzhen, Enshi and Baotou) as well as two additional sites, Lijiang (100.4°E 26.9°N) and Lake Qinghai (100.1°E 37.4°N). In addition, for each reference point and lag λ, we find the location of maximum $C_i^\lambda(x, y, yr)$ in each of the 57 years, and then draw the smallest circle that contains at least 50% of each of the yearly maxima. This quantifies interannual variability. Figure 9 condenses propagation information from Figure 8 into a single composite image by showing the lag λ for which $K_i^\lambda(x, y)$ is maximized, with 50% variance circles for selected λ and connecting arrows superimposed. Using these tools, we focus on whether storms propagate between South and East Asia, whether storm tracks change between years, and what trajectories reveal about underlying dynamics.

Steering by 200 mb level Winds

In Figure 8, K_i^0 ($\lambda = 0$) reveals the size of storms at each reference point, typically around 300 km. Interannual variability is generally small for $\lambda =$ -2 to 2. Negative values of $K_i^\lambda(x, y)$ may result from a strong positive K_i^λ on another day, and should not necessarily be interpreted as storm suppression. All reference points show coherent propagation of anomalies across days.

We focus first on the South Asian monsoon domain. In the "Monsoon Zone" (Figure 8b, Durg), storms propagate west-northwestward from the Bay of Bengal with little variance in trajectory, also seen in past work such as Figure 1 of Sikka, 1977. These storms, known in the literature as "monsoon depressions" or "low-pressure systems"(Sikka, 1977; Chen and Weng, 1999; Krishnamurthy and Ajayamohan, 2010), generally do not reach tropical cyclone intensity. Instead, tropical cyclone occurrence in the Bay of Bengal is confined mostly to October-November and April-May (Li et al., 2013). Several previous studies show that monsoon depressions can originate from further east over Indochina or the South China Sea (Saha et al., 1981). Storms reaching Kathmandu (Figure 8a) also propagate westward, but their primary source is the Yunnan Plateau to the east, with a contribution from Bangladesh and the Bay of Bengal visible at $\lambda =$ -1. In turn, Figure 8d (Lijiang) shows that these Yunnan Plateau storms originate from the mid-latitude westerlies north of the Tibetan Plateau ($\lambda =$ -5 to -2). Bay of Bengal depressions do not reach the Yunnan Plateau. The Himalayas divide regions of westerly and easterly propagation. Figures 8a and 8b also indicate that rainfall peaks over the Himalayan Foothills and South India 5 days before and after a storm passes through the "Monsoon Zone," and vice-versa. This reflects the spatial pattern associated with "intraseasonal oscillations," or ISOs, an extensively studied 10-20 day mode of variability associated with the cycle of active and break periods in the South Asian monsoon (Krishnamurti and Ardanuy, 1980; Chen and Chen, 1993; Annamalai and Slingo, 2001; Han et al., 2006; Fujinami et al., 2011; Fujinami et al., 2014).

In East Asia, the direction of propagation also shifts from westerly north of 30°N to easterly over South China. In Figures 8c and 9c (Shenzhen), storms from the Philippines and Taiwan move northwestward to South China and then westward toward the Yunnan Plateau, with low interannual variability for $\lambda =$ -2 to 2. This behavior has been seen both in observation (Chen and Weng, 1999; Liu and Chan, 2003) and in idealized monsoon studies (Privé and Plumb, 2007b). Baotou, our northernmost reference point (Figures 8g and 9g), sits at the July-August latitude of the tropospheric jet (Schiemann et al., 2009), and propagation is therefore strictly westerly. Central China marks the transition between westerly and easterly storm advection. Over Enshi (Figures 8e and 9e, Yangtze Corridor), westerly storms are sheared into northeast-southwest tilted bands. This phenomenon, also seen in Figures 8f and 9f (Lake Qinghai), can be understood by considering upper-level winds at this latitude (Figure 10a). If a midlatitude storm transported by the westerly jet is perturbed southward, it will gain westward velocity from mean flow, whereas storms passing further to the north continue eastward. The Himalayas block the passage of storms between the Tibetan Plateau and India, but storms are able to traverse the lower terrain of the Yunnan Plateau.

In all regions, the direction of propagation agrees closely with 200 mb-level winds (Figure 10a). For the previously discussed "monsoon depressions," this observation is in fact a coincidence. The west-northwestward travel of monsoon depressions instead results from an unusual secondary circulation that advects disturbances against lower-level flow without interacting with the upper troposphere (Chen and Yoon, 2000; Chen et al., 2005), even though the predecessors of monsoon depressions are brought by upper-level winds from the east. In the rest of Asia, upper-level winds steer disturbances. We verify this claim by also performing lag-lead correlations for the months of June and September (not shown). Trajectories are mostly similar, and substantial changes correspond to changes in 200 mb-level winds. The low interannual variability of storm trajectories results from the relative constancy of upper-level winds between years, as seen for instance with tropical cyclones in the western Pacific (Kumar and Krishnan, 2005). The band of positive correlation in All-Asia JA EOF1 does not correspond to the storm tracks in Figures 8 and 9, nor to their interannual variations. Figures 10c and 10d show the 200-mb level winds associated with the 5 most positive EOF1 years ("wet" years) and 5 most negative years ("dry" years). The steering direction of storms remains steady in both, although some changes occur. A check of the K_i^λ in these "wet" and "dry" years also does not reveal major differences (not shown). Therefore, we propose that the interannual variability of storm trajectories does not explain the correlation of precipitation anomalies between South and East Asia.

An Apparent Contradiction

Storms are the proximate cause of precipitation, and yet Figure 9 shows that July-August storm trajectories behave differently from monthly rainfall anomalies. Both respond to blocking by the Himalayas, but storm trajectories are less responsive to other low topography. The propagation direction of storms is roughly a function of latitude, without the local heterogeneity observed in rainfall. Lastly, the direction of storm tracks does not change much from year to year. Storms produce rainfall and yet appear incapable of explaining its variations on longer time scales.

A solution can be identified by considering northeastern India and the southeastern Tibetan Plateau. Although Figure 9d shows that storms in the region come from the Yunnan Plateau to the east, local observations of δ^{18}O show a Bay of Bengal origin and isotopic depletion from convection (Gao et al., 2011). The seeming incompatibility of storms and vapor history helps us to isolate two separate processes: Storm propagation and moisture transport, both of which interact with mean flow in different ways. Storms are an eddy process superimposed on the mean state of the atmosphere. Synoptic depressions are steered by the upper troposphere and recycle whatever water vapor is locally available as they propagate. In contrast, because the scale height of water vapor is about 3 km, moisture transport depends on the state of the lower troposphere, where patterns of convergence change greatly from year to year (Annamalai and Slingo, 2001; Yoon and Chen, 2005). The fixity of storm trajectories points to changes in moisture transport as the root of interannual precipitation anomalies. In the next section, we propose a mechanism whereby such changes may induce coupling between South and East Asia.

2.8 Coupling between India and China

Proposed Mechanism

We propose that years of anomalously heavy July-August rainfall over the Himalayan Foothills reflect increased transport of water vapor from the Bay of Bengal. In turn, some of this surplus vapor travels via northeastern India to the southeastern Tibetan Plateau and northern Yunnan Plateau, and onward to the Yangtze Corridor. In Sampe and Xie, 2010, a linear baroclinic model (LBM) with prescribed heating over the Yangtze Corridor produced a zonal band of ascent, as well as anomalous descent to the north and south (Figures 13 and 14 of their paper). We suggest that increased latent heating associated with an increase in water vapor along the Yangtze Corridor may supply a diabatic forcing similar to the Sampe and Xie experiment, and that the resulting vertical velocity anomalies could ultimately generate the tripole pattern of rainfall anomalies over China seen in All-Asia JA EOF1. In months with reduced moisture transport across the Yunnan Plateau, we therefore propose that the decrease in latent heating along the Yangtze Corridor would lead to anomalous local descent and an inverted spatial pattern of rainfall anomalies. We further theorize that the coupling between India and China begins in July, when the onset of monsoon circulation in northern India initiates abundant moisture transport toward the Himalayas and onward to the Yunnan Plateau, and ends by September due to the shift of peak insolation back to the Equator.

The strong dipole of Indian summer rainfall variability, and corresponding shift in moisture transport, may reflect the existence of two stable summer ITCZ positions over India: An oceanic latitude at 5°N and a continental latitude at 15°N, as argued in Gadgil, 2003. In turn, the preferred configuration of the ITCZ may be influenced by the state of ENSO and Indian Ocean SST. A full moisture budget equates the *convergence* of moisture transport with the balance of precipitation and evaporation ($P - E$) (Trenberth, 1991; Chen and Bordoni, 2014). For our purposes, we assume that an additional influx of moisture from the Bay of Bengal must translate to increased precipitation downstream. Also, our subsequent model results suggest that evaporation is a negligible component of the moisture budget during the monsoon.

Potential Vorticity and Moist Static Energy

The linkage of July-August rainfall anomalies in India and China can be understood in terms of conservation of potential vorticity (PV). The PV of a column of air is given by

$$PV \approx \frac{(\xi + f)}{H} = \text{constant}$$

where $\xi = \frac{\partial v}{\partial x} - \frac{\partial u}{\partial y}$ is the relative vorticity of the column, $f = 2\Omega \sin\phi$ is the planetary vorticity at latitude ϕ due to the rotation rate of the Earth Ω, and H is the height of the column. This approximation is valid for a barotropic fluid. In this simple framework, heating acts by stretching a parcel and topography by compressing it. This helps to explain the sensitivity of flow even to low topography, and why moisture does not simply pass over the Arakan Mountains or Ghats.

A moisture parcel propagating northward from the Bay of Bengal cannot overcome the steep topography gradient of the Himalayas (which sharply decreases H). Instead, trajectories bifurcate between a westward branch towards Nepal ($\xi > 0$) and eastward forced channel flow between the Himalayas and Arakan Mountains into northeastern India ($\xi < 0$). These two trajectories encounter different topography. To the west, the Himalayas exceed 5 km of altitude, preventing access of moisture to the quasi-desertic Western Tibetan Plateau. To the east, the Himalayas are slightly lower, the slopes are less steep, and river valleys allow access to the high terrain of the eastern Tibetan Plateau and Yunnan Plateau. During monsoon season, moisture is observed to propagate as far as Lhasa and up the Brahmaputra and Zayu river valleys, which run from the Tibetan Plateau's southeastern edge into northeastern India (Gao et al., 2011; Yang et al., 2011a). Propagation may also be aided by the phenomenon described in Holton, 2004a that perturbations in easterly flow are damped whereas westerly flow excursions are amplified due to the gradient of planetary vorticity. Lastly, moist flow upslope may be abetted by surface heating, which should lift isentropes (Molnar and Emanuel, 1999; Privé and Plumb, 2007b).

In practice, we lack information about individual parcels. Instead, moist static energy h, and in particular the subcloud quantity h_b, reveals information about the strength and extent of the monsoon (Privé and Plumb, 2007a; Privé and Plumb, 2007b). h tracks total potential energy per kilogram of air (units of J kg^{-1} or m^2 s^{-2}), including latent heating, sensible heating and potential energy:

$$h = L_v q + c_p T + gz$$

L_v is the latent heat of vaporization of water and c_p the specific heat of dry air. In the absence of diabatic heating, this quantity remains conserved. Following Boos and Kuang, 2010, h is expressed in units of Kelvin by dividing by c_p. The resulting quantity can be interpreted as the equivalent temperature the parcel would have at sea level if all moisture was condensed. According to both idealized studies and observation, the maximum of h_b occurs at the northernmost extent of monsoon circulation (Emanuel, 1995; Privé and Plumb, 2007a; Boos and Kuang, 2010; Nie et al., 2010). Therefore, if our hypothesis of abundant moisture transport from the Bay of Bengal to northeastern India and onward is correct, we should observe an associated h_b maximum there that also diffuses downstream onto the southern Tibetan Plateau, northern Yunnan Plateau and beyond. The Himalayas amplify the h_b maximum along the Himalayan Foothills both by shielding warm air over India from cold air further north (Boos and Kuang, 2010) and by forced wind and moisture convergence. The Arakan Mountains may further induce convergence and strengthen h_b by restricting atmospheric flow into northeastern India to a narrow channel.

Supporting Evidence

APHRODITE shows that northeastern India experiences intense summer rainfall of 20 to 30 mm day^{-1} (Figure 1). Such rates require substantial moisture advection inland. Several past studies demonstrate this transport. As previously mentioned in sections 3b and 6d, studies of δ^{18}O of precipitation on the southeastern Tibetan Plateau suggest a Bay of Bengal origin (Yao et al., 2009; Gao et al., 2011; Yang et al., 2011a). Zhang et al., 2013, using AIRS satellite retrievals corroborated by radiosonde observations, find a deep layer of water vapor on the Tibetan Plateau in summer, with up to 15 mm of precipitable water over the southeastern Tibetan Plateau and northern Yunnan Plateau. In Medina et al., 2010, analysis of TRMM satellite data shows massive stratiform storms that advect moisture from the Bay of Bengal and wetlands of Bangladesh to the eastern Himalayas. Tagging of water in isotope-enabled GCM runs with the LMDZ model (which we use in the next section) show some transport of Bay of Bengal water vapor to central and southern China (Yao et al., 2013).

Direct observations of water vapor transport are unavailable. Several previous studies have suggested that changes in moisture transport over India induce precipitation anomalies in China (Feng and Zhou, 2012; Cao et al., 2014), but the resolution of the reanalysis products used in these studies (2.5° × 2.5° and 1.25° × 1.25° resolution respectively) may be unable to produce realistic fields of moisture transport. Pausata et al., 2011 argued that, during Heinrich events, East Asian speleothems record decreased Indian monsoon rainfall due to the downstream advection of isotopically enriched water vapor. However, their proposed pathway is further south over Indochina and does not correspond to All-Asia JA EOF1.

The covariation of precipitation anomalies in South and East Asia does not require a direct link, since each region could be independently responding to the same external forcing. Nonetheless, we propose a pathway of moisture transport from India to China across the Yunnan Plateau as a simple mechanism whose variations can explain our results. In the following section, we test our hypothesis by analyzing results from a model with high resolution around the Tibetan Plateau.

2.9 Model Results

Specifications

We employ the LMDZ5 (Laboratoire Météorologique de Dynamique - Zoom) model to investigate the proposed mechanism, specifically the LMDZ5A package used in Coupled Model Intercomparison Project Phase 5 (CMIP5) as part of the Fifth Assessment Report of the Intergovernmental Panel on Climate Change (IPCC AR5, Christensen et al., 2011). LMDZ is the flagship atmospheric model of Institut Pierre Simon Laplace (IPSL). Details of model function are available in Hourdin et al., 2006 and Hourdin et al., 2012. The run analyzed below uses the AMIP protocol, which fixes CO_2 and prescribes monthly fields of SST and sea ice with some interannual variability. A high-resolution nested grid (~50 km resolution) is included over East Asia (0°to 55°N and 60°E to 130°E) inside of a coarse global grid.

The transition from coarse to fine resolution occurs over an area far outside of the region of interest in order to avoid edge effects. In addition, winds are nudged to ECMWF reanalysis with a dissipation time constant τ of 1 hour/4 hours (inside/outside zoomed region).

The combination of zoomed grid and nudged winds substantially improves precipitation and δ^{18}O climatologies relative to observation (Gao et al., 2011). An isotope-enabled version of LMDZ (LMDZ-iso) has been tested across a range of climates with good performance (Risi et al., 2010). LMDZ has also been extensively tested in the vicinity of the Tibetan Plateau and consistently outperforms other isotopically-enabled models (Gao et al., 2011; Lee et al., 2012; Eagle et al., 2013; Gao et al., 2013; Yao et al., 2013). We present results for the year 2006 as a case study, leaving in-depth testing and investigation of interannual variability for future runs. Rainfall climatology roughly resembles observations from APHRODITE, with correct seasonality over South and East Asia (not shown). Figure 10b shows that LMDZ produces a field of 200-mb level wind similar to NCEP reanalysis (Figure 10a).

Moist Static Energy and Moisture Transport in LMDZ

To analyze model treatment of the South Asian monsoon, we calculate near-surface moist static energy h_b, and also streamlines of column-integrated moisture transport $\vec{Q} = (Q_u, Q_v)$ for each month from June to September (Figure 11), where $Q_u = \frac{1}{g}\int qu \, \mathrm{d}p$ and $Q_v = \frac{1}{g}\int qv \, \mathrm{d}p$ (Trenberth, 1991). The direction of $\vec{Q}$ is mostly dictated by circulation in the lower troposphere, where specific humidity is much higher. Our calculated values agree with past estimates such as in Feng and Zhou, 2012.

LMDZ's estimate of h_b can be compared to the July climatology of 10-meter moist static energy in Figure 1 of Nie et al., 2010 and Figure 3a of Boos and Hurley, 2013, which it mostly resembles. In July and August, LMDZ correctly generates a maximum of moist static energy along the Himalayan Foothills and east of the Hindu Kush, a feature absent from almost all CMIP5 GCMs (Boos and Hurley, 2013). This maximum is due to the abundant advection of moisture from the Bay of Bengal by cyclonic mean circulation. In June, the h_b maximum is instead situated over the Arabian Ocean and Bay of Bengal because winds over India are westerly, which brings dry air from the continental interior. Bay of Bengal SST also peaks in May and June according to observation (Bhat et al., 2004). In September, h_b is lower everywhere due to decreased insolation, although cyclonic circulation and northward moisture transport from the Bay of Bengal persist in weakened form. Over the northern Bay of Bengal, peak column-integrated moisture transport across 22°N onto land is 314.5 kg $\mathrm{m}^{-1}\mathrm{s}^{-1}$ in July, 262.8 kg $\mathrm{m}^{-1}\mathrm{s}^{-1}$ in August and 206.9 kg $\mathrm{m}^{-1}\mathrm{s}^{-1}$ in September. This agrees with the observation that water vapor from the Bay of Bengal still reaches Lhasa in September, but less frequently than in July and August (Gao et al., 2011). Abundant moisture transport from the Bay of Bengal to the Himalayan Foothills requires cyclonic circulation over India and sufficient heating. In this run, these conditions are only met in July and August.

LMDZ also shows moisture transport from India downstream to China in July and August, and corresponding local maxima in moist static energy over the southeastern Tibetan Plateau and Sichuan Basin. In the model, there is a positive bias in moist static energy and rainfall over the central Tibetan Plateau relative to observation. Meanwhile, in northeastern India, moist static energy is underestimated by 20 to 25K, and rainfall by 20 mm day^{-1}. Therefore, we suggest that the route of moisture transport from the Bay of Bengal to the Yangtze Corridor is shifted northward in LMDZ by about 5 degrees of latitude, and that the actual route is through northeastern India and across the Yunnan Plateau.

2.10 Conclusion

In this work, we find that July-August monthly rainfall anomalies in South and East Asia are correlated across thousands of kilometers, as shown by point-to-point correlations, an agreement map method and EOF analysis. Further investigation with lag-lead correlations of rainfall shows that interannual variations in storm tracks cannot explain this result. Instead, we postulate that a pathway of moisture transport exists from the Bay of Bengal to the Yangtze Corridor across the northern Yunnan Plateau. Changes in this transport produce a coherent band of rainfall anomalies connecting northeastern India and central China, and also induce changes of opposite sign in the “Monsoon Zone,” North China and South China. This link is confined to July and August, when cyclonic monsoon circulation sets in over India and insolation remains high. We propose All-Nepal and Yangtze monsoon rainfall as two local indices that reflect this leading mode of Asian rainfall variability. The LMDZ model, featuring a high resolution grid around the Tibetan Plateau, produces a realistic monsoon climatology and confirms basic elements of our hypothesis, which offers promise for future modeling efforts.

It is important to understand the role of storms. On a daily time scale, the passage of a storm induces a positive rainfall anomaly. They also alter their synoptic environment by processes such as the release of CAPE, such that storms and atmospheric conditions evolve in tandem. Yet, at the monthly level, our results suggest that the leading mode of July-August rainfall variability in Asia cannot be attributed to a change in storm behavior. Storms function as a passive, stochastic process that registers the state of the atmosphere by precipitating available water vapor. Since the scale height of water vapor is about 3 km, lower tropospheric conditions dictate its distribution. Increased moisture transport to the Himalayas requires corresponding changes in circulation, lower-level convergence and also in the distribution of near-surface moist static energy, which is correlated with seasonal rainfall anomalies in monsoon regions (Hurley and Boos, 2013). In contrast, the steering direction of storms remains relatively constant between years. The agreement of storm tracks with 200-mb level winds suggests that their propagation across Asia is generally an upper tropospheric process, with some regional exceptions. Therefore, they are insensitive to orography besides the high barrier of the Himalayas. The sharp spatial gradients of rainfall and monthly rainfall anomalies reflect sensitivity to lower tropospheric processes, where topography dictates flow.

The lack of observations along the proposed route of moisture transport hinders the corroboration of our theory. Many locations traversed are remote or politically sensitive, such as the eastern Tibetan Plateau in China, Arunachal Pradesh in India or Kachin State in Myanmar. Meteorological data alone may be insufficient to characterize the behavior of water vapor. Studies have compiled event-based measurements of isotopes at downstream sites in China (Yang et al., 2011b; Wu et al., 2015), but the complexity of their δ^{18}O signals makes interpretation of parcel origin and history a challenge. An ideal study would feature daily or sub-daily measurement of water vapor at multiple sites en route, including northeastern India, the Yunnan Plateau and Sichuan, similar to measurements performed at several sites along the Brahmaputra River valley on the Tibetan Plateau by Gao et al., 2011.

We note an additional connection between Bay of Bengal sea surface temperature (SST) and Indian rainfall variability. Using HadSST 3.1 (Kennedy et al., 2011a; Kennedy et al., 2011b), which features SST from 1850 to present on a 5° × 5° grid, we test the correlation of July-August rainfall in India at every point with SST in the northern Bay of Bengal (defined as the mean of SST at 87.5°E 22.5°N and 92.5°E 22.5°N). The resulting pattern again resembles All-Asia JA spatial EOF1 (not shown), with positive correlations over the Himalayan Foothills, eastern Tibetan Plateau and Yangtze Corridor and negative correlation over the "Monsoon Zone", all exceeding a 95% confidence level ($|r| > .18$). However, the time series of northern Bay of Bengal SST is not significantly correlated with All-Asia JA temporal EOF1 ($r = .11$) or India temporal EOF1 ($r = .09$). This result is robust to different definitions of Bay of Bengal SST. Indian monsoon rainfall variability and Bay of Bengal SST have previously been shown to covary on weekly time scales (Vecchi and Harrison, 2002; Han et al., 2006). The covariance of local SST and monthly rainfall anomalies implies a mutual response to external forcing that we will investigate in future work.

The results above have only briefly considered the source of the coupled variability described above. Previous work has shown the ability of El Niño conditions in the central Pacific to induce droughts over India in following summer (Kumar et al., 2006), as well as circulation and rainfall anomalies over East Asia via the "capacitor effect" (Xie et al., 2009). We found no significant correlation between the Niño 3.4 index (ONI) in December and the leading July-August modes of South and East Asian rainfall variability (All-Asia JA EOF1, India JA EOF1 and China JA EOFs 1 and 2; correlations shown in Table 2). However, the correlation of December Niño 3.4 and All-India Monsoon Rainfall exceeds a 95% confidence level, suggesting that ENSO-related anomalies may have a particular spatial character distinct from India EOF1. Both equatorial Indian Ocean zonal wind and SST anomalies have been linked to variations in rainfall over India (Ihara et al., 2007; Mishra et al., 2012). Thus, leading modes of global and regional variability such as the Western Pacific Anticyclone (Kosaka et al., 2011), the Pacific Decadal Oscillation (Mantua and Hare, 2002) and the Indian Ocean Dipole (Saji et al., 1999) may influence the Indian monsoon by altering circulation or SSTs. However, the atmospheric response is sensitive to the exact distribution of such anomalies (Xie et al., 2009).

Statistically significant 20th century trends in rainfall have been found across Asia (Christensen et al., 2011; Singh et al., 2014). The leading temporal EOFs in our study (Figures

6 and 7) generally show that precipitation has increased along the Himalayan Foothills and China south of 30°N (Hunan and Jiangxi Provinces in particular), and decreased over the "Monsoon Zone" and in northern China around 35°N (particularly Shaanxi and Henan Provinces). This agrees with previous studies that discuss a "South Flood North Drought" pattern in China (Ding et al., 2008) and a decrease in All-India Monsoon Rainfall since the 1970s (Annamalai et al., 2013). These results could reflect a change in mean moisture transport from the Bay of Bengal to China in the past few decades. A better physical understanding of the coupling between the South and East Asian monsoons may improve projections of 21st century precipitation changes in Asia, which remain uncertain (Christensen et al., 2011).

2.11 Acknowledgment

This work was supported by NSF funds EAR-0909195 and EAR-1211925. We also acknowledge NSFC (National Natural Science Foundation of China) grant #40921120406 for encouraging the feedback and support of colleagues in China. We thank Jinqiang Chen, Peter Molnar and two anonymous reviewers for their valuable suggestions. APHRODITE precipitation data is publicly available at `http://www.chikyu.ac.jp/precip/index.html`. FERRET, a NOAA product, was used for data analysis and preliminary plot generation. The official All-India Monsoon Rainfall time series was obtained from the Indian Meteorological Department (IMD) website at `http://www.imd.gov.in/section/nhac/dynamic/Monsoon_frame.htm`. The Oceanic Niño Index (ONI) time series was retrieved from NOAA at `http://www.cpc.ncep.noaa.gov/products/analysis_monitoring/ensostuff/ensoyears.shtml`. Monthly 200 mb-level reanalysis winds were obtained from NCEP/NCAR reanalysis available at `http://www.esrl.noaa.gov/psd/data/gridded/data.ncep.reanalysis.derived.surface.html`. Bay of Bengal SST was obtained from HadSST 3.1, provided by the UK Met Office at `http://www.metoffice.gov.uk/hadobs/hadsst3/data/download.html`. Data, figures used and animations of relevant data are available at: `http://www.atmos.berkeley.edu/~jessed/myfigures.html`.

2.12 Tables and Figures

Table 2.1: The 22 reference points used in the point to point comparisons and agreement map.

Region	#	Nearest City	Long	Lat	JA Precip (mm day^{-1})	St. Dev.	STN
Himalayan Foothills + Bangladesh	1	Chittagong	91.9°E	22.4°N	16.55	6.58	.88
	2	Kathmandu	85.4°E	27.6°N	12.34	3.33	5.09
	3	Patna	85.1°E	25.6°N	7.78	2.92	2.42
	4	Eastern Assam	95.1°E	27.4°N	12.62	3.27	1.04
	5	Nyingchi	94.4°E	29.6°N	3.71	1.47	1.28
“Monsoon Zone”	6	Bhubaneswar	85.9°E	20.4°N	10.06	3.04	1.98
	7	Durg	81.4°E	21.1°N	9.26	2.98	1.83
	8	Ahmedabad	72.6°E	23.1°N	7.11	3.85	1.74
	9	Karachi	67.1°E	24.9°N	1.68	2.01	.86
South India	10	Bangalore	77.6°E	12.9°N	3.04	1.78	1.89
	11	Kumbakonam	79.4°E	10.9°N	2.29	1.62	2.94
South China	12	Namh Dinh	106.1°E	20.4°N	7.64	3.80	1.56
	13	Shenzhen	114.1°E	22.6°N	9.78	4.41	1.01
	14	Taipei	121.6°E	25.1°N	6.59	4.62	3.36
Yangtze Corridor + Korea + Japan	15	Chongqing	106.4°E	29.6°N	4.41	2.15	1.49
	16	Enshi	109.4°E	30.4°N	5.80	3.09	1.32
	17	Anqing	117.1°E	30.6°N	4.58	3.03	1.42
	18	Changzhou	119.9°E	31.9°N	4.39	2.37	1.14
	19	Jinju (Korea)	128.1°E	35.1°N	7.66	4.10	1.67
	20	Tokyo	139.4°E	35.9°N	5.35	2.86	3.33
North China	21	Baotou	109.9°E	40.6°N	2.47	1.26	1.08
	22	Chengde	117.9°E	40.9°N	4.50	1.99	1.98

Table 2.2: July-August correlation coefficients r from 1951 to 2007 of All-Nepal rainfall, All-India rainfall (calculated from APHRODITE),"Monsoon Zone" rainfall and Yangtze rainfall (mean rainfall over the region bounded by (104.5°E 29°N), (108°E 32°N), (120°E 34°N) and (122°E 31.5°N)), as well as Oceanic Niño Index (ONI) in preceding December, or equivalently the N(0)-D(0)-J(1) mean of Niño 3.4 (SST anomaly averaged over the region 5°S-5°N and 120°W-170°W). Each time series is correlated with one another, as well as with All-Asia JA temporal EOF1, India JA temporal EOF1, China JA temporal EOFs 1 & 2 and official July-August All-India Monsoon Rainfall from the Indian Meteorological Department (IMD). Although All-Nepal Monsoon Rainfall is reliable only for 1961-2007 due to station coverage limitations and the Monsoon Zone time series likewise degrades after 1970, all 57 years are used for consistency, and results are not substantially affected. July and August are treated as separate time points except for correlation with ONI, which uses a single value per year. 95% and 99% confidence levels are indicated by bold font and asterisks respectively, and are calculated to account for the shared autocorrelation between time series, which reduces the effective degrees of freedom (Livezey and Chen, 1983).

Index	All-Nepal	All-India	MZ	YZ	EOF1 (All-Asia)	EOF1 (India)	EOF1/2 (China)	All-India (IMD)
All-Nepal	**1***	-.07	**-.52***	**.28***	**.59***	**.70***	**.37***/.14	.02
All-India	-.07	**1***	**.76***	-.08	**-.43***	**-.54***	-.04/ **-.27***	**.94***
Monsoon Zone	**-.52***	**.76***	**1***	**-.23**	**-.74***	**-.90***	**-.27*/-.30***	**.67***
Yangtze	**.28***	-.08	**-.24**	**1***	**.62***	**.31***	**.62***/**.61***	-.11
Oceanic Niño Index	.11	**.26**	.15	.15	.10	-.02	.17/-.11	.24

Table 2.3: All-Nepal Monsoon Rainfall for every July and August, 1951-2007, calculated as an area average over Nepal. Precipitation is in mm day^{-1}. The index is given by the monthly precipitation anomaly averaged over Nepal in units of standard deviation. Station quality improves dramatically starting in 1961 such that use of the 1951-1960 component is discouraged. 1961-2007 values are used to calculate monthly average and standard deviation. July: 11.34 mm day^{-1} mean, st. dev. of 1.71 mm day^{-1}; in August, 9.91 mean, st. dev. of 1.54 mm day^{-1}. The inaccuracy of the index from 1951 to 1960 is reflected by the relatively high standard deviation of those points.

Month	Precip	Index	Month	Precip	Index	Month	Precip	Index
July 1951	*7.46*	*-2.27*	July 1970	12.85	0.88	July 1989	12.79	0.85
Aug 1951	*8.27*	*-1.07*	Aug 1970	8.40	-0.98	Aug 1989	9.30	-0.40
July 1952	*6.09*	*-3.07*	July 1971	9.04	-1.34	July 1990	12.96	0.95
Aug 1952	*11.58*	*1.08*	Aug 1971	9.53	-0.25	Aug 1990	9.74	-0.11
July 1953	*17.91*	*3.84*	July 1972	11.35	0.01	July 1991	8.12	-1.88
Aug 1953	*5.96*	*-2.57*	Aug 1972	6.62	-2.14	Aug 1991	10.99	0.70
July 1954	*13.68*	*1.37*	July 1973	8.23	-1.82	July 1992	9.19	-1.26
Aug 1954	*10.49*	*0.38*	Aug 1973	8.92	-0.65	Aug 1992	9.24	-0.44
July 1955	*19.09*	*4.53*	July 1974	12.94	0.94	July 1993	9.17	-1.27
Aug 1955	*7.45*	*-1.60*	Aug 1974	10.79	0.57	Aug 1993	11.46	1.01
July 1956	*7.13*	*-2.46*	July 1975	12.98	0.96	July 1994	9.51	-1.07
Aug 1956	*9.95*	*0.02*	Aug 1975	8.61	-0.85	Aug 1994	10.09	0.12
July 1957	*12.72*	*0.81*	July 1976	9.36	-1.16	July 1995	10.76	-0.34
Aug 1957	*8.54*	*-0.89*	Aug 1976	10.26	0.23	Aug 1995	10.89	0.64
July 1958	*8.58*	*-1.61*	July 1977	10.14	-0.70	July 1996	12.41	0.63
Aug 1958	*14.77*	*3.16*	Aug 1977	10.31	0.26	Aug 1996	11.22	0.85
July 1959	*8.23*	*-1.82*	July 1978	12.66	0.77	July 1997	10.67	-0.39
Aug 1959	*7.02*	*-1.88*	Aug 1978	8.79	-0.73	Aug 1997	9.48	-0.28
July 1960	*11.05*	*-0.17*	July 1979	11.60	0.15	July 1998	13.51	1.27
Aug 1960	*8.54*	*-0.89*	Aug 1979	8.51	-0.91	Aug 1998	13.83	2.55
July 1961	9.59	-1.02	July 1980	12.46	0.66	July 1999	11.19	-0.09
Aug 1961	12.47	1.66	Aug 1980	9.46	-0.29	Aug 1999	11.54	1.06
July 1962	9.79	-0.91	July 1981	13.06	1.01	July 2000	11.01	-0.19
Aug 1962	13.45	2.30	Aug 1981	9.44	-0.31	Aug 2000	11.48	1.02
July 1963	10.90	-0.26	July 1982	9.22	-1.24	July 2001	10.90	-0.26
Aug 1963	11.67	1.14	Aug 1982	9.70	-0.14	Aug 2001	10.15	0.15
July 1964	13.43	1.22	July 1983	10.78	-0.33	July 2002	12.18	0.49
Aug 1964	8.84	-0.70	Aug 1983	9.41	-0.33	Aug 2002	9.41	-0.33
July 1965	10.25	-0.64	July 1984	14.45	1.82	July 2003	12.97	0.95
Aug 1965	10.25	0.22	Aug 1984	7.32	-1.69	Aug 2003	9.41	-0.33
July 1966	9.78	-0.91	July 1985	13.45	1.23	July 2004	12.73	0.81
Aug 1966	11.88	1.28	Aug 1985	9.65	-0.17	Aug 2004	7.41	-1.63
July 1967	11.40	0.04	July 1986	11.44	0.06	July 2005	10.14	-0.70
Aug 1967	8.72	-0.78	Aug 1986	7.82	-1.36	Aug 2005	10.19	0.18
July 1968	10.93	-0.24	July 1987	13.36	1.18	July 2006	9.16	-1.27
Aug 1968	8.58	-0.87	Aug 1987	10.87	0.62	Aug 2006	7.78	-1.39
July 1969	9.94	-0.82	July 1988	14.52	1.86	July 2007	13.67	1.36
Aug 1969	9.97	0.04	Aug 1988	12.38	1.60	Aug 2007	9.68	-0.15

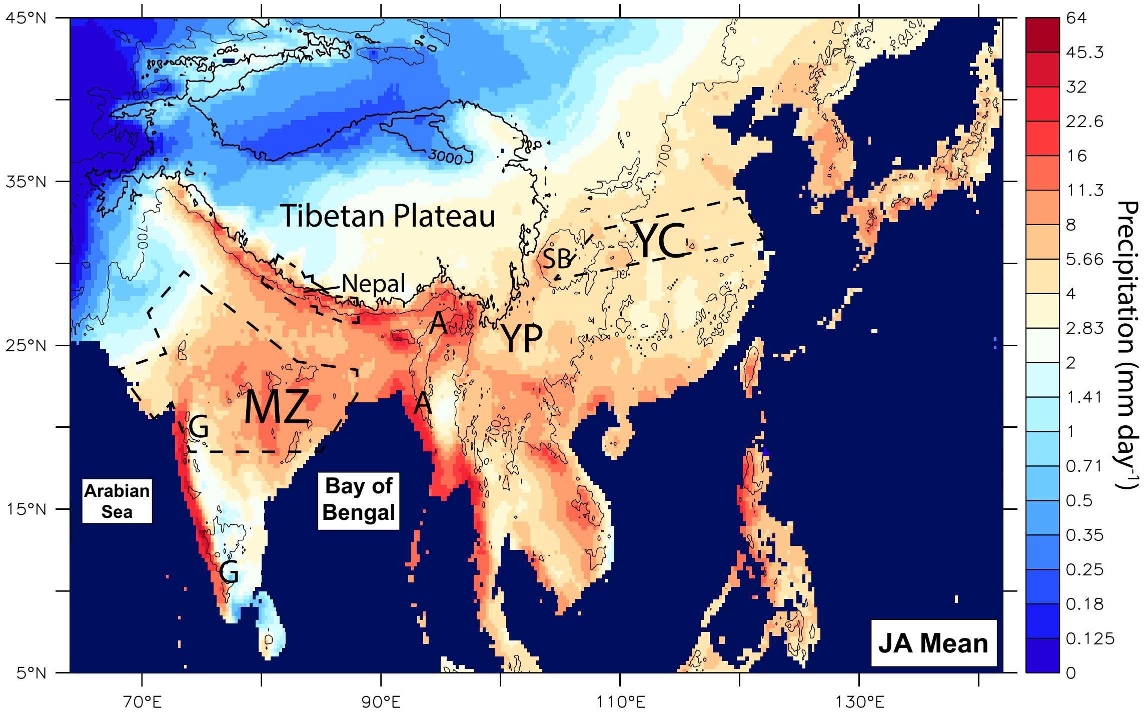

Figure 2.1: July-August mean precipitation from APHRODITE (units of mm day^{-1}, 1951-2007) plotted with a log base 2 color scale. Topography contours of 700 and 3000 meter elevation are superimposed (light and thick contour respectively). No data are available over water (deep blue shading) since APHRODITE is a composite of station data. Important regions are abbreviated as MZ - "Monsoon Zone" and YC - Yangtze Corridor. Key topographic features are labeled as follows: A - Arakan Mountains; G - Ghats; YP - Yunnan Plateau; SB - Sichuan Basin.

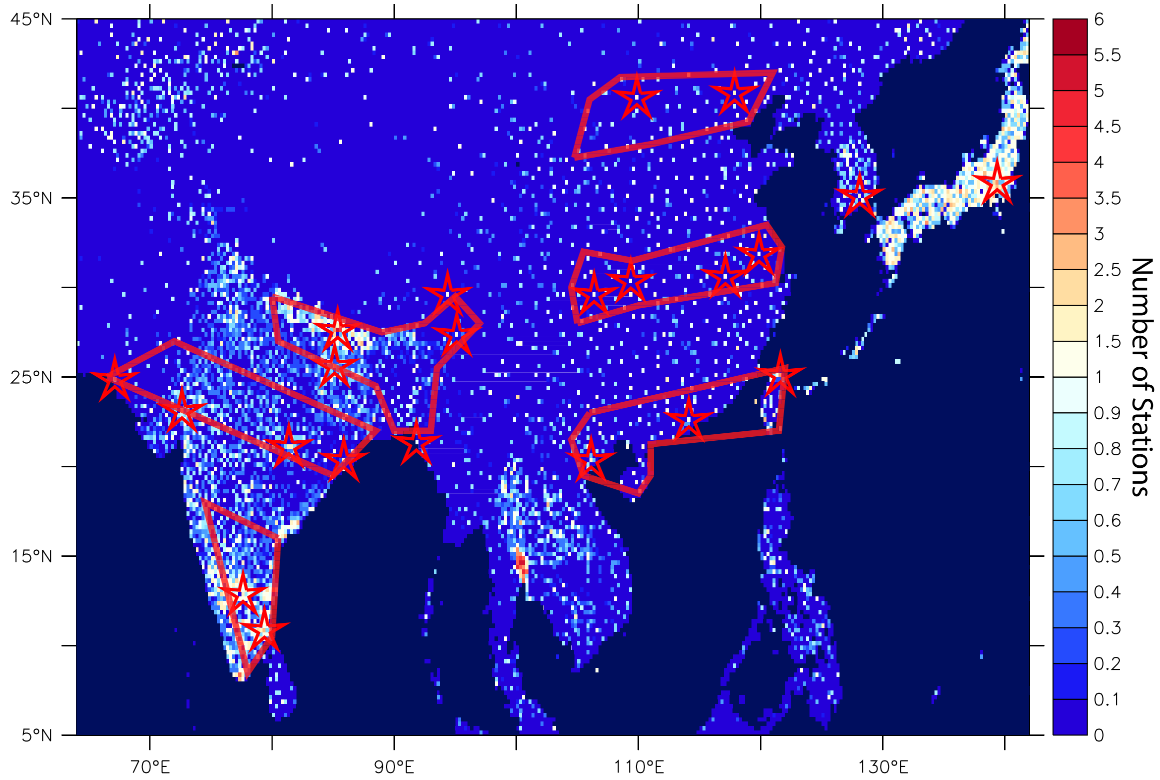

Figure 2.2: Mean station coverage STN in APHRODITE (1951-2007), with the 22 reference points (stars) and 6 regions (Himalayan Foothills, "Monsoon Zone," South India, South China, Yangtze Corridor and North China) used to calculate correlations and agreement maps.

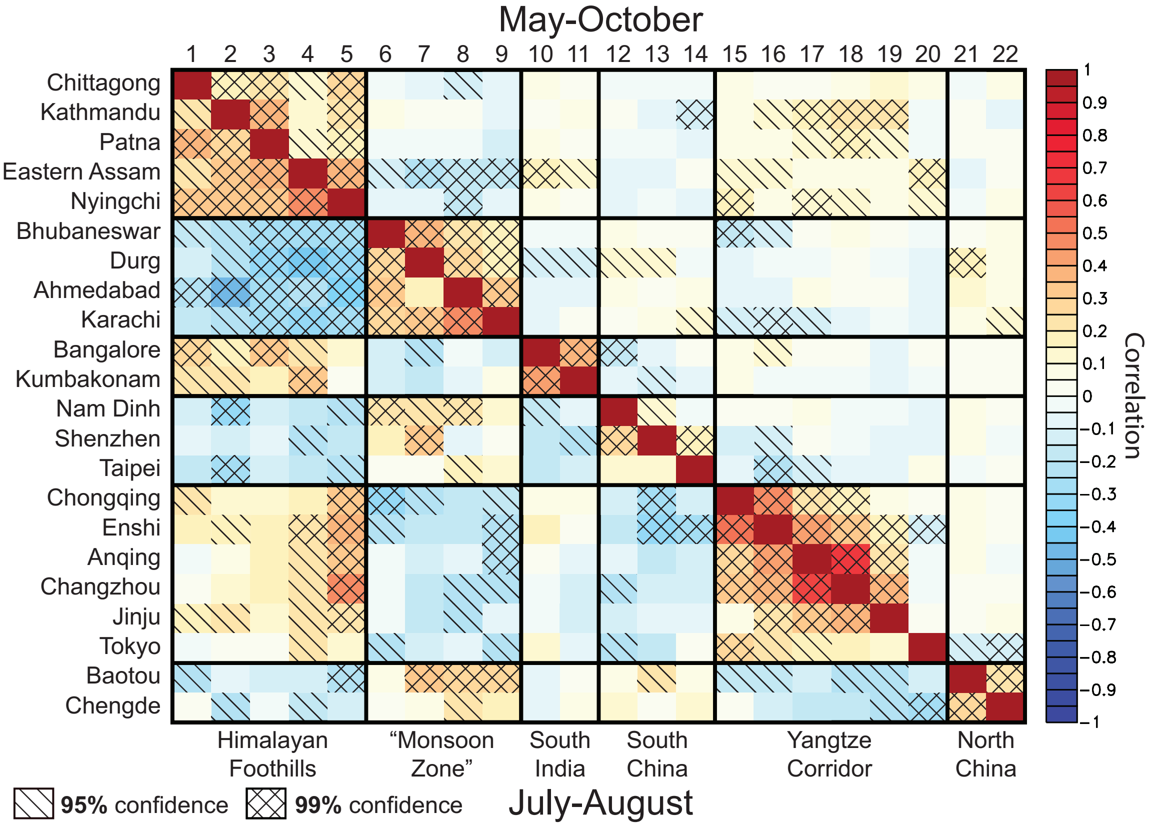

Figure 2.3: Correlation coefficient r of normalized monthly precipitation anomaly time series P'' between each of the 22 reference points for the years 1951-2007. Each monthly anomaly is treated as an independent time point. Bottom-left: July-August (JA, 114 time points). Upper-right: May-October (MJJASO, 342 time points). Confidence levels above 95% and 99% are indicated by single and double diagonal hatches respectively. Given degrees of freedom n, the threshold for significance is listed. July-August ($n = 112$) - 95%/99%: $|r| > .184/.240$. May-October ($n = 340$) - 95%/99%: $|r| > .106/.139$. Shared autocorrelation between monthly rainfall anomaly time series is small and does not affect the number of effective degrees of freedom. Region-to-region correlations reproduce point-to-point results closely (not shown).

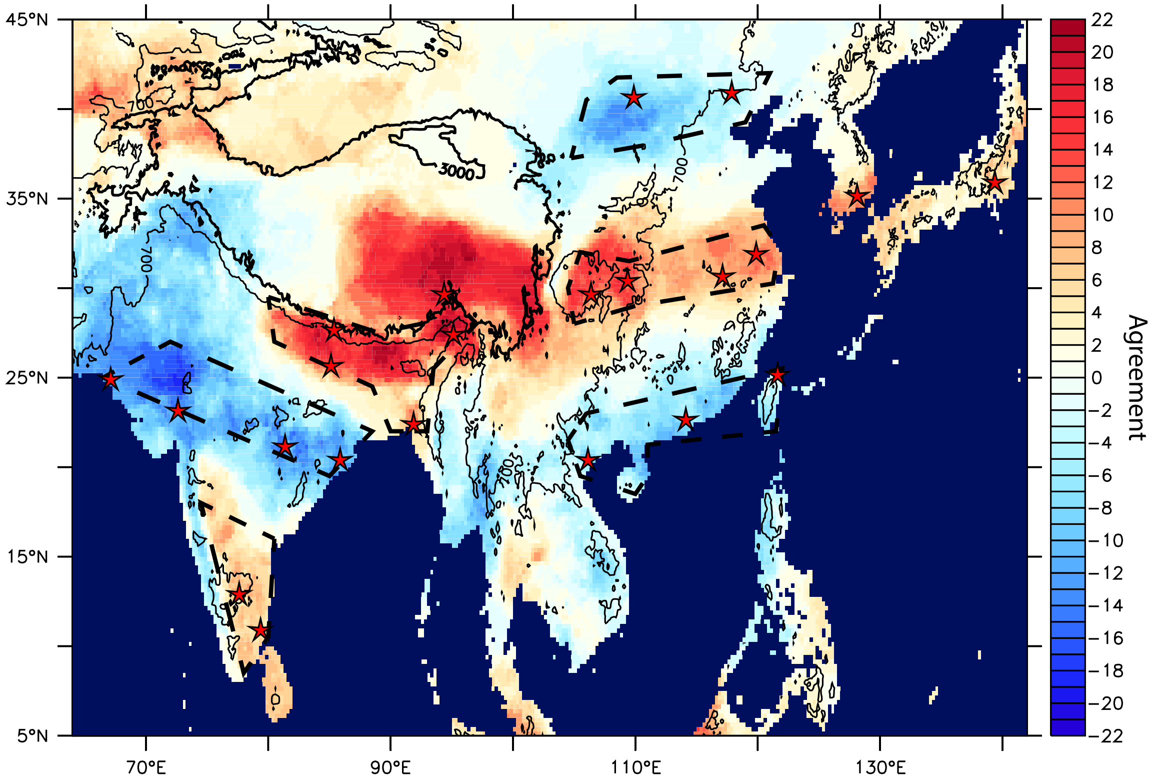

Figure 2.4: Agreement map $A(x, y)$ of July-August rainfall anomalies predicted by all 22 reference points, calculated using method described in Section 3b, with 3000 meter and 700 meter topography isolines superimposed (thick and thin lines respectively) and reference points marked with red stars.

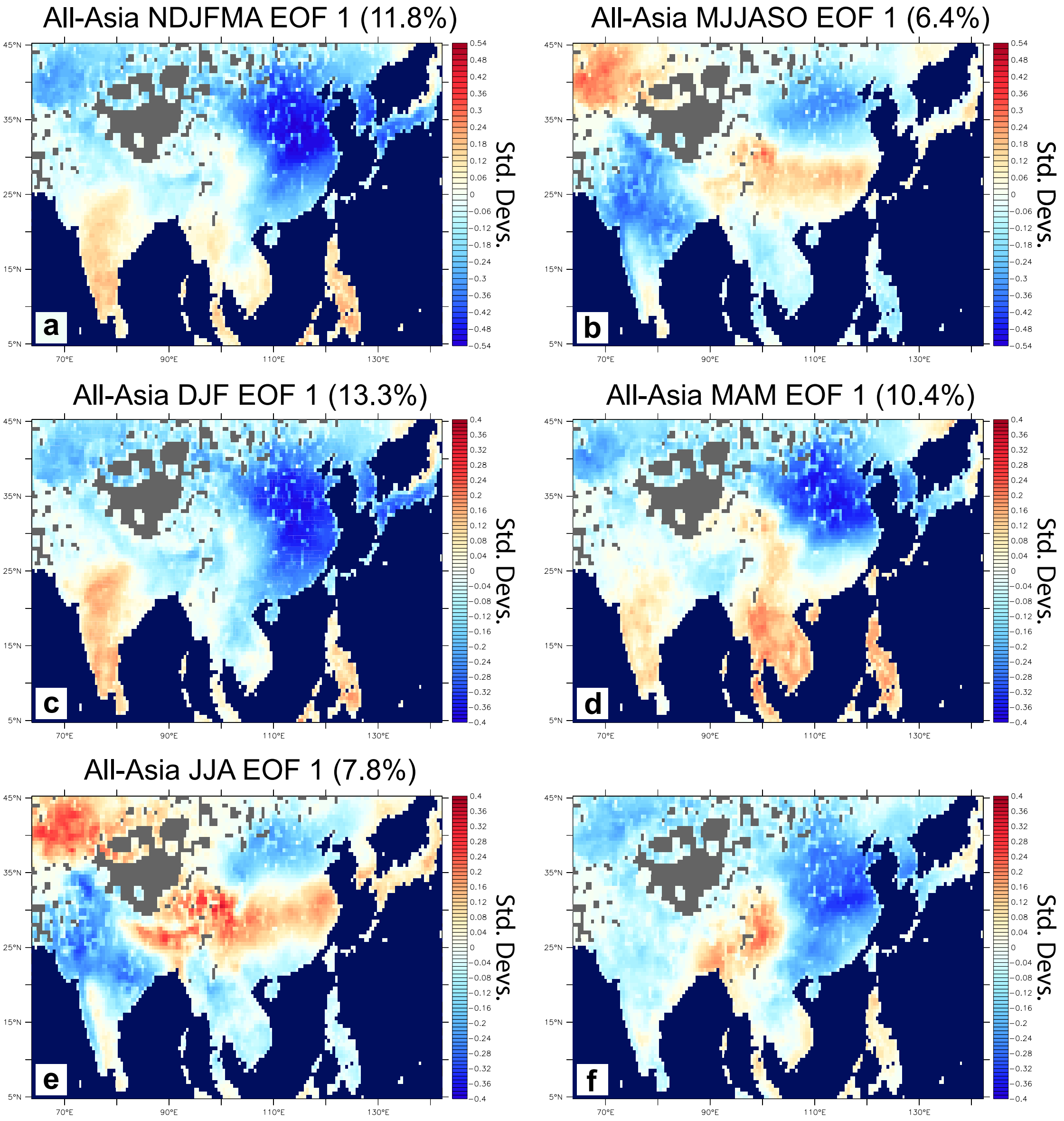

All-Asia NDJFMA EOF 1 (11.8%)

All-Asia MJJASO EOF 1 (6.4%)

All-Asia DJF EOF 1 (13.3%)

All-Asia MAM EOF 1 (10.4%)

All-Asia JJA EOF 1 (7.8%)

Figure 2.5: EOF 1 of normalized anomaly precipitation for the region 64E-142E and 5N-45N for June through September separately with .5° × .5° resolution.

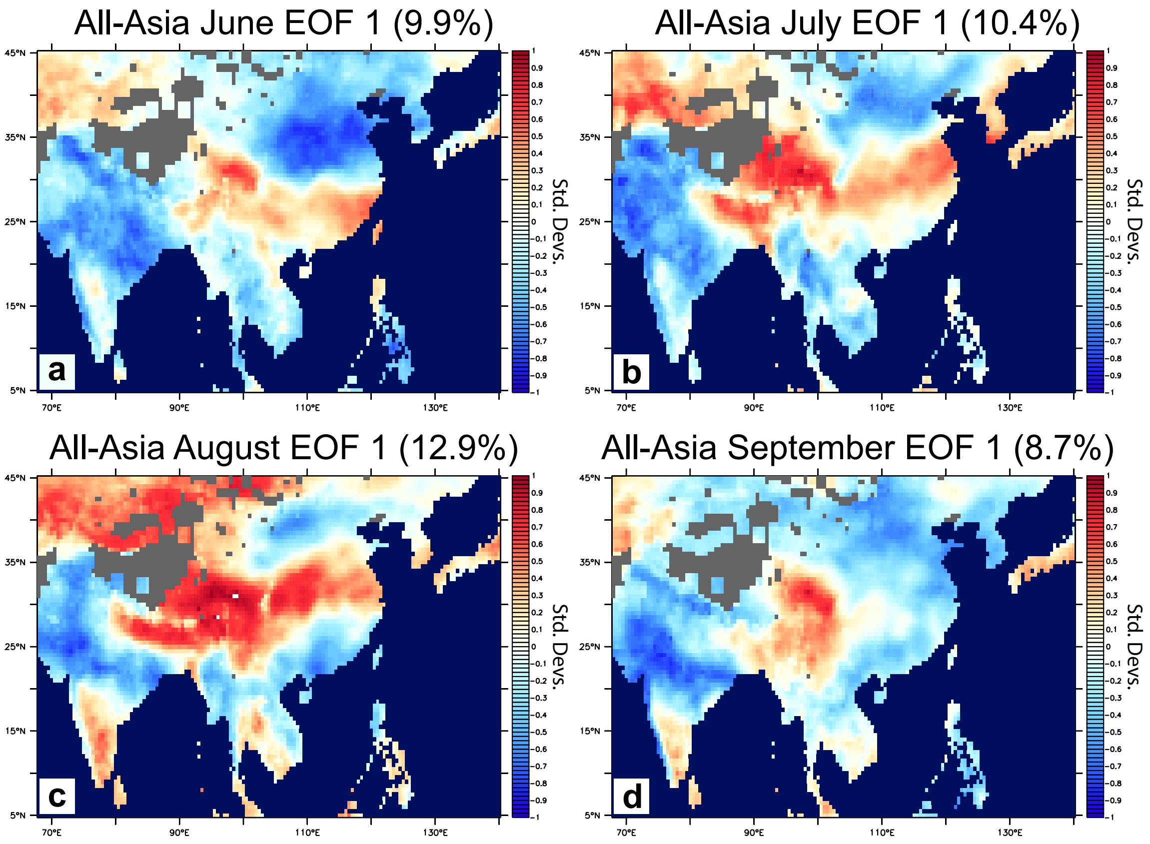

All-Asia June EOF 1 (9.9%)

All-Asia July EOF 1 (10.4%)

All-Asia August EOF 1 (12.9%)

All-Asia September EOF 1 (8.7%)

Figure 2.6: EOF1 of normalized anomaly precipitation computed separately for June, July, August and September (units of standard deviation) for the All-Asia region (68°E-140°E and 5°-45°N) with .5° × .5° resolution for 1951-2007. Percentage of variance explained by each EOF is listed alongside.

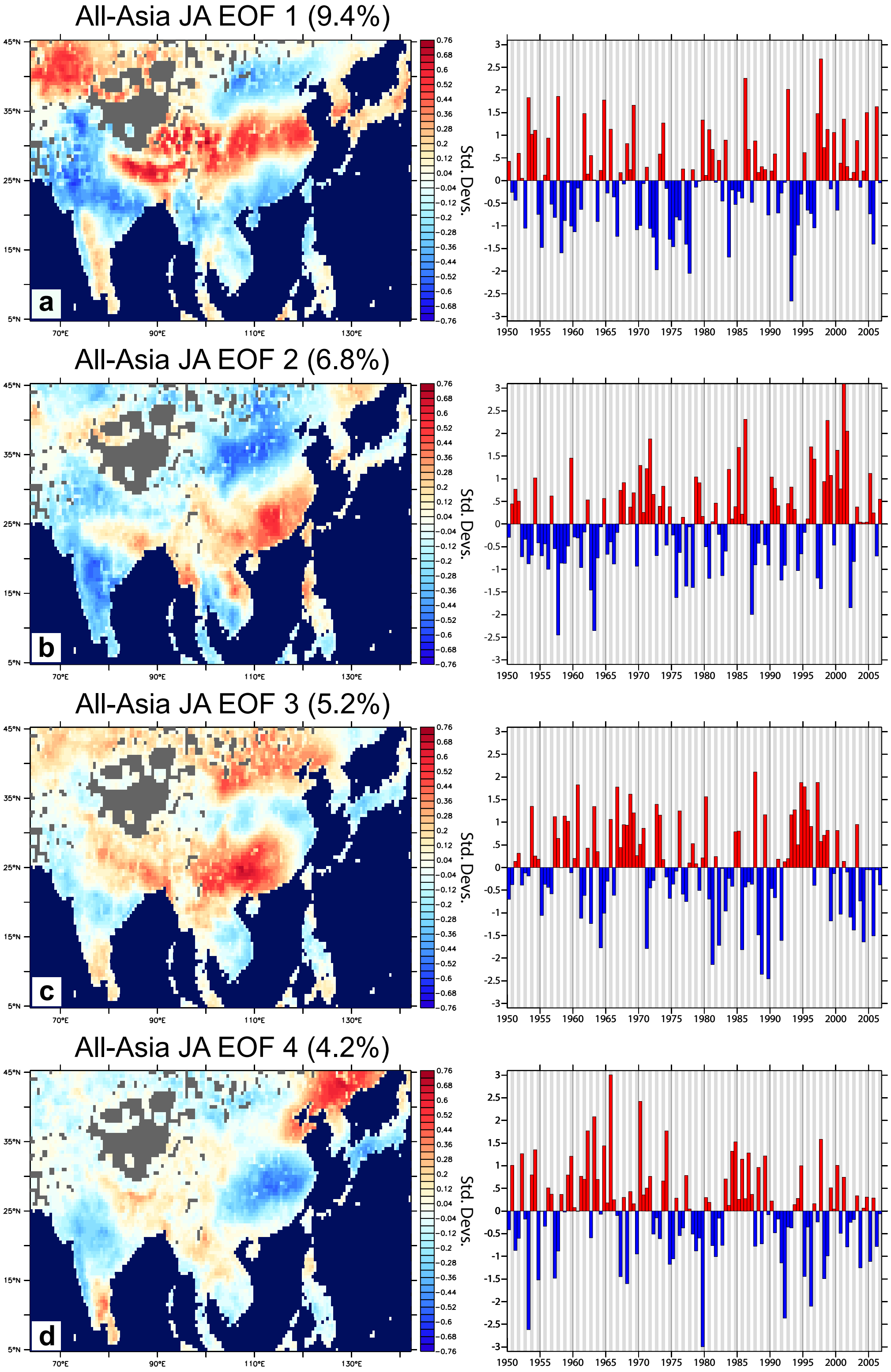

Figure 2.7: Leading spatial and temporal EOFs of July-August normalized anomaly precipitation P'' for the All-Asia region (64°E-142°E and 5°N-45°N) with .5° × .5° resolution for 1951-2007 (114 time points). Percentage of variance explained by each EOF is listed alongside. July (white shading) and August (gray shading) value of temporal EOF are shown separately. Time series are normalized to unit variance ($\sigma = 1$).

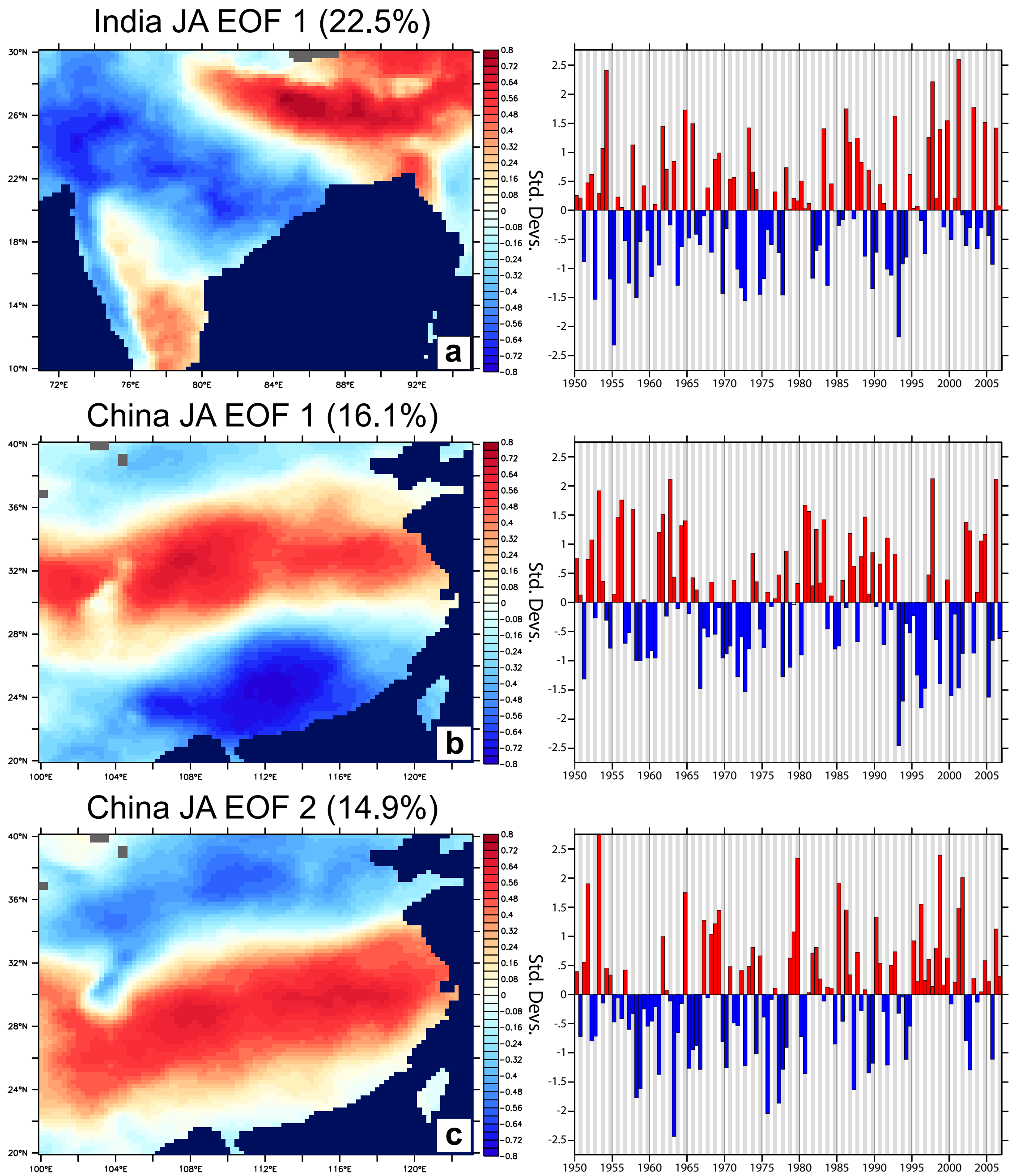

Figure 2.8: Leading spatial and temporal EOFs of July-August normalized anomaly precipitation P'' for India (71°E-95°E and 10°N-30°N) and China (100°E-123°E and 20°N-40°N) with .25° × .25 textdegree resolution for 1951-2007 (114 time points). Percentage of variance explained by each EOF is listed alongside. July (white shading) and August (gray shading) are both shown. Time series are normalized to unit variance ($\sigma = 1$).

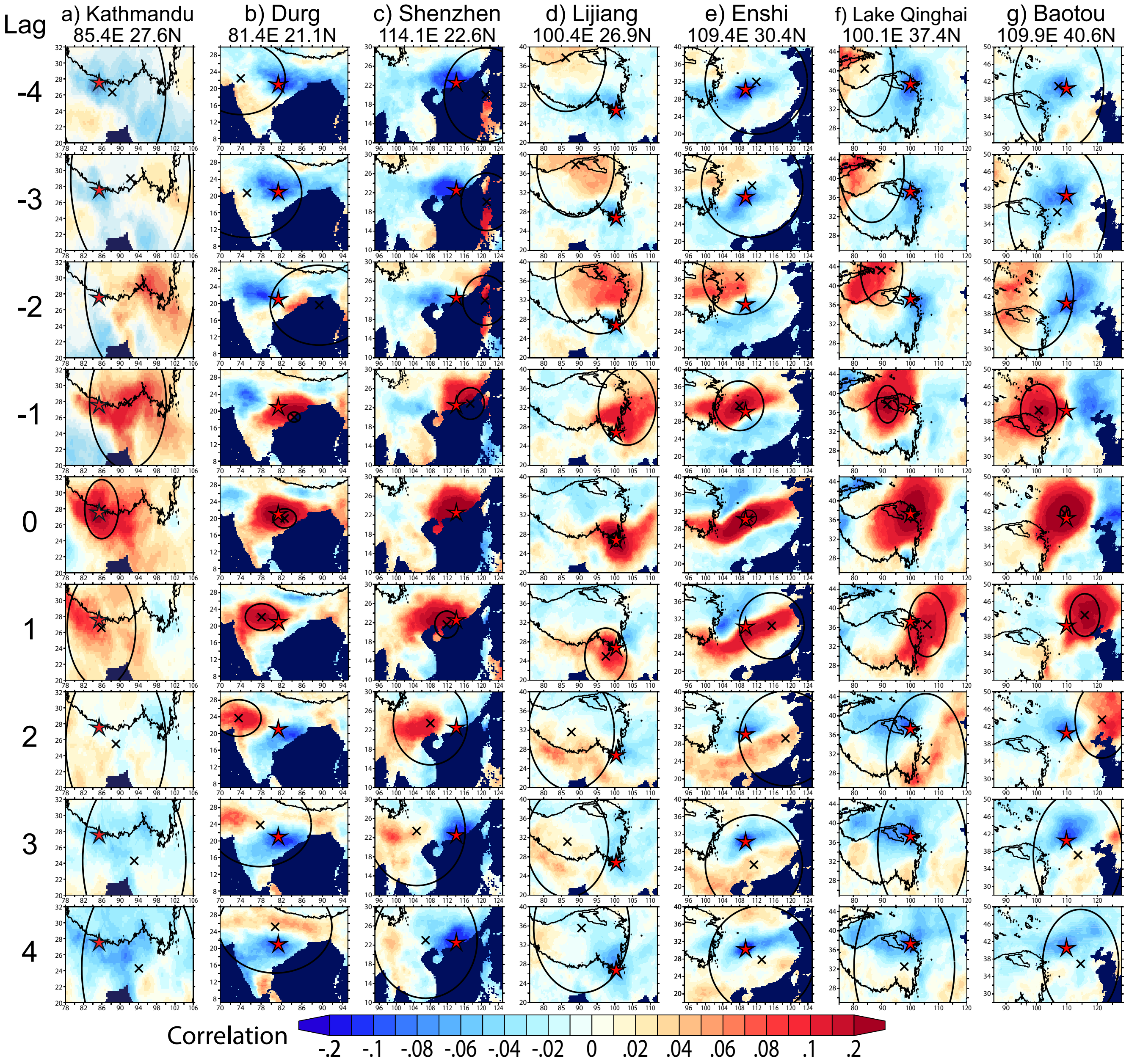

Figure 2.9: July-August K_i^λ for reference point (x_i, y_i) (red star) and $\lambda = -5$ to 5, where K_i^λ is the 57-year mean of anomalous correlation C_i^λ of local rainfall $P''(x_i, y_i)$ with normalized anomaly rainfall P'' at all other points, with an imposed lag or lead of λ days (see main text for formula). Variance circles for a given λ are drawn to include at least 50% of yearly maxima of anomalous correlation C_i^λ from all 57 years, with X marking their center.

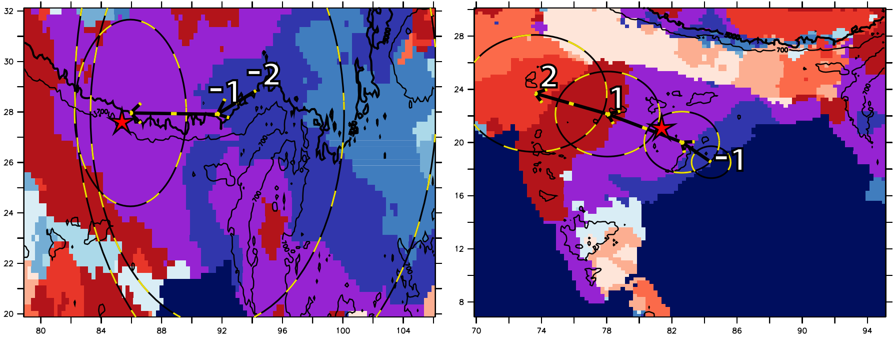

a) Kathmandu 85.4E 27.6N λ = -2 to 0

b) Durg 81.4E 21.1N λ = -1 to 2

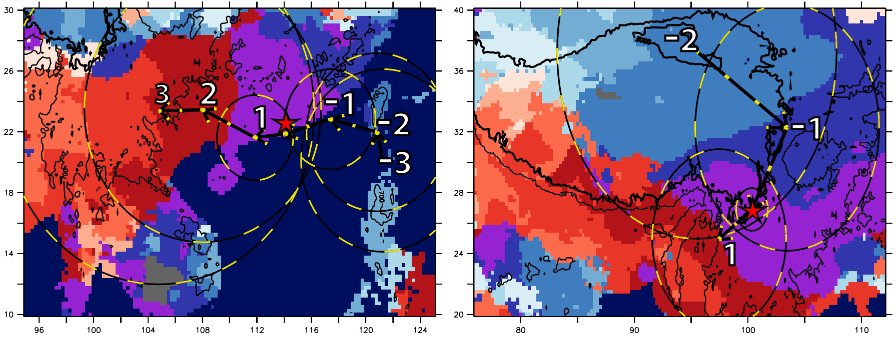

c) Shenzhen 114.1E 22.6N λ = -3 to 3

d) Lijiang 100.4E 26.9N λ = -2 to 1

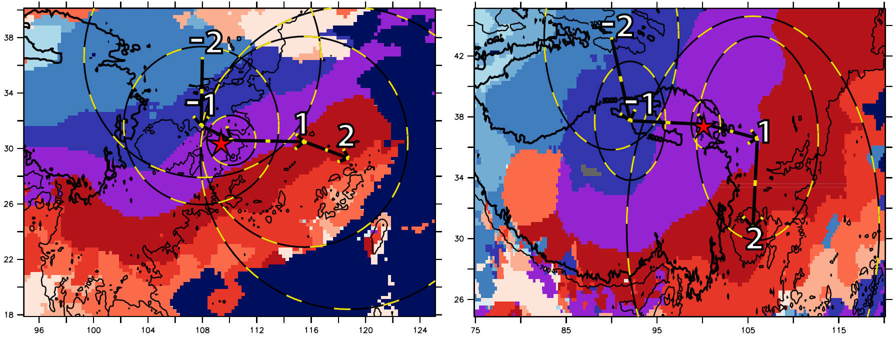

e) Enshi 109.4E 30.4N λ = -2 to 2

f) Lake Qinghai 100.1E 37.4N λ = -2 to 2

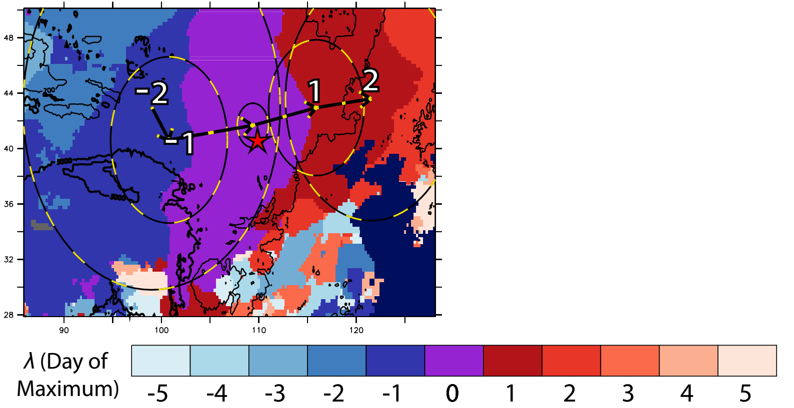

g) Baotou 109.9E 40.6N λ = -2 to 2

Figure 2.10: July-August plot of the lag λ for which, given listed reference point (x_i, y_i) (red star), the 57-year mean anomalous correlation of rainfall $K_i^{\lambda}(x, y)$ is maximized. Variance circles from Figure 9 (black with yellow highlights) are superimposed for range of λ listed above each figure, with connecting arrows showing propagation (also black with yellow highlights).

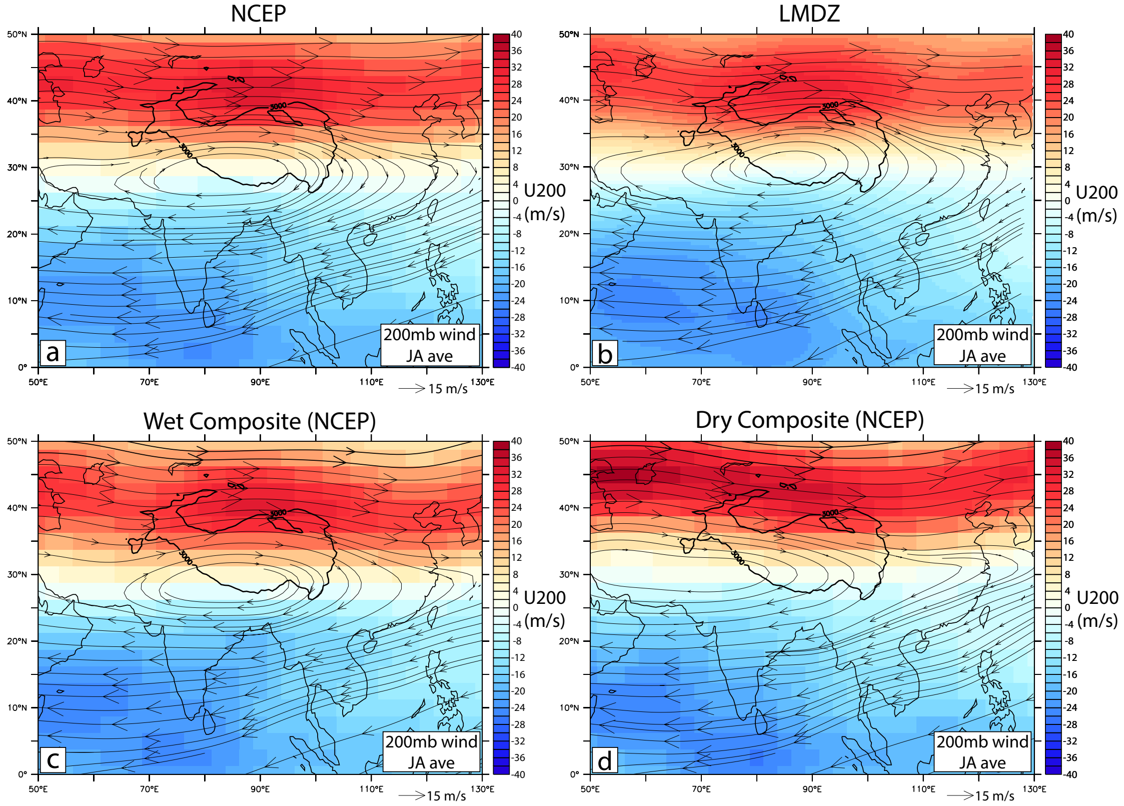

Figure 2.11: July-August streamlines of mean 200 mb level winds from NCEP reanalysis (1948-2014) (a) and LMDZ 200 mb winds for the year 2006 (b). Figures c and d are NCEP reanalysis 200 mb-level wind for composites of "wet" years (c) and "dry" years (d). The "wet" composite includes the five years with the most positive value of All-Asia JA EOF1, while the "dry" composite is the equivalent with the five most negative years.

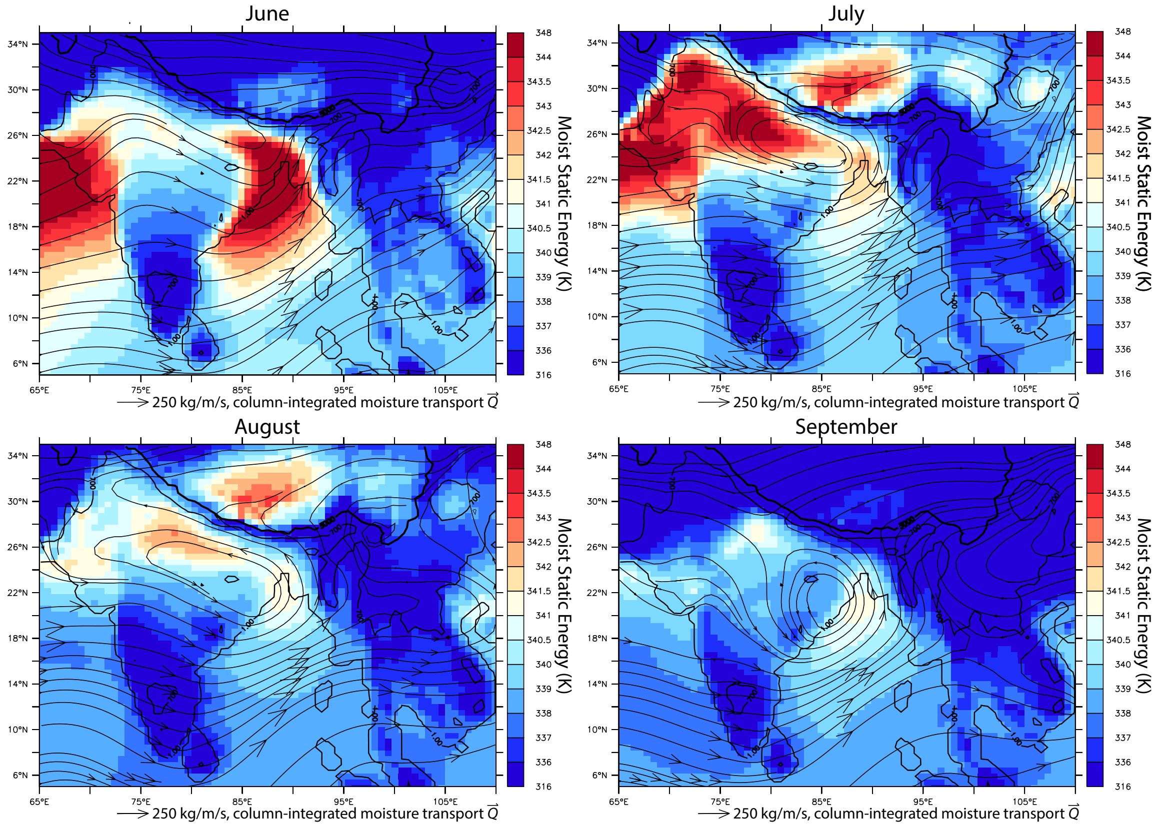

Figure 2.12: LMDZ values of near-surface moist static energy h_b (shading) and column-integrated moisture transport $\vec{Q}$ (streamlines, magnitude shown by size of arrowheads) for each month from June to September 2006 over the region 65°E-110°E and 5°N-35°N. Moist static energy is given by the formula $h_b = c_pT + L_vq + gz$, with specific heat of dry air c_p and latent heat of condensation of water L_v, as described in main text. Units of moist static energy are Kelvin, obtained by dividing h_b by c_p as practiced in Boos and Hurley, 2013. Column-integrated moisture transport is given by $\vec{Q} = \frac{1}{g}\int q\vec{u}\ \mathrm{d}p$. Note unusual color scale of moist static energy used to emphasize changes over continental India.

Chapter 3

The Rainband Detection Algorithm (RDA): A climatology of frontal rainfall in China

3.1 Abstract

A novel 57-year (1951-2007) daily catalog of frontal rainbands over China is compiled from APHRODITE rain gauge data via a recursive convergent image processing algorithm, the Rainband Detection Algorithm (RDA). We produce an unprecedented climatology of Meiyu front progression in summer, and investigate the "South Flood-North Drought" pattern of late 20th-century rainfall change in China. We find that the South Flood-North Drought has resulted from changes in rainbands properties during particular rainfall stages. Two robust changes occurred during 1980-2007 relative to 1951-1979: 1) A decrease in the frequency of frontal rainbands during the Pre-Meiyu period (May), and 2) a southward shift in the latitude of Post-Meiyu rainbands (mid-July to September). In addition, a previously reported shifted in June-July rainfall between 1994-2007 and 1979-1993 resulted from a change in intensity of frontal rainfall events, even though their frequency remained constant. The RDA method reveals modifications in rainband behavior that are not captured by other simpler metrics of China rainfall that we tested. By studying historical rainfall change, we begin to address the critical question of whether the South Flood-North Drought will persist under 21st-century global warming.

3.2 Introduction

Eastern China receives about 60% of its precipitation from May to August via the East Asian summer monsoon. The period of peak rainfall lasting from early June to mid-July is called "Meiyu season" (lit. "plum rains," referring to the spectacular growth of plum blossoms in central China with the onset of heavy rains). During this time, heavy rainfall occurs in zonal bands resulting from frontal synoptic conditions (the "Meiyu front"). The rainfall climatology of Japan and Korea also features similar phenomena, known as Baiu and Changma respectively, that deliver key fractions of total yearly rainfall. A growing volume of evidence suggests a shift in rainfall over China beginning in the late 1970s, featuring a "South Flood-North Drought" pattern shown in Figure 3.1 (Hu, 1997; Gong and Ho, 2002; Nigam et al., 2013). A permanent change would have major humanitarian impacts on densely-populated eastern China, where a sizable fraction of the population depends on agriculture for subsistence. Northern China already suffers from substantial depletion of freshwater resources along with increasing demand (Currell et al., 2012; Gleeson et al., 2012). The Chinese government has embarked on a project to reroute water from the Yangtze River to northern China, the South-North Water Transfer Project (*nanshui beidiao gongcheng*), which is expected to become the most expensive hydraulic engineering project ever undertaken and will entail massive human and environmental impact (Magee, 2011). Under such circumstances, it is vital to understand whether this pattern will strengthen under global warming, or represents only a temporary deviation from the mean.

The climatology of the East Asian monsoon is unique when compared to other monsoon circulations (Ding and Chan, 2005). Whereas understanding of tropical monsoons has progressed greatly via theoretical studies (Plumb and Hou, 1992; Privé and Plumb, 2007a; Bordoni and Schneider, 2008), the dynamics that favor the existence of frontal convection over East Asia in summer remain a point of debate, centering around the interplay of the tropospheric jet and Tibetan Plateau (Molnar et al., 2010; Sampe and Xie, 2010; Chen and Bordoni, 2014). Therefore, no simple conceptual template exists for interpreting the South Flood-North Drought. However, it is known that the migration of the Meiyu front entails a series of large-scale circulation changes (Chen, 2004), and furthermore that anomalies in Meiyu front latitude produce corresponding rainfall anomalies (Kosaka et al., 2011). Therefore, the South Flood-North Drought should be describable in terms of changes in the mean properties of Meiyu rainbands, such as a shift in latitude, a change in intensity, or an earlier or delayed northward migration. In turn, such a characterization may elucidate the dynamics responsible for the change.

We have developed a recursive fitting algorithm, the Rainband Detection Algorithm (RDA), that locates frontal rainbands in a daily precipitation map and quantifies their attributes. Using the APHRODITE rain gauge product, we have created a 57-year (1951-2007) daily database of rainband attributes in China. Previous studies have investigated the statistics of the Meiyu front on decadal and even centennial timescales (Chen, 2004; Ge et al., 2008; Xu et al., 2009), but to our knowledge no previous author has compiled a multi-decadal daily catalog of events. We use this catalog to find the late 20th-century changes in rainband statistics that have caused the South Flood-North Drought. Furthermore, since rainbands are produced by frontal atmospheric conditions, late 20th-century changes in rainband attributes may reflect corresponding changes in East Asian monsoon dynamics, and ultimately be influenced by 20th-century warming. We propose an altered progression of the tropospheric jet as proximal cause in the conclusion, and elaborate on this theory in Chapter 4.

3.3 APHRODITE

The APHRO_MA_V1101 product from APHRODITE (Asian Precipitation - Highly-Resolved Observational Data Integration Towards Evaluation of the Water Resources) includes 57 years (1951-2007) of daily rainfall (PRECIP product) on a .25° × .25° grid over 60°-150°E and 15°S-55°N (Yatagai et al., 2012). Values are assimilated from weather station observations and therefore available over land only. We focus on the subregion inside of 100°E-123°E and 20°N-40°N, where Meiyu rainbands occur. Stations in this region are spaced at 100-200 km intervals (shown by RSTN product), such that rainbands are clearly resolved. APHRODITE's resolution cannot capture some features visible in TRMM satellite data Xu et al. (2009), but its length allows for the study of decadal change. Since almost all precipitation in this region falls as rain, we use the words "rainfall" and "precipitation" interchangeably in the rest of this work.

3.4 Rainband Detection Algorithm (RDA)

Overview

For each day from 1 January 1951 to 31 December 2007 (20,819 days total), RDA determines whether a rainband exists inside the window of 105-123°E and 20-40°N, a region hereafter referred to as "East China." A rainband is defined as a continuous chain of rainfall maxima exceeding 10 mm day^{-1} spanning at least 5° of longitude. If a rainband exists, its properties are calculated including latitude, intensity, tilt, length and width, as well as a "quality score" Q, defined as the fraction of daily total East China rainfall falling within the band. Fits with poor Q are discarded. We also test for the existence of two rainbands on a single day, an arrangement commonly found in August and September. In such a case, the first and second fitted rainbands are referred to as "primary" and "secondary" rainbands respectively. A description of algorithm functionality in greater detail follows.

We cannot distinguish between the mechanisms that supply rainfall. Any storm that propagates zonally over the course of a day will be interpreted as a rainband, regardless even of whether it propagates westward or eastward. However, from observation, storms reaching East China during the rainiest months of the East Asian summer monsoon are predominantly westerly (Day et al., 2015). Therefore, we expect that RDA detects similar types of rainfall events from one summer to the next, allowing for meaningful analysis of decadal changes.

Recursive Convergent Image Processing

1. Given a daily map of East China rainfall (105-123°E, 20-40°N) at .25° × .25° resolution, the maximum rainfall intensity int_{max} and its latitude lat_{max} are recorded at each longitude. If there exists a continuous chain of maxima spanning 5° of longitude (20

points in a row) where int_{max} exceeds 10 mm day^{-1}, we proceed to step 2 and attempt a rainband fit (Figure 3.2a). Otherwise, there is no rainband and no fit is attempted for that day (Figure 3.2b).

2. A weighted least-squares linear regression of lat_{max} using int_{max} as weighting approximates the position of the rainband with a straight line (a reasonable assumption from observation). To encourage convergence, the weight of outlying maxima is set to zero. An outlier is defined as any maximum where lat_{max} is over 5° of latitude away from $\langle lat_{max}\rangle$, the centroid of lat_{max} weighted by int_{max}[1], calculated as

$$\langle lat_{max}\rangle = \frac{\sum_{long} lat_{max} * int_{max}}{\sum_{long} \max}$$

3. A recursive algorithm converges from this initial fit to a best estimate of rainband position. In each iteration, we find a new set of maxima within k degrees of the previous best fit line, and again perform a weighted linear fit of the maxima (Figure 3.3a). k is progressively decreased with each iteration from 5° to 2° by .25° increments, and then from 2° to .25° by .25° increments repeating each width k twice in a row (Figures 3.3b-c). The fit obtained in the final iteration is taken as our best estimate (Figure 3.3d).

4. We define the "quality score" Q as the fraction of daily total East China rainfall (the sum of all rainfall inside of 105-123°E and 20-40°N) that falls within 2.5° degrees of the best estimate line (Figure 3.4b). Other rainband properties are calculated as follows:

   a) *Latitude*: The latitude of the best fit line at 115°E.
   b) *Intensity*: Mean rainfall of all "rainband points" (points along the best fit line where daily rainfall exceeds 5 mm day^{-1}).
   c) *Length*: Total number of rainband points (units of degrees longitude)
   d) *Width*: Mean distance between half-maxima ($int_{max}/2$) on either side of each rainband point (units of degrees latitude).

---

[1] In rare cases with two rainbands of roughly equal strength that are well-separated in latitude, the centroid of precipitation may lie midway between the bands such that all maxima will be thrown out as outliers. To avoid this scenario, we verify after removing outliers that

$$\sum_{long} weights > 200 \text{ mm day}^{-1}$$

When this condition is failed, which can only occur when too many of our maxima have been discarded, we return to step 1 and find maxima inside a subwindow with latitude range of 20°N-$\langle lat_{max}\rangle$ or $\langle lat_{max}\rangle$-40°N, depending on which half of our domain has a longer chain of maxima exceeding 10 mm day^{-1}. The remaining steps of our algorithm are applied as usual. The search for a secondary rainband and calculation of quality scores are performed over the whole East China window (20°N-40°N).

5. After finding a primary rainband, we check for the existence of a secondary rainband by removing all *banded rainfall* associated with the primary band from the daily rainfall map. *Banded rainfall* is defined as all rainfall falling within 4° of a rainband axis and any other adjacent points where rainfall exceeds 10 mm day^{-1} (see Figure 3.5a for an example). After removing primary rainband rainfall, we reapply the continuous maximum criterion from step 1 (Figure 3.5b). If passed, steps 2-4 are repeated to find a best estimate for the position of the secondary rainband, and its attributes calculated.

6. If a secondary rainband is found, two additional *conditional* quality scores Q_1 and Q_2 are calculated. Q_1 is the fraction of total daily East China rainfall that fell within 2.5° degrees of the primary rainband *after removing all rainfall associated with the secondary rainband* (effectively the Q score if the secondary rainband didn't exist). Likewise, Q_2 is the Q score of the second rainband *after removing all rainfall from the primary rainband.* An example is shown in Figure 3.4d.

Quality Control

After running the algorithm for all 20,819 days from 1 January 1951 to 31 December 2007, we obtained 11,228 days with at least one rainband and 1,116 days with two rainbands. Subsequently, we apply a quality control (QC) algorithm to eliminate days with poor fit, based on the quality scores Q, Q_1 and Q_2 as well as the "Taiwan fraction" TW, defined as the percentage of daily total East China rainfall falling over the island of Taiwan (roughly 120-122°E and 22-26°N). Rainband fits are deemed successful if they satisfy the following two criteria:

1. $TW < 20\%$. If $TW > 20\%$, the day's fit is thrown out (238 cases total, 2.1% of total fits). Such days are dominated by tropical storms reaching Taiwan and do not exhibit a strong rainband (example shown in Figure 3.4a).

2. The quality scores of the fit must meet either of the two following benchmarks:

   a) If $Q > .6$, the fit is deemed successful (7,522 days, 67.0% of total fits; Figure 3.4b). If Q_2 is also greater than .6, the day will be classified as a double rainband day (Type I double rainband; 232 cases). 3.1% of days where $Q > .6$ also achieve $Q_2 > .6$.

   b) If $Q < .6$, the fit is discarded unless two rainbands are detected and both $Q_1 > .6$ **and** $Q_2 > .6$ (where again Q_1 and Q_2 are *conditional* quality scores as defined above). In such cases, the presence of multiple rainbands of similar intensity initially obscures the goodness of fit (Figure 3.4d). Such days are also classified as double rainband days (Type II double rainband; 466 cases).

If neither criterion 2a nor 2b is satisfied, the fit is thrown out (Figure 3.4c).

The use of conditional quality scores Q_1 and Q_2 adds 466 double rainband fits (6.2% of all successful fits) that would otherwise have been missed due to $Q < .6$. 33.2% of double rainband days are Type I ($Q > .6$) and 66.8% Type II ($Q < .6$) as defined above. Double rainbands are more common during certain months, particularly July-September. Tables 3.1-3.3 contain detailed results of the application of RDA to years 1951-2007 in APHRODITE. The entire catalog is publicly available on the author's website.

Rainfall Types

RDA allows us to classify all rainfall on each day as either *banded* (falls within a rainband) or *local*. *Banded* rainfall consists of all rainfall falling within 4° of a rainband axis and any other adjacent points where rainfall exceeds 10 mm day^{-1}, the same definition as in step 5 of the recursive algorithm above. An example is shown in Figure 3.5a. Rainfall on each of the 20,819 available days was partitioned into its banded and local components. This allows us to determine what fraction of rainfall at each point in East China is supplied via banded rainfall (Figure 3.7). We also test for the significance of decadal changes in banded and local rainfall separately (Figure 3.10). These results are discussed below. Videos of the climatological progression of banded and local rainfall are available at the author's website and on request, as well as daily maps of banded and local rainfall for the years 1951-2007.

3.5 Methods

Alternative Metrics of China Rainfall

Since the RDA method is complex, we must justify its use by proving that it supplies information about China rainfall beyond what simpler metrics can provide. We define a suite of potential daily rainfall metrics as follows:

- M_1 - Latitude of maximum rainfall;
- M_2 - Intensity-weighted centroid of daily rainfall latitude;
- M_3 - Intensity of maximum rainfall over China (100-123°E and 20-40°N);
- M_4 - Area-averaged intensity of China rainfall;
- M_5 - Area-averaged intensity of North China rainfall (107.5-125°E and 37-42°N);
- M_6 - Area-averaged intensity of South China rainfall (107.5-122.5°E and 27-33°N);
- M_7 - % of days where M_5 exceeds 1 mm day^{-1} (*frequency* of North China rainfall);
- M_8 - % of days where M_6 exceeds 1 mm day^{-1} (*frequency* of South China rainfall).

The definitions of the North China and South China regions are the same as in Yu et al. (2010). Each metric is subjected to the same tests of significance applied to changes in rainband behavior between time periods. The climatologies of $M_1 - M_8$ are shown in Figure 3.9a-d, and mean values during different seasons listed in Tables 3.9-3.11. The significance of changes in each metric between 1951-1979 and 1980-2007 is displayed in Table 3.12. Section 3.6 discusses results.

Temporal Autocorrelation

Fronts and rainbands tend to persist for several days. Therefore, rainfall amounts and front attributes on successive days are not fully independent observations, which reduces the effective number of degrees of freedom of these time series. This temporal autocorrelation must be accounted for in calculations of statistical significance such as estimating the p-value of a change in rainband frequency between two time periods. In this particular case, we use the analytic formula for a Bernoulli process (applicable for any time series where observations are binary) with effective number of degrees of freedom $n = \frac{N}{\tau}$ for number of days N and decorrelation time τ given by

$$\tau = 1 + 2\sum_{k=1}^{m} \rho(k)$$

where $\rho(k)$ is the autocorrelation function of rainband existence with lag k (Von Storch and Zwiers, 1999). We calculate τ using a maximum lag of $m = 10$ days. The yearly mean decorrelation timescale of rainband frequency is found to be $\tau = 1.81$ after removing the seasonal cycle. This value is used to calculate significance of changes in Figure 3b. The standard deviation and p-values of rainband frequency changes in Tables 3.5 and 3.7 use seasonal values of τ calculated in 3.4. Similarly, Table 3.11 shows the τ of alternative metrics of China rainfall, which is then used to calculate the significance of decadal changes in Table 3.12. τ is also used to select block length for moving blocks bootstrap tests, as described below.

Significance of Changes: Bootstrapping Algorithms

Observations of rainband latitude and intensity during a given time period obey unknown distributions. Therefore, we require non-parametric tests to estimate the standard deviation of their mean and the significance of changes in mean. We employ bootstrapping with and without replacement (the latter also known as a permutation test), well-established techniques that estimate quantities of interest by constructing synthetic distributions with random sampling of original data (Good, 2005). We use bootstrapping with replacement to calculate the standard deviation of means (Tables 3.4, 3.6 and 3.8). We focus on changes in front attributes between 1951-1979 and 1980-2007 (Tables 3.5 and 3.6), and also repeat our methodology for 1979-1993 versus 1994-2007 (Tables 3.7 and 3.8). p-values listed are from permutation testing with 10,000 iterations; the results of bootstrapping with and without replacement are very similar.

The bootstrap must be adapted for time series featuring temporal autocorrelation. In such time series, a single anomalous weather event will persist over several days, and a bootstrap method will tend to exaggerate the significance of differences between the two original distributions. To avoid this scenario, we use a *moving blocks bootstrap* test, described for instance in Singh et al. (2014). This technique is identical to bootstrapping with replacement except that samples are drawn in continuous blocks of length n that preserve the time structure of the original data set. Block length is chosen based on decorrelation time scale τ. The autocorrelation of daily rainfall in China is $\tau = \sim 3$ days, and therefore the significance estimates in Figure 3.6a use a moving blocks bootstrap with block length of 3 days and 1000 iterations. The calculation of significance of change in alternative China rainfall statistics $M_1 - M_6$ (Table 3.12) uses the τ of each statistic in each season (Table 3.11) rounded to the nearest integer as block length. In general, a choice of block lengths between 2 and 5 days leads to similar results. Our MATLAB code for the permutation test and the moving blocks bootstrap is included in the appendix.

The moving blocks bootstrap cannot be used for time series with gaps. Therefore, we use a permutation test to estimate the significance of changes in mean latitude and intensity of rainbands between time periods (Tables 3.6 and 3.8). These latter results are verified with Anderson-Darling and Kolmogorov-Smirnov tests, two methods which estimate the significance of shifts in distribution between two sample. These tests are described below.

Significance of Changes in Distribution

In addition to gauging the significance of changes in mean, we can also test the probability that two samples were drawn from the same distribution. The Kolmogorov-Smirnov and Anderson-Darling tests each define a test statistic based on the largest difference between the observed probability distribution of two samples. Similar to a t-test, the value of this test statistic can be translated into a p-value. We first define the *empirical distribution function* $F_1(x)$ and $F_2(x)$ of each sample. All n observations in each sample are ordered as $\{X_1 < ... < X_n\}$, after which $F(x)$ is calculated as follows:

$$F(x) = \frac{1}{n} \sum_{i=1}^{n} I_{[-\infty,x]}(X_i) \tag{3.1}$$

$$I_{[-\infty,x]} = \begin{cases} 1 & \text{if } X_i \leq x \\ 0 & \text{otherwise} \end{cases} \tag{3.2}$$

The K-S test statistic D is then defined as the maximal distance between the two empirical distribution functions:

$$D = \max_{all\ x} |F_1(x) - F_2(x)| \tag{3.3}$$

D can then be inverted to derive a p-value. The Anderson-Darling (A-D) test statistic A^2 resembles D, but is formulated to be more sensitive to the tails of the distribution:

$$A^2 = -n - S\,, \text{where} \tag{3.4}$$

$$S = \sum_{i=1}^{n} \frac{2i-1}{n} \left[\ln(F(X_i)) + \ln\left(1 - F(X_{n+1-i})\right)\right]. \tag{3.5}$$

A^2 can likewise be translated into a p-value. The K-S and A-D tests cannot be used if values are repeated within samples, because D and A^2 are then undefined. We solve this problem by using bootstrap versions of these tests. Bootstrap K-S and A-D tests were performed using the programming language R with 10,000 iterations. The significance of changes in the distribution of rainband latitude and intensity are presented in Tables 3.13 and 3.14. Both tests produce fairly similar results.

3.6 Results

Rainband Climatology

We compile our daily rainband catalog into a 57-year daily climatology (1951-2007). The yearly progression of precipitation over eastern China is shown in Figure 3.6a, longitudinally averaged over $100 - 123°$E with a 5-day running mean, similar to Figure 7 in Ding and Chan (2005). China receives a substantial fraction of its yearly precipitation outside of summer, unlike other monsoonal regions which tend to be very dry in winter (Wang and LinHo, 2002). Figure 3.6b shows a Hovmöller diagram of the probability of rainband occurrence at each latitude, including both primary and secondary rainbands. Some periods of heavy rainfall, in particular the August peak over southern China (over 10 mm day^{-1} around 20°N), do not correspond to a surge in rainband frequency. Figure 3.6c shows the probability of rainband occurrence and mean intensity on each day. Figure 3.6d shows mean rainband tilt and length, as well as the conditional probability of observing a secondary rainband given the presence of a primary rainband. Frontal rainbands over China can appear in any month, with their probability of occurrence and intensity maximizing in late June (80% probability of occurrence, mean intensity of 31 mm day^{-1}) and minimizing in January (10% probability occurrence, mean intensity of 12 mm day^{-1}).

Abrupt climatological shifts occur simultaneously in both rainfall and rainband climatology. We define 5 periods of distinct behavior as demarcated in Figure 3.6:

1. The Spring Rains (days 60-120, March 1-April 30), previously studied in Tian and Yasunari (1998), marked by frequent but relatively weak rainbands (47% occurrence, 20 mm day^{-1} mean);

2. Pre-Meiyu season (days 121-160, May 1-June 9), during which rainfall and front intensity steadily increase (56% occurrence, 25.5 mm day^{-1} mean);

3. Meiyu season (days 161-200, June 10-July 19) when a remarkable 7-degree northward shift in mean rainband latitude occurs over the course of several weeks, and rainband frequency and intensity peaks (66% occurrence, 28.3 mm day^{-1} mean);

4. Post-Meiyu season (days 201-273, July 20-September 30), when rainbands are less common than during the Spring Rains (42% occurrence) but double rainbands occur more frequently (28% chance of observing a secondary rainband if a primary rainband is observed);

5. The Fall Rains (days 274-320, October 1-November 16), when mean rainband latitude shifts back southward from its northern maximum of 30°N and rainband frequency decreases to just 27%.

The Pre-Meiyu, Meiyu and Post-Meiyu are equivalent to the three stages of Meiyu rainfall described in Ding and Chan (2005). The transition from Pre-Meiyu to Meiyu and from Meiyu to Post-Meiyu both entail striking, sudden changes in rainband behavior. The onset of the Meiyu is marked by a climatological jump in rainband frequency and intensity around day 160 (June 9) that persists for 20 days when rainbands are concentrated between 26° and 30°N. Yet by day 200 (July 19), this same region is less likely than any other latitude to feature a rainband, roughly an 80% local decline in frequency in the span of 3 weeks (Figure 3.6b). Rainbands are generally more probable and stronger during spring than in fall, and the intensification of rainband activity during the Meiyu and abrupt northward jump have no counterpart in the Fall Rains. The causes of this seasonal asymmetry merit further study.

These results can be compared with the frontal event catalog of Xu et al. (2009), which finds a similar date for the northward transition of the Meiyu front. The total number of rainband counts as well as the mean and standard deviation of rainband frequency, latitude and intensity during each time period are presented in Table 3.4. Figure 3.7 shows that frontal rainfall constitutes at least 40% of yearly total for all of mainland China east of 105°E between 21°N and 37°N, over 60% for most of central China, and up to 74% in the vicinity of Jiangxi Province (28°N, 116°E). Thus, banded rainfall is an essential component of East China's yearly rainfall budget.

Rainband Changes

1980-2007 versus 1951-1979

The yearly mean change in rainfall rate between 1951-1979 and 1980-2007 over the region 100°-142°E and 20°-48°N is shown in Figure 3.1. The South Flood-North Drought refers in particular to a meridional dipole of decadal rainfall change over eastern China (110°-125°E and 22°-42°N), where most of China's population resides. Pronounced local shifts are also visible in Taiwan, South Korea and parts of Japan. This work focuses on eastern China. Annual changes in northern China between 35°-40°N are significant at a 95% confidence level, whereas changes in central and southern China are not. However, there are substantial changes in central and southern China rainfall during particular Meiyu stages, as shown in Figure 3.8a and discussed below.

We test whether the rainband catalog reflects the South Flood-North Drought by calculating changes in rainband frequency during 1980-2007 relative to 1951-1979 (shown as a Hovmöller diagram in Figure 3.8b). We also calculate the significance of changes in rainband attributes during each of the five Meiyu stages (Tables 3.5 and 3.6). During the Pre-Meiyu (days 121-160), the probability of observing a primary rainband has declined from 59.0% ± 2.0% to 53.0% ± 2.1% (p = 0.020; Table 3.5. Figure 3.8 shows matching decreases in front occurrence and rainfall over central China during this time period. The Pre-Meiyu decrease in rainfall was previously reported by Xin et al. (2006), who linked it to decadal change in the North Atlantic Oscillation (NAO), and also by Wang et al. (2009). We propose that diminished rainband occurrence has caused this decrease.

In addition, a southward shift in mean rainband latitude has occurred during the Post-Meiyu (days 201-273, or July 20-Sep 30). We focus on rainbands north of 27°N; rainbands occurring south of this latitude are produced by the westward-propagating remnants of tropical storms, and therefore dynamically unrelated to other storminess during Meiyu season (Day et al., 2015). Considering both primary and secondary rainbands north of 27°N, mean latitude during 1951-1979 was 33.6°N ± .3° versus 32.9°N ± .3° during 1980-2007 ($p = .0003$; Table 3.6). This shift remains significant if we do not restrict by front latitude ($p = .0048$). A Post-Meiyu rainfall increase in central China and decrease in northern China has also occurred, producing a South Flood-North Drought pattern (Figure 3.8c). As a result, yearly rainfall has increased in central China even though Pre-Meiyu rainfall changes in that region are actually negative (Figure 3.8a). Unlike Yu et al. (2010), our catalog does not exhibit a 20th-century decrease in the intensity of Yangtze River region frontal rainbands during July-August. A significant southward shift in rainband latitude is also found for the whole year ($p = .0032$, Table 3.6), but this signal is dominated by the Post-Meiyu shift.

1979-1993 versus 1994-2007

We test this methodology also with the set of years 1979-1993 versus 1994-2007, when past authors have reported a shift in South China rainfall (Kwon et al., 2007; Wu et al., 2010; Yim et al., 2013). The most distinctive change between these two sets of years occurred during Meiyu season, during which rainband latitude shifted southward from 30.0°N ± .4° to 28.9°N ± .4° ($p = .0002$) and the *intensity* of rainbands also jumped from 27.3 ± 1.1 mm day^{-1} to 29.8 ± 1.1 mm day^{-1} ($p = .9994$), leading to increased rainfall over central and southern China. Zou and Ren (2015) also found that China experienced a more intense Meiyu during the 1990s, as well as generally more severe rainfall events. Unlike the comparison between 1951-1979 and 1980-2007, rainband *frequency* remained unchanged. We infer that changes in frequency versus changes in intensity may signal the existence of two different types of external forcing, an idea further explored in the conclusion.

Significance of Changes in Distribution of Latitude and Intensity

As discussed in Section 3.5, a permutation test of changes in rainband latitude and intensity may exaggerate their significance. We use two independent techniques, a bootstrap Kolmogorov-Smirnov and bootstrap Anderson-Darling test, to verify the results in Table 3.4. The results of comparing the years 1980-2007 to 1951-1979 is presented in Table 3.13. Neither test captures the Pre-Meiyu decline in rainband frequency after 1979 since rainband latitude and intensity distributions remain similar. On the other hand, the Post-Meiyu southward shift in rainband latitude is found to be highly significant by both tests ($p < .001$). As before, no significant changes in rainband intensity are found between 1951-1979 and 1980-2007. This suggests that the estimates of significance from permutation testing are trustworthy.

Also, a substantial southward shift in latitude and decrease in intensity of rainbands is found during Meiyu season between 1979-1993 and 1994-2007 ($p < .001$ for both changes; Table 3.14). This further confirms that rainfall changes observed between 1979-1993 and 1994-2007 are fundamentally different from the South Flood-North Drought pattern of changes between 1951-1979 and 1980-2007.

Decadal Changes in Alternative Metrics $M_1 - M_8$

We compare the results above with the magnitude of changes in a suite of simple metrics for China rainfall $M_1 - M_8$, as defined in Section 3.5. We focus on differences in $M_1 - M_8$ between 1980-2007 and 1951-1979 (Tables 3.9-3.12). No alternative metric supplies a complete picture of late-20$^{\text{th}}$-century China rainfall change. From 1951-1979 to 1980-2007, area-averaged North China rainfall (M_5) during the Post-Meiyu season declined from 3.20 mm day^{-1} to 2.70 mm day^{-1}. This change is significant at a 99% level ($p = .0004$), and induced a yearly decrease in North China rainfall from 1.31 mm day^{-1} to 1.20 mm day^{-1} ($p = .0068$). However, the change in M_5 fails to capture the southward shift of rainband latitude during the Post-Meiyu that is ultimately responsible for the drought in North China, as seen in Figure 3.8a. Similarly, the intensity-weighted centroid of precipitation latitude (M_2) shifted southward during the Pre-Meiyu by $.3°$ ($p = .017$) from 1951-1979 to 1980-2007, but RDA suggests that the most notable change in rainfall between these time periods is the *frequency of occurrence of rainbands* that supply the rainfall (Table 3.5). No other metric shows any notable change during the Pre-Meiyu season.

In summary, the use of RDA captures key features of the South Flood-North Drought that are not revealed by analyzing simpler metrics.

Change in Rainfall Types

Using our method for partitioning daily rainfall into its banded and local components, we can test whether one of these components accounts for the majority of decadal change. In Figure 3.10, we compare banded and local rainfall changes between the periods 1980-2007 and 1951-1979 over the whole year, and also during the Pre-Meiyu and Post-Meiyu seasons during which we have already identified substantial change. The significant decrease in yearly rainfall in northern China (Figure 3.1) is overwhelmingly due to a regional decrease in banded rainfall (significant at a 99% level) without a corresponding decrease in local rainfall (Figure 3.10a). During the Pre-Meiyu season (Figure 3.10b), a marked decrease in banded rainfall over the Yangtze River Valley ($p < .005$) is partially offset by a general increase in local rainfall across all of China, especially in the vicinity of Hunan, Guizhou and Chongqing Provinces (108°-114°E, 26°-30°N). The Post-Meiyu dipole between northern and southern China is clearly visible in changes in banded rainfall, and indistinct in local rainfall changes (Figure 3.10c). In contrast, the sharp decrease in yearly rainfall in Taiwan is overwhelmingly due to changes in local rainfall. Banded rainfall only makes up 20-30% of total rainfall on the island (Figure 3.1).

In conclusion, **the North Flood-South Drought has resulted primarily from changes in banded rainfall**. In turn, these changes in banded rainfall are zonally symmetric and coherent across thousands of kilometers, which suggests that they are caused by changes in the large-scale dynamics of the East Asian summer monsoon. We explore possible causes in the conclusion and Chapter 4.

3.7 Conclusion

The goal of this work has been to present a clear summary of late-20$^{\text{th}}$-century rainfall change in China as characterized by changes in frontal rainfall, a core element of the East Asian summer monsoon that constitutes 56% of yearly rainfall to the region. We used the Rainband Detection Algorithm (RDA), a recursive image processing algorithm, to compile a 57-year catalog of daily rainband occurrence over China and the properties of each event, such as latitude, intensity, tilt, width and length, all of which we have made available to other researchers. The progression of the East Asian summer monsoon in China is displayed in unprecedented fashion as a sequence of 5 stages, each with preferred position, frequency and strength of frontal rainfall. With approximate duration listed, these are: 1) the Spring Rains (March 1-April 30); 2) the Pre-Meiyu (May 1-June 9); 3) the Meiyu (June 10-July 19); 4) the Post-Meiyu (July 20-September 30) and 5) the Fall Rains (October 1-November 16). The climatological transitions from one period to the next are abrupt rather than smooth.

We are able to ascribe previously reported decadal rainfall change (the South Flood-North Drought) to modified rainband properties during particular rainfall stages. Two statistically significant occurred between the years 1951-1979 and 1980-2007:

1. A decrease in rainband frequency during the Pre-Meiyu ($p = .020$);

2. A southward shift in mean rainband latitude during the Post-Meiyu ($p = .0003$, permutation test; $p = .0001$, Anderson-Darling test).

The first change led to a decrease in central China rainfall in May, while the second has been the principal contributor to the South Flood-North Drought trend in total yearly rainfall (Figure 3.1). Furthermore, we find that rainfall changes during the Pre-Meiyu and Post-Meiyu in China are primarily due to changes in frontal rainfall, as opposed to a change in the contribution from local storms (Figure 3.10). These robust decadal changes in rainbands suggest the influence of large-scale climate change, which may have altered the synoptic conditions in the East Asian monsoon that produce frontal rainfall.

It is essential to understand whether the South Flood-North Drought will persist under 21st-century warming, or manifests an ephemeral decadal change. However, the CMIP5 (Climate Model Intercomparison Project) model suite contained in the Intergovernmental Panel on Climate Change's Fifth Assessment Report (IPCC AR5) does not even agree on the sign of future summer rainfall changes in East Asia (Christensen et al., 2011). Some studies attribute the South Flood-North Drought to natural variability (Zhang et al., 1999; Xin et al., 2006; Lei et al., 2014), but Zhou et al. (2009) claimed that the South Flood-North Drought was distinct from other patterns of 20th-century variability. Since regional climate projection in Asia poses such a challenge, the most hopeful approach may be to link the South Flood-North Drought with other large-scale climate changes that can be more reliably modeled and projected into the future. Zhao et al. (2010) previously suggested that the South Flood-North Drought was associated with the late 20th-century rise in global mean surface temperature. In Chapter 4, we propose that 20th-century global warming has influenced frontal rainfall in China by changing the seasonal cycle of the East Asian jet. Many recent studies have studied the influence of global warming on the Hadley Cells and tropospheric jets (Frierson et al., 2007; Kang and Lu, 2012). A link between changes in the East Asian jet and rainfall could reveal the future of the South Flood-North Drought.

We also investigated a change in China rainfall between 1979-1993 and 1994-2007 reported by other authors. We find a highly significant uptick in the *intensity* of rainbands during Meiyu season ($p = .0006$) as well as a southward shift in their mean latitude ($p = .0002$). The resulting mid-summer rainfall increase over the Yangtze River basin has increased the risk of flooding (Gemmer et al., 2008). We suggest that a different mechanism explains this surge in frontal rainfall severity than explains the 1951-1979/1980-2007 changes, which are characterized by frequency changes. A potential culprit are the aerosols produced during the industrialization and urbanization of East China beginning in 1979 with Deng Xiaoping's Revolutionary Reform and Opening (*gaige kaifang*). Recent research highlights the potentially substantial impact of aerosols on atmospheric temperature and cloud properties across Asia (Menon et al., 2002; Fan et al., 2012; Streets et al., 2013). We suggest that the intensification of frontal storms during Meiyu season from 1994 to 2007 is linked to the rise in aerosols, and that they may be further impacted by the anticipated decrease of anthropogenic aerosols in the 21st century (Westervelt et al., 2015).

Our study also shows that the whole of Taiwan has experienced a deficit in rainfall during the end of the twentieth century. In particular, the south and eastern coast on the east of the Central Mountain Range saw the largest decrease during 1980-2007 versus 1951-1979 in all of East Asia according to APHRODITE (almost 2 mm day^{-1}). According to RDA, Taiwan receives relatively little banded rainfall (less than 40%; Figure 3.7), and the yearly aggregate depends substantially on typhoons and the locally favorable rainfall conditions in their wake (Chen and Chen, 2011). No consensus exists on the overall impact of global warming on tropical cyclone rainfall (Wehner et al., 2015). The suggestion has been made that tropical cyclone tracks in the vicinity of Taiwan have shifted due to global warming (Wang et al., 2011), but the shifts in question are only on the order of several hundred kilometers and may reflect natural variability instead (Chan, 2006). An upsurge in Taiwanese rainfall from tropical cyclones occurred at the beginning of the 21st century (Tu et al., 2009), but further analysis suggested that it was unrelated to global warming (Chang et al., 2013). Thus, the 20th-century decrease in Taiwanese rainfall remains to be explained. This example highlights the potential versatility of our rainband catalog in isolating different aspects of East Asian rainfall change.

3.8 Acknowledgments

APHRODITE precipitation data is publicly available at `http://www.chikyu.ac.jp/precip/index.html`. Ferret, a NOAA product, was used for some data analysis and preliminary plot generation and is freely available at `http://ferret.pmel.noaa.gov/Ferret/`. The rainband detection algorithm and the majority of data analysis code were written in MATLAB. A full database of rainband statistics from 1 January 1951 to 31 December 2007 and associated MATLAB and Ferret codes used to produce results are available at the author's website: `http://www.atmos.berkeley.edu/~jessed/data.html`, and key figures are reproduced at `http://www.atmos.berkeley.edu/~jessed/myfigures.html`. This work was supported by NSF grants EAR-0909195 and EAR-1211925, which allowed the presentation of preliminary results in conference settings and the feedback of our peers. We also acknowledge NSFC (National Natural Science Foundation of China) grant #40921120406 for enabling our collaboration with Professor Yanjun Cai of IEECAS in Xi'an, which led to the present work. Important contributions to the current work were made by Inez Fung, Jacob Edman, John Chiang and Weihan Liu. We thank Jinqiang Chen and an anonymous reviewer for valuable suggestions on a version of this chapter intended for publication.

3.9 Code

Below we attach the relevant code used to perform bootstrapping of Meiyu statistics without replacement (permutation test) and the moving blocks bootstrap for calculating significance of differences.

Permutation test of significance of changes

```
function [actualdiff,p,testmean,testdev] = myperm(s1,s2,niter)

%myperm.m, written by Jesse Day October 29th 2014. Uses a permutation test
%to determine the statistical significance of difference in means between
%two populations.

%s1 is sample 1, s2 is sample 2. ps refers to permuted sample

diffs=zeros(niter,1);
n1=length(s1);
n2=length(s2);
n=n1+n2; %total number of samples to rearrange
s=[s1 s2];

for i=1:niter

    order=randperm(n);
    ps1=s(order(1:n1));
    ps2=s(order(n1+1:n));
    diffs(i)=mean(ps2)-mean(ps1);

end

testmean=mean(diffs);
testdev=std(diffs);
actualdiff=mean(s2)-mean(s1);
ndiff=sum(actualdiff>diffs);
p=(ndiff+1)/(niter+1); %obtains an unbiased estimator

%histogram of means versus actual value
%histogram(diffs);
```

Moving blocks bootstrap for significance of changes

```
function [actualdiff,p,testmean,testdev,Zscore] = mybs_diff_blocks( ...
        s1,s2,niter,blklen)

%edited April 2nd 2015 to allow for selection of data in blocks.

%mybs_diff.m. written by Jesse Day October 29th 2014. A complementary
%technique to myperm.m, which uses a permutation test (no replacement) to
%determine whether a shift in mean between two populations is statistically
%significant or not.

n1=length(s1);
n2=length(s2);
s1_avs=zeros(niter,1);
s2_avs=zeros(niter,1);
diffs=zeros(niter,1);

for i=1:niter

    bs1=zeros(size(s1));
    bs2=zeros(size(s2));

    for j=1:blklen:n1

        jmax=j+blklen-1;

        if jmax>n1
            jmax=n1;
        end

        myblklen=jmax-j+1;
        sampmax=n1-myblklen+1;

        myr=mod(round(rand*sampmax),sampmax)+1;
        bs1(j:jmax)=s1(myr:myr+myblklen-1);

    end

    for j=1:blklen:n2

        jmax=j+blklen-1;
```

```
            if jmax>n2
                 jmax=n2;
            end

            myblklen=jmax-j+1;
            sampmax=n2-myblklen+1;

            myr=mod(round(rand*sampmax),sampmax)+1;
            bs2(j:jmax)=s2(myr:myr+myblklen-1);

      end

      s1_avs(i)=mean(bs1);
      s2_avs(i)=mean(bs2);
      diffs(i)=s2_avs(i)-s1_avs(i);
%          diffs(1:i)
%          pause

end

actualdiff=mean(s2)-mean(s1);
ndiff=sum(diffs>0);
p=(ndiff+1)/(niter+1); %obtains an unbiased estimator
testmean=mean(diffs);
testdev=std(diffs);
Zscore=testmean/testdev;

%extra verification module
histogram(diffs);
mean1=mean(s1_avs);
dev1=std(s1_avs);
mean2=mean(s2_avs);
dev2=std(s2_avs);
sampdev=(dev1^2/niter+dev2^2/niter)^(1/2);
trudev=sampdev*niter^(1/2);
pause
testdev;
pause
```

3.10 Tables and Figures

Table 3.1: Statistics on the functionality of the rainband detection algorithm. Number in parentheses indicates the percentage of days that fall into that category out of all 20,819 days.

	Total Fits	Passes Quality Control	Percent Passing QC
Primary rainband found	11,228 (53.9% of days)	7,988 (38.4% of days)	71.1%
Secondary rainband found	1,116 (5.4% of days)	698 (3.4% of days)	62.5%

Table 3.2: Details on the application of quality control (QC) criteria to primary rainbands.

Criterion	Number (% of total)
Primary rainband days before QC	11,228
Taiwan days (TW> 20%)	238 (2.1%)
$Q > .6$ (strong rainband)	7,522 (67.0%)
Double rainband ($Q_1 > .6$ and $Q_2 > .6$)	466 (4.2%)
Poor fit (Fails QC)	3002 (26.8%)

Table 3.3: Details on the application of quality control (QC) criteria to secondary rainbands. Type I and Type II fits are explained in greater detail in Section 3.4.

Criterion	Number (% of total)
Secondary rainband days before QC	1,116
Type I fit ($Q > .6$ and $Q_2 > .6$)	232 (20.8%)
Type II fit ($Q_1 > .6$ and $Q_2 > .6$)	466 (41.8%)
Poor fit (Fails QC)	418 (37.5%)

Table 3.4: Total number of rainband counts N (both primary counts N_1 and secondary counts N_2), frequency of primary and secondary rainbands and latitude and intensity (mm day^{-1}) of rainbands during the Spring Rains, Pre-Meiyu, Meiyu, Post-Meiyu, Fall Rains and for the full year. Post-Meiyu rainbands are further categorized by whether they occur north or south of 27°N, since events in that season have very different properties depending on latitude. We also list the decorrelation timescale τ_1 and τ_2 of primary and secondary fronts (units of days). Statistics are compiled using both primary and secondary rainbands, and are very close to results using primary rainbands alone, except during the Post-Meiyu period when secondary rainbands are common. Standard deviations for latitude and intensity are obtained by a permutation method with 10,000 iterations.

				1951-2007 Means					
Time Period	N	N_1	1f. (%)	τ_1 (days)	N_2	2f. (%)	τ_2 (days)	Lat. (°)	Int. (mm day^{-1})
Spring Rains (60-120)	1661	1635	47.0 ± 1.2	1.96	26	0.7 ± 0.1	.95	$27.5 \pm .1$	$20.1 \pm .4$
Pre-Meiyu (121-160)	1371	1279	56.1 ± 1.5	2.01	92	4.0 ± 0.4	.98	$27.4 \pm .2$	$25.5 \pm .5$
Meiyu (161-200)	1688	1499	65.8 ± 1.5	2.19	189	8.3 ± 0.6	1.11	$29.5 \pm .2$	$28.3 \pm .5$
Post-Meiyu (201-273)	2113	1757	42.2 ± 1.1	1.91	356	8.6 ± 0.5	1.44	$29.9 \pm .2$	$25.6 \pm .5$
Post-Meiyu, $> 27°$N	1368	1215	27.1 ± 1.0	-	153	3.4 ± 0.3	-	$33.3 \pm .2$	$23.9 \pm .5$
Post-Meiyu, $< 27°$N	745	556	15.2 ± 0.8	-	189	5.1 ± 0.4	-	$23.7 \pm .1$	$28.8 \pm .9$
Fall Rains (274-320)	744	714	26.6 ± 1.3	2.15	30	1.1 ± 0.2	1.48	$29.2 \pm .3$	$20.5 \pm .7$
Full Year (1-365)	8682	7984	38.4 ± 0.5	1.81	698	3.4 ± 0.1	1.12	$28.6 \pm .1$	$23.5 \pm .2$

Table 3.5: Change in frequency of primary and secondary rainbands between 1951-1979 and 1980-2007, with standard deviation of mean and p-value of change calculated analytically. Statistically significant changes at the 95%/99% level are indicated by bold font/bold font and asterisk respectively.

	Primary rainband %			Secondary rainband %		
Time Period	'51-'79	'80-'07	p	'51-'79	'80-'07	p
Spring Rains (60-120)	46.4 ± 1.7	47.7 ± 1.7	.70	0.8 ± .2	0.7 ± .2	.38
Pre-Meiyu (121-160)	**59.0 ± 2.0**	**53.0 ± 2.1**	**.020**	4.2 ± .6	3.8 ± .6	.32
Meiyu (161-200)	66.8 ± 2.0	64.6 ± 2.1	.23	7.4 ± .8	9.2 ± .9	.93
Post-Meiyu (201-273)	42.5 ± 1.5	42.0 ± 1.5	.41	9.2 ± .8	7.8 ± .7	.084
Post-Meiyu, > 27°N	27.8 ± 1.3	26.4 ± 1.3	.24	3.8 ± .5	2.9 ± .4	.082
Post-Meiyu, < 27°N	14.7 ± 1.1	15.6 ± 1.1	.71	5.4 ± .6	4.9 ± .6	.27
Fall Rains (274-320)	25.8 ± 1.7	27.6 ± 1.8	.77	1.0 ± .3	1.2 ± .4	.65
Full Year (1-365)	38.6 ± 0.6	38.1 ± 0.6	.31	3.4 ± .2	3.3 ± .2	.36

Table 3.6: Change in latitude and intensity of rainbands between 1951-1979 and 1980-2007, with standard deviation of mean and p-value of change both calculated by a permutation test with 10,000 iterations. Statistically significant changes at the 95%/99% level are indicated by bold font/bold font and asterisk respectively.

	Rainband latitude (°)			Intensity (mm day^{-1})		
Time Period	'51-'79	'80-'07	p	'51-'79	'80-'07	p
Spring Rains (60-120)	**27.6 ± .2**	**27.3 ± .2**	**.020**	**19.7 ± .5**	**20.5 ± .5**	**.984**
Pre-Meiyu (121-160)	27.5 ± .3	27.4 ± .3	.29	25.4 ± .7	25.6 ± .8	.72
Meiyu (161-200)	29.6 ± .3	29.4 ± .3	.24	28.2 ± .8	28.4 ± .8	.71
Post-Meiyu (201-273)	**30.2 ± .3***	**29.6 ± .3***	**.0048***	25.5 ± .7	25.7 ± .7	.71
Post-Meiyu, > 27°N	**33.6 ± .2***	**32.9 ± .3***	**.0003***	23.5 ± .7	24.2 ± .7	.92
Post-Meiyu, < 27°N	23.7 ± .1	23.8 ± .2	.83	29.1 ± 1.3	28.3 ± 1.4	.20
Fall Rains (274-320)	29.1 ± .4	29.3 ± .4	.79	20.3 ± 1.0	20.8 ± .9	.76
Full Year (1-365)	**28.7 ± .1***	**28.5 ± .1***	**.0032***	23.3 ± .3	23.6 ± .3	.95

Table 3.7: Change in frequency of primary and secondary rainbands between 1979-1993 and 1994-2007, with standard deviation of mean and p-value of change calculated analytically. No changes below are statistically significant at a 95% level.

	Primary rainband %			Secondary rainband %		
Time Period	'79-'93	'94-'07	p	'79-'93	'94-'07	p
Spring Rains (60-120)	50.0 ± 2.3	45.4 ± 2.4	.087	0.9 ± .3	0.5 ± .2	.14
Pre-Meiyu (121-160)	53.0 ± 2.9	53.2 ± 3.0	.52	3.5 ± .7	4.1 ± .8	.71
Meiyu (161-200)	63.7 ± 2.9	64.8 ± 3.0	.61	8.7 ± 1.2	9.5 ± 1.3	.67
Post-Meiyu (201-273)	41.6 ± 2.1	42.7 ± 2.1	.63	8.0 ± 1.0	8.0 ± 1.0	.50
Post-Meiyu, > 27°N	27.2 ± 1.9	25.2 ± 1.9	.23	3.1 ± .6	2.9 ± .6	.42
Post-Meiyu, < 27°N	14.4 ± 1.5	17.4 ± 1.6	.91	4.9 ± .8	5.1 ± .8	.55
Fall Rains (274-320)	26.4 ± 2.4	27.0 ± 2.5	.58	1.6 ± .6	0.8 ± .4	.13
Full Year (1-365)	37.9 ± 0.9	38.2 ± 0.9	.59	3.3 ± .3	3.3 ± .3	.52

Table 3.8: Change in latitude and intensity of rainbands between 1979-1993 and 1994-2007, with standard deviation of mean and p-value of change both calculated by a permutation test with 10,000 iterations. Statistically significant changes at the 95%/99% level are indicated by bold font/bold font and asterisk respectively.

	Rainband latitude (°)			Intensity (mm day^{-1})		
Time Period	'79-'93	'94-'07	p	'79-'93	'94-'07	p
Spring Rains (60-120)	27.2 ± .3	27.5 ± .3	.967	20.5 ± .7	20.6 ± .8	.54
Pre-Meiyu (121-160)	27.4 ± .4	27.2 ± .4	.23	25.0 ± 1.0	26.2 ± 1.1	.94
Meiyu (161-200)	**30.0 ± .4***	**28.9 ± .4***	**.0002***	**27.3 ± 1.1***	**29.8 ± 1.1***	**.9994***
Post-Meiyu (201-273)	29.8 ± .4	29.3 ± .5	.092	25.9 ± .9	25.4 ± .9	.28
Post-Meiyu, > 27°N	32.8 ± .3	33.0 ± .4	.80	24.4 ± 1.0	23.9 ± 1.1	.24
Post-Meiyu, < 27°N	23.8 ± .2	23.8 ± .2	.48	28.7 ± 1.8	27.9 ± 1.7	.28
Fall Rains (274-320)	**28.9 ± .5**	**29.7 ± .6**	**.982**	20.1 ± 1.4	21.7 ± 1.4	.94
Full Year (1-365)	28.6 ± .2	28.4 ± .2	.13	**23.3 ± .4**	**24.0 ± .4**	**.982**

Table 3.9: Mean and standard deviation of mean for metrics M_1 to M_8 for 1951-1979. M_1: Latitude of maximum daily rainfall (°). M_2: Intensity-weighted centroid of daily rainfall (°). M_3: Intensity of maximum rainfall over China (100-123°E and 20-40°N, mm day^{-1}). M_4: Area-averaged intensity of China rainfall (mm day^{-1}). M_5: Area-averaged intensity of North China rainfall (107.5-125°E and 37-42°N, mm day^{-1}). M_6: Mean intensity of South China rainfall (107.5-122.5°E and 27-33°N, mm day^{-1}). M_7: Frequency of North China rainfall (%). M_8: Frequency of South China rainfall (%). *Frequency* denotes percentage of days where mean rainfall over specified area exceeds 1 mm day^{-1}. Standard deviations of means are obtained by a permutation method with 10,000 iterations. Statistically significant changes at the 95%/99% level are indicated by bold font/bold font and asterisk respectively as subsequently calculated in Table 3.12.

1951-1979 Means

Time Period	M_1	M_2	M_3	M_4	M_5	M_6	M_7	M_8
Spring Rains (Mar 1-Apr 30, 60-120)	26.3 ± 0.2	**27.9 ± 0.1**	31.2 ± 1.1	2.6 ± 0.1	.52 ± 0.05	3.9 ± .2	25.0 ± 2.0	71.7 ± 2.1
Pre-Meiyu (May 1-Jun 9, 121-160)	25.7 ± 0.2	27.6 ± 0.1	59.4 ± 1.9	4.4 ± 0.2	1.20 ± 0.11	5.5 ± .3	47.1 ± 3.0	82.6 ± 2.2
Meiyu (Jun 10-Jul 19, 161-120)	27.9 ± 0.3	29.1 ± 0.2	72.5 ± 2.1	5.1 ± 0.1	2.78 ± 0.18	5.9 ± .3	81.1 ± 2.4	91.0 ± 1.7
Post-Meiyu (Jul 20-Sep 30)	27.4 ± 0.3	29.4 ± 0.1	69.1 ± 1.9	4.1 ± 0.1	**3.20 ± 0.16***	3.7 ± .2	76.4 ± 1.8	82.0 ± 1.7
Fall Rains (Oct 1-Nov 16)	25.6 ± 0.2	28.5 ± 0.2	36.9 ± 1.8	1.9 ± 0.1	.76 ± 0.09	2.3 ± .2	30.7 ± 2.5	57.2 ± 2.6
Full Year (1-365)	26.2 ± 0.1	28.3 ± 0.1	43.5 ± 0.7	2.8 ± 0.1	**1.31 ± 0.05**	3.4 ± .1	40.0 ± 1.0	67.7 ± 1.0

Table 3.10: Mean and standard deviation of mean of metrics M_1 to M_8 for 1980-2007. Standard deviations of means are obtained by a permutation method with 10,000 iterations. Statistically significant changes at the 95%/99% level are indicated by bold font/bold font and asterisk respectively as subsequently calculated in Table 3.12.

1980-2007 Means

Time Period	M_1	M_2	M_3	M_4	M_5	M_6	M_7	M_8
Spring Rains (Mar 1-Apr 30, 60-120)	26.2 ± 0.2	**27.6 ± 0.1**	32.4 ± 1.0	2.6 ± 0.1	.51 ± 0.06	3.8 ± .2	24.1 ± 2.1	72.5 ± 2.2
Pre-Meiyu (May 1-Jun 9, 121-160)	25.4 ± 0.2	27.7 ± 0.2	57.0 ± 1.8	4.2 ± 0.2	1.31 ± 0.12	5.0 ± .3	48.8 ± 3.0	79.6 ± 2.4
Meiyu (Jun 10-Jul 19, 161-120)	27.6 ± 0.3	29.1 ± 0.1	73.6 ± 2.2	5.2 ± 0.1	2.79 ± 0.18	6.4 ± .3	81.3 ± 2.3	92.1 ± 1.6
Post-Meiyu (Jul 20-Sep 30)	27.0 ± 0.2	29.2 ± 0.1	67.5 ± 1.9	4.0 ± 0.1	**2.70 ± 0.14***	3.9 ± .2	75.3 ± 1.9	85.5 ± 1.6
Fall Rains (Oct 1-Nov 16)	26.0 ± 0.3	28.5 ± 0.2	36.4 ± 2.1	1.8 ± 0.1	.65 ± 0.08	2.4 ± .2	28.0 ± 2.5	54.7 ± 2.8
Full Year (1-365)	26.2 ± 0.1	28.2 ± 0.1	43.1 ± 0.7	2.8 ± 0.1	**1.20 ± 0.04**	3.4 ± .1	39.4 ± 1.0	68.6 ± 1.0

Table 3.11: Autocorrelation timescale of metrics M_1-M_8. In subsequent calculations of significance, the block length for moving blocks bootstrapping is chosen for each season by rounding to the nearest whole number. Alternative choices of block length do not strongly influence estimations of significance.

	1980-2007 Means							
Time Period	M_1	M_2	M_3	M_4	M_5	M_6	M_7	M_8
Spring Rains (Mar 1-Apr 30, 60-120)	2.20	2.52	2.49	1.77	1.94	1.57	1.60	1.92
Pre-Meiyu (May 1-Jun 9, 121-160)	2.08	2.22	2.02	1.97	1.66	1.66	1.92	1.92
Meiyu (Jun 10-Jul 19, 161-120)	2.71	3.65	2.32	3.38	2.22	3.47	2.01	2.10
Post-Meiyu (Jul 20-Sep 30)	1.93	2.76	2.05	3.20	2.31	3.24	2.13	2.46
Fall Rains (Oct 1-Nov 16)	1.58	2.69	3.32	3.14	1.37	1.37	1.44	3.57
Full Year (1-365)	2.16	3.03	2.56	2.75	2.14	2.14	1.84	2.82

Table 3.12: Significance level p of changes in metrics M_1-M_8 between 1951-1979 and 1980-2007, as calculated by a moving blocks bootstrap for latitude and intensity metrics with 10,000 iterations and block length of τ rounded up to nearest integer, and analytically calculated using effective degrees of freedom $N = n/\tau$ for frequency metrics M_7 and M_8. Statistically significant changes at the 95%/99% level are indicated by bold font/bold font and asterisk respectively.

	1980-2007 Means							
Time Period	M_1	M_2	M_3	M_4	M_5	M_6	M_7	M_8
Spring Rains (Mar 1-Apr 30, 60-120)	.180	**.017**	.850	.414	.346	.320	.298	.649
Pre-Meiyu (May 1-Jun 9, 121-160)	.077	.819	.080	.154	.871	.038	.729	.091
Meiyu (Jun 10-Jul 19, 161-120)	.091	.468	.696	.808	.503	.943	.538	.745
Post-Meiyu (Jul 20-Sep 30)	.046	.150	.162	.132	**.0004***	.848	.296	.975
Fall Rains (Oct 1-Nov 16)	.965	.412	.442	.154	.049	.620	.107	.244
Full Year (1-365)	.726	.068	.314	.302	**.0068**	.776	.242	.784

Table 3.13: Statistical significance (express as p-value) of change in distribution of latitude and intensity of rainbands between 1951-1979 and 1980-2007, as calculated by a bootstrap Kolmogorov-Smirnov (K-S) and bootstrap Anderson-Darling (A-D) test, each with 10,000 iterations. Statistically significant changes at the 95%/99% level are indicated by bold font/bold font and asterisk respectively.

	Latitude (°)		Intensity (mm day^{-1})	
Time Period	K-S	A-D	K-S	A-D
Spring Rains (Mar 1-Apr 30, 60-120)	.086	.037	.19	.083
Pre-Meiyu (May 1-Jun 9, 121-160)	.24	.086	.94	.90
Meiyu (Jun 10-Jul 19, 161-120)	.30	.21	.25	.40
Post-Meiyu (Jul 20-Sep 30)	**.0073**	**.0018***	.28	.24
Post-Meiyu (Jul 20-Sep 30), $> 28°N$	**.0010***	**.0001***	.04	.10
Post-Meiyu (Jul 20-Sep 30), $< 28°N$	.38	.33	.53	.62
Fall Rains (Oct 1-Nov 16)	.23	.15	.94	.83
Full Year (1-365)	.075	**.016**	.26	.12

Table 3.14: Statistical significance (expressed as p-value) of change in distribution of latitude and intensity of rainbands between 1979-1993 and 1994-2007, as calculated by a bootstrap Kolmogorov-Smirnov (K-S) and bootstrap Anderson-Darling (A-D) test, each with 10,000 iterations. Statistically significant changes at the 95%/99% level are indicated by bold font/bold font and asterisk respectively.

	Latitude (°)		Intensity (mm day^{-1})	
Time Period	K-S	A-D	K-S	A-D
Spring Rains (Mar 1-Apr 30, 60-120)	.34	.12	.35	.60
Pre-Meiyu (May 1-Jun 9, 121-160)	.76	.57	.32	.29
Meiyu (Jun 10-Jul 19, 161-120)	**.0006***	**.0002***	**.0009***	**.0006***
Post-Meiyu (Jul 20-Sep 30)	.14	.15	.48	.87
Post-Meiyu (Jul 20-Sep 30), $> 28°N$	.13	.35	.26	.35
Post-Meiyu (Jul 20-Sep 30), $< 28°N$	.67	.60	.70	.36
Fall Rains (Oct 1-Nov 16)	.16	.092	.40	.17
Full Year (1-365)	.14	.29	.090	.062

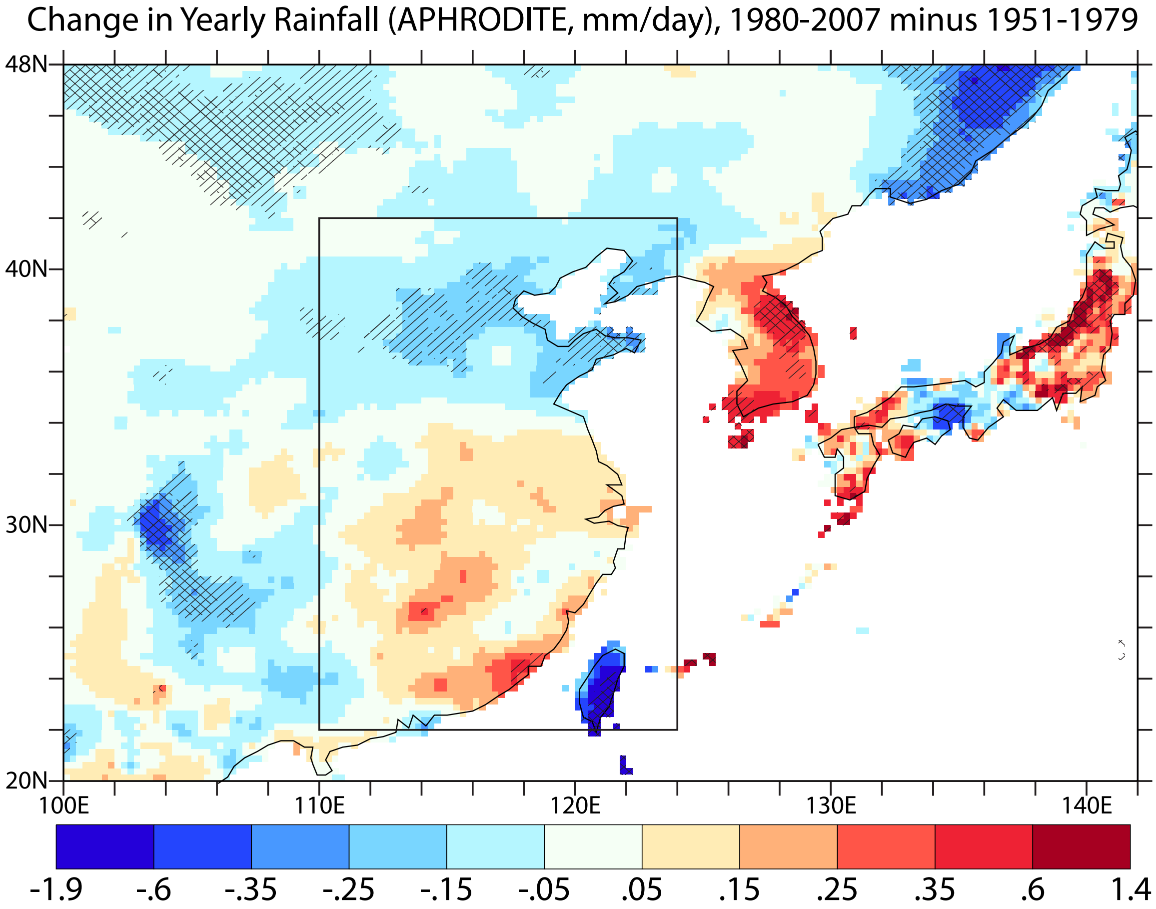

Figure 3.1: Difference in yearly mean rainfall between 1980-2007 and 1951-1979. The South Flood-North Drought pattern is visible between 110-124°E and 22-42°N over mainland China (marked by box). Changes significant at a 95%/99% level are marked with single/double cross-hatches respectively.

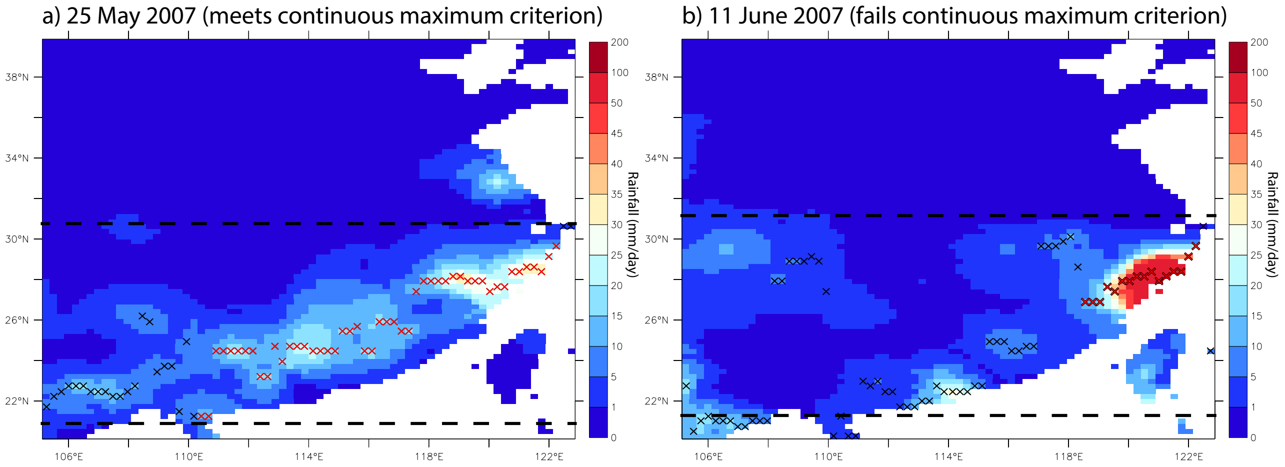
a) 25 May 2007 (meets continuous maximum criterion)

b) 11 June 2007 (fails continuous maximum criterion)

Figure 3.2: On each day, RDA first checks whether a continuous band of precipitation maxima exceeding 10 mm day^{-1} exists that spans over 5 degrees of longitude. If so, a rainband fit is attempted. In panels a and b, the latitude of maximum precipitation at each longitude is marked with a black X. The longest continuous chain of maxima exceeding 10 mm day^{-1} is marked in red. a) 25 May 2007 - the continuous maximum criterion is met and a fit is attempted. b) 11 June 2007 - although there is abundant rainfall in some locations, no band is visible and the continuous maximum criterion is failed. No fit is attempted.

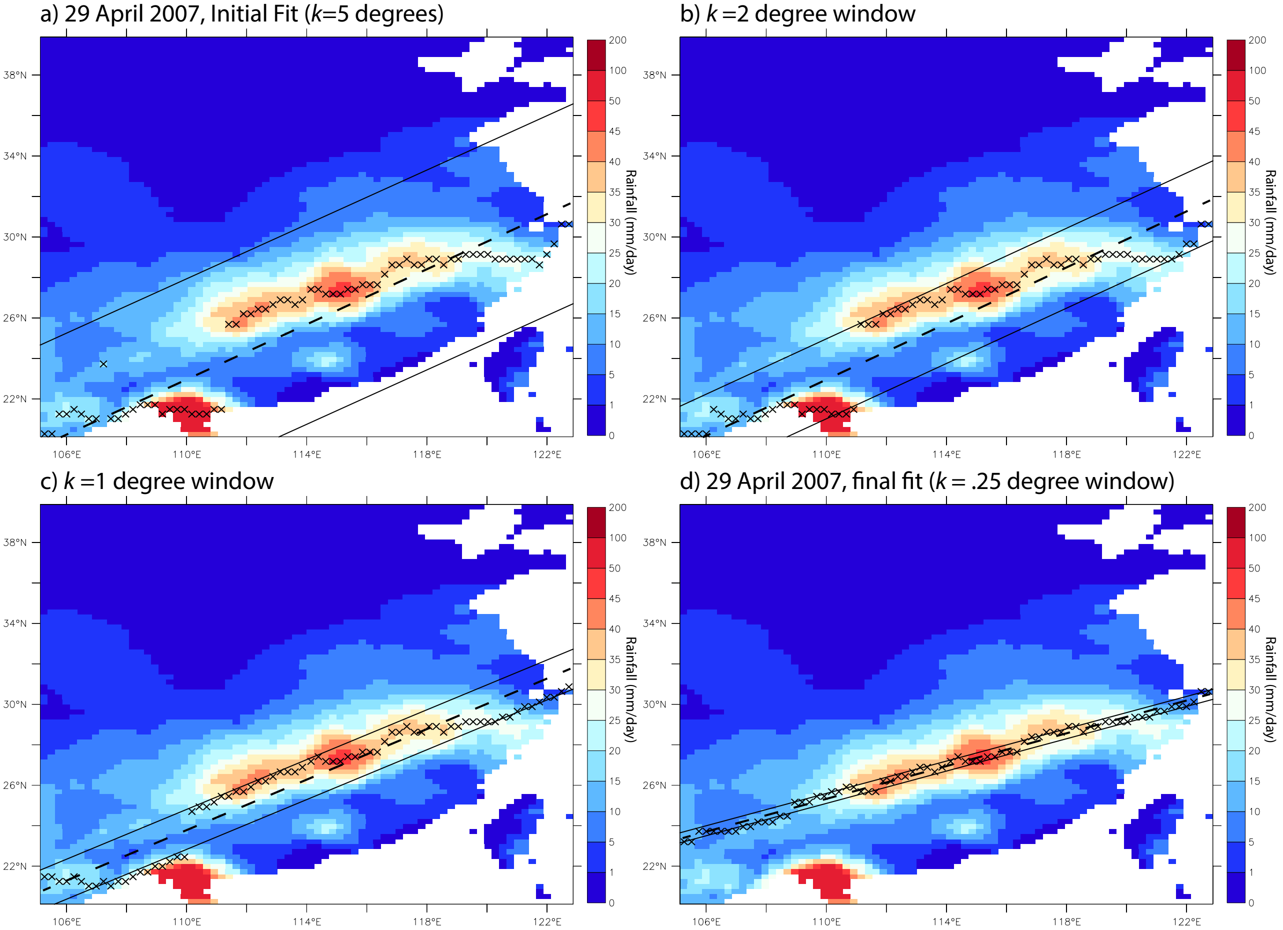

Figure 3.3: Display of the functionality of the recursive convergent fit. Dashed line shows estimated rainband position before each iteration and the solid lines indicate the window within we search for maxima. On 29 April 2007, a strong maximum in southernmost China skews our initial rainband fit (a), but the algorithm eventually converges on its true position via tighter windowing (d).

a) August 18 2007 (Typhoon Sepat) - ``Taiwan Fraction” > 20%, **no fit**

b) 4 June 2007 - Q>.6, **successful fit**

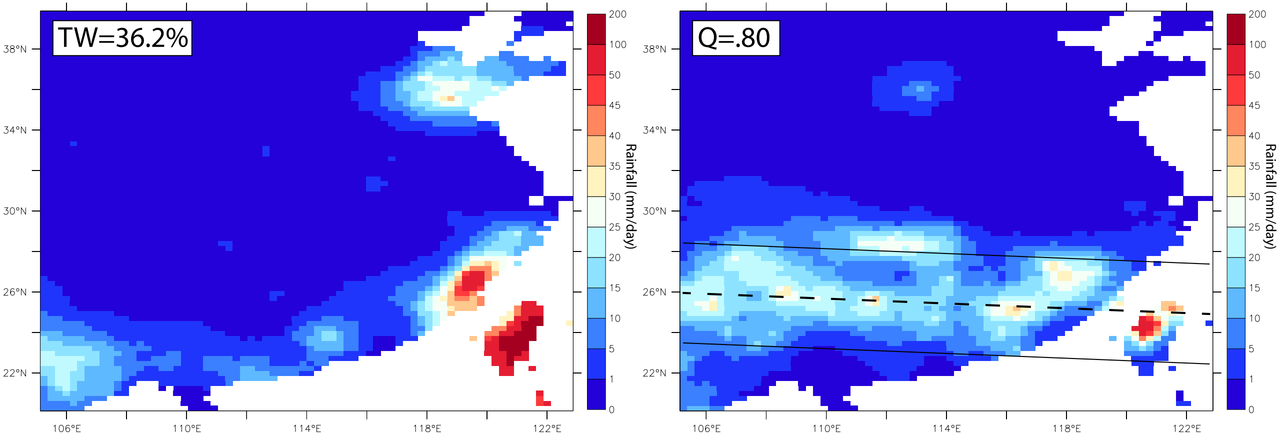

c) 17 April 2007 - Q<.6, **no fit**

d) 21 May 2007 (Q<.6, but Q1>.6 and Q2>.6) - double rainband, **fit**

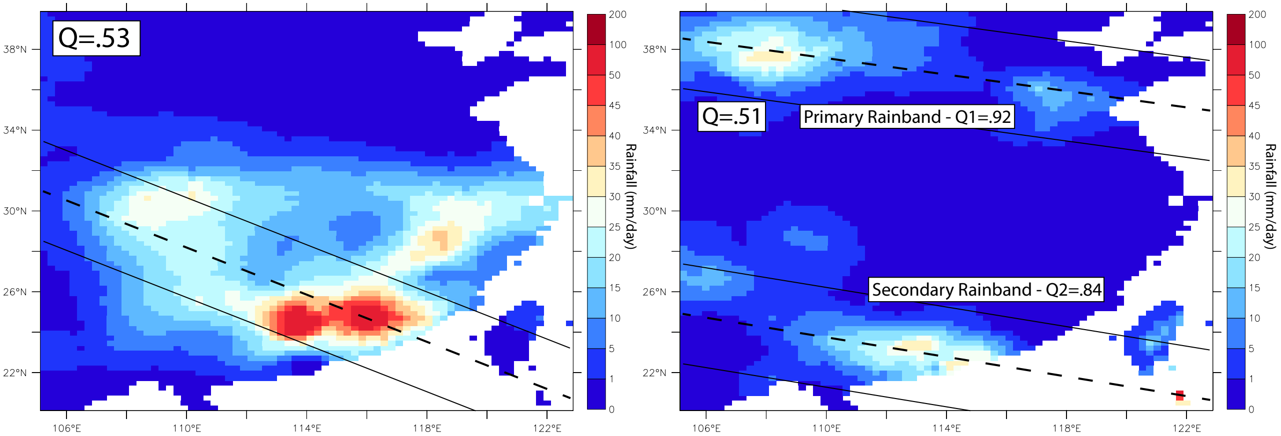

Figure 3.4: A quality control algorithm is used to exclude poor fits. a) 18 August 2007 - Days with a high Taiwan fraction (here, corresponding to the passage of Typhoon Sepat) are excluded from our statistics. b) June 4 2007 - A high-quality fit is achieved. c) 17 April 2007 - Although a tentative fit is obtained, it explains the distribution of rainfall poorly and is therefore unsuccessful. d) 21 May 2007 (same day as Figure 3.5) - An initial fit appears to be of poor quality ($Q < .6$). However, after finding a secondary rainband, we determine that conditional quality scores Q_1 and Q_2 are sufficiently high, and the double rainband fit is successful.

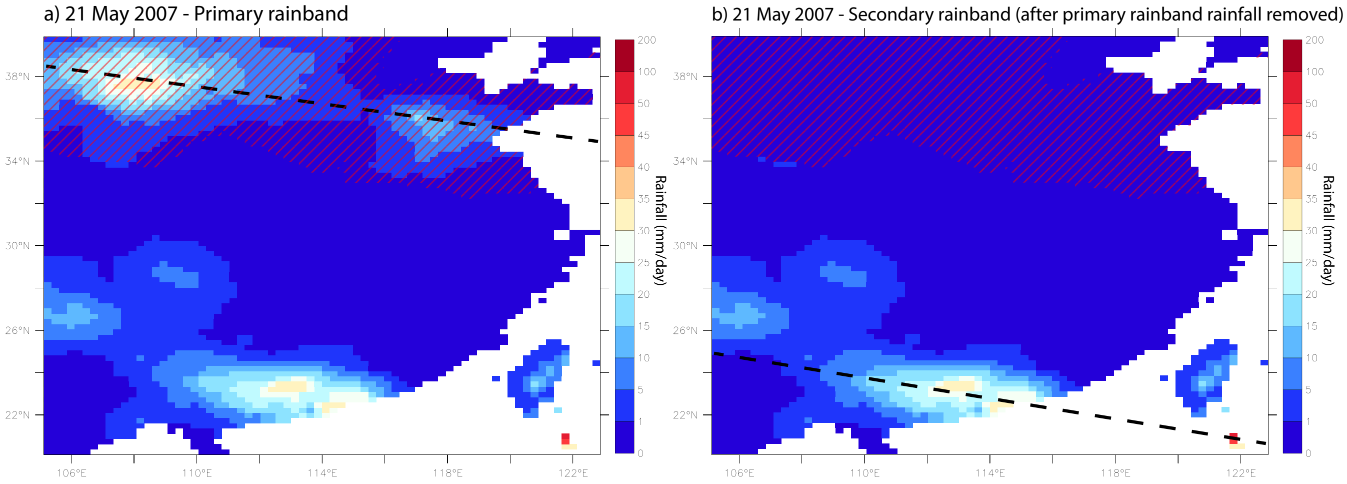
a) 21 May 2007 - Primary rainband

b) 21 May 2007 - Secondary rainband (after primary rainband rainfall removed)

Figure 3.5: a) The first pass of the recursive fit algorithm converges on the strongest rainband, around 37°N (defined as the "primary rainband"). The *banded rainfall* associated with the primary band is shaded with red hatchmarks. b) All banded rainfall from the primary band is removed, and we check for the presence of another rainband (a "secondary rainband"), again using the continuous maximum criterion. When this criterion is satisfied, we find the secondary rainband's position with the recursive fit algorithm.

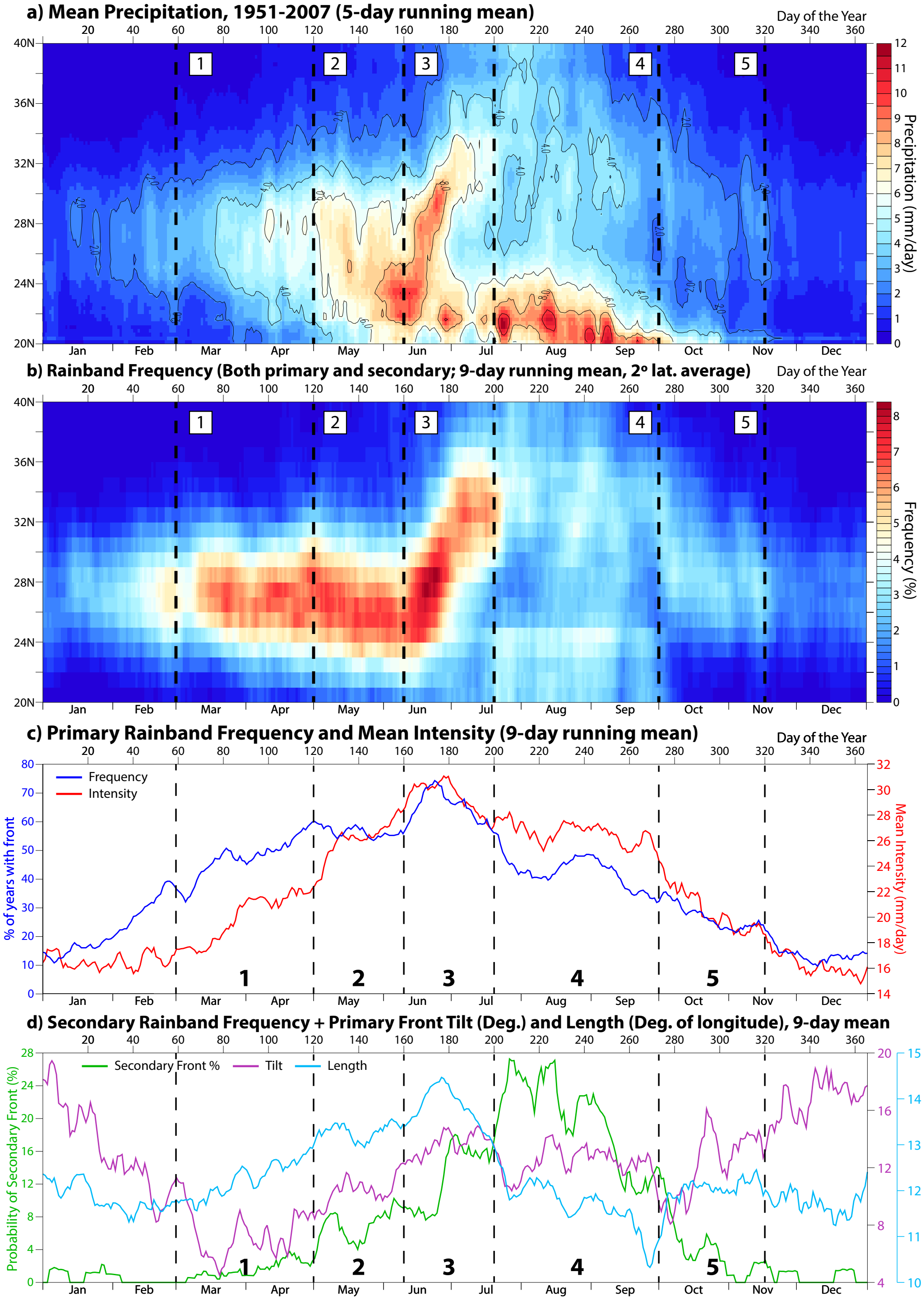
a) Mean Precipitation, 1951-2007 (5-day running mean)

b) Rainband Frequency (Both primary and secondary; 9-day running mean, 2º lat. average)

c) Primary Rainband Frequency and Mean Intensity (9-day running mean)

d) Secondary Rainband Frequency + Primary Front Tilt (Deg.) and Length (Deg. of longitude), 9-day mean

Figure 3.6: Climatology of East Asian rainfall and rainbands, 1951-2007, with important time periods marked as follows: 1 - Spring Rains; 2 - Pre-Meiyu; 3 - Meiyu; 4 - Post-Meiyu; 5 - Fall Rains. a) Hovmöller diagram of precipitation (100-123°E longitudinal average); b) Hovmöller diagram of absolute probability of observing a rainband (both primary and secondary), smoothed in time with a 9-day and 2°-running box filter; c) Probability of primary rainband occurrence and mean intensity (9-day running mean); d) The conditional probability of a secondary rainband given the presence of a primary rainband, as well as the mean tilt and length of primary rainband events (9-day running mean).

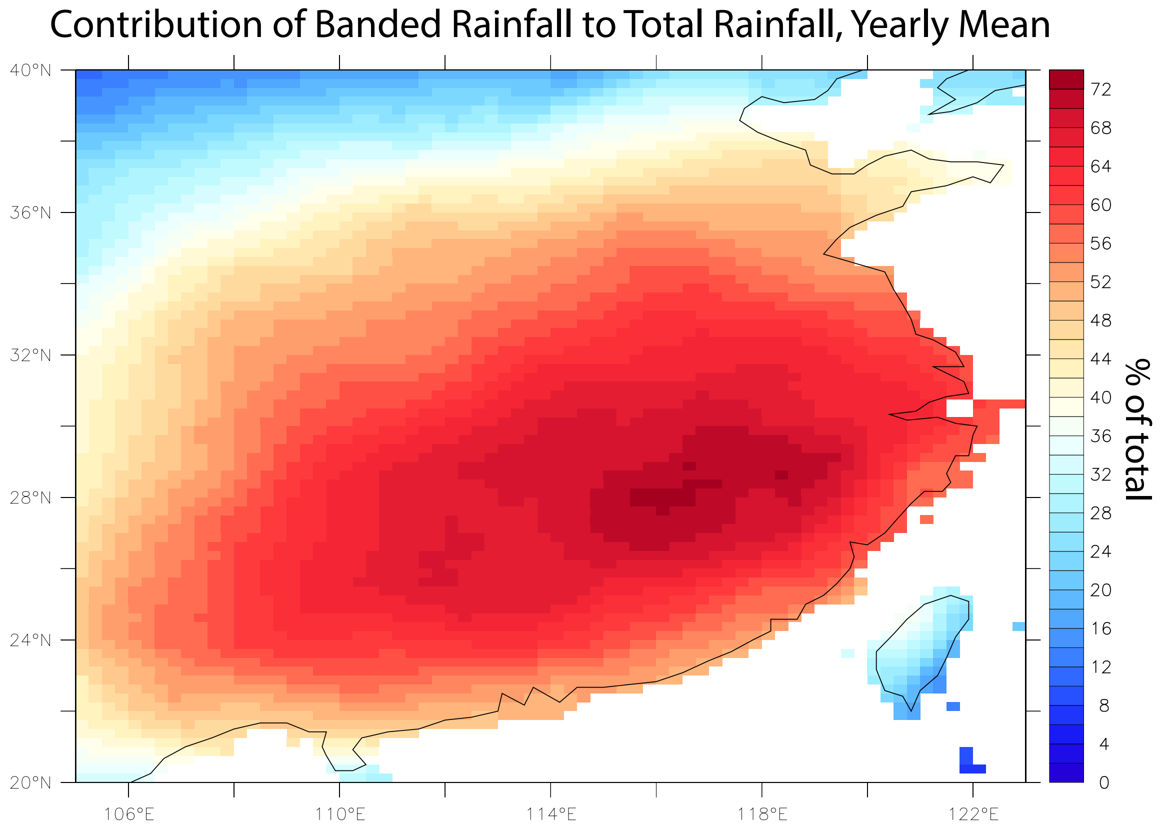

Figure 3.7: Yearly mean percentage of total rainfall that falls as banded rainfall. On a given day, banded rainfall consists of all rainfall falling within 4° of a rainband axis and rainfall at any other adjacent point exceeding 10 mm day^{-1}.

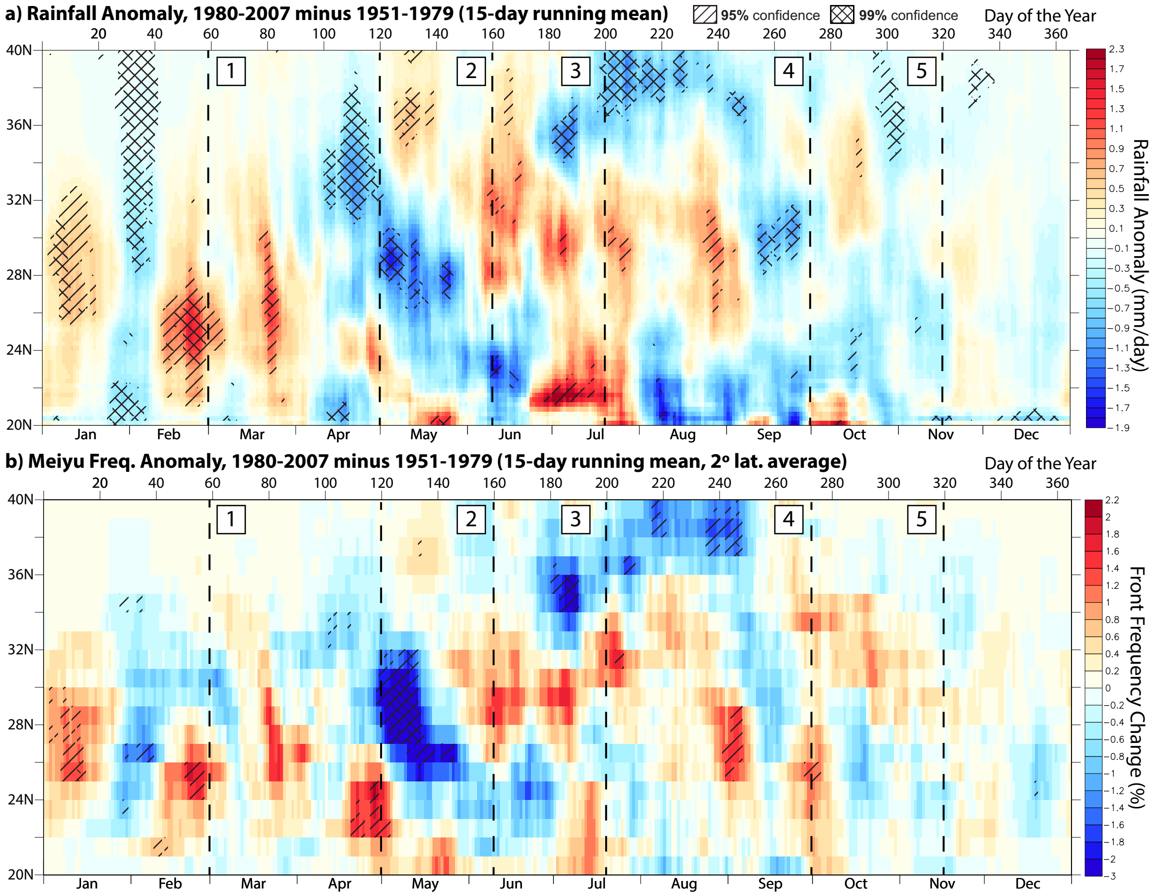

Figure 3.8: a) 15-day running mean of the change in rainfall between 1951-1979 and 1980-07, with 95%/99% confidence level marked by single/double cross-hatches; b) 15-day running mean of the change in rainband frequency between 1951-1979 and 1980-07, with two-degree smoothing in latitude and confidence levels marked as in a). The significance of rainfall changes is calculated by a permutation method. Time periods are marked as in Figure 3.6: 1 - Spring Rains; 2 - Pre-Meiyu; 3 - Meiyu; 4 - Post-Meiyu; 5 - Fall Rains.

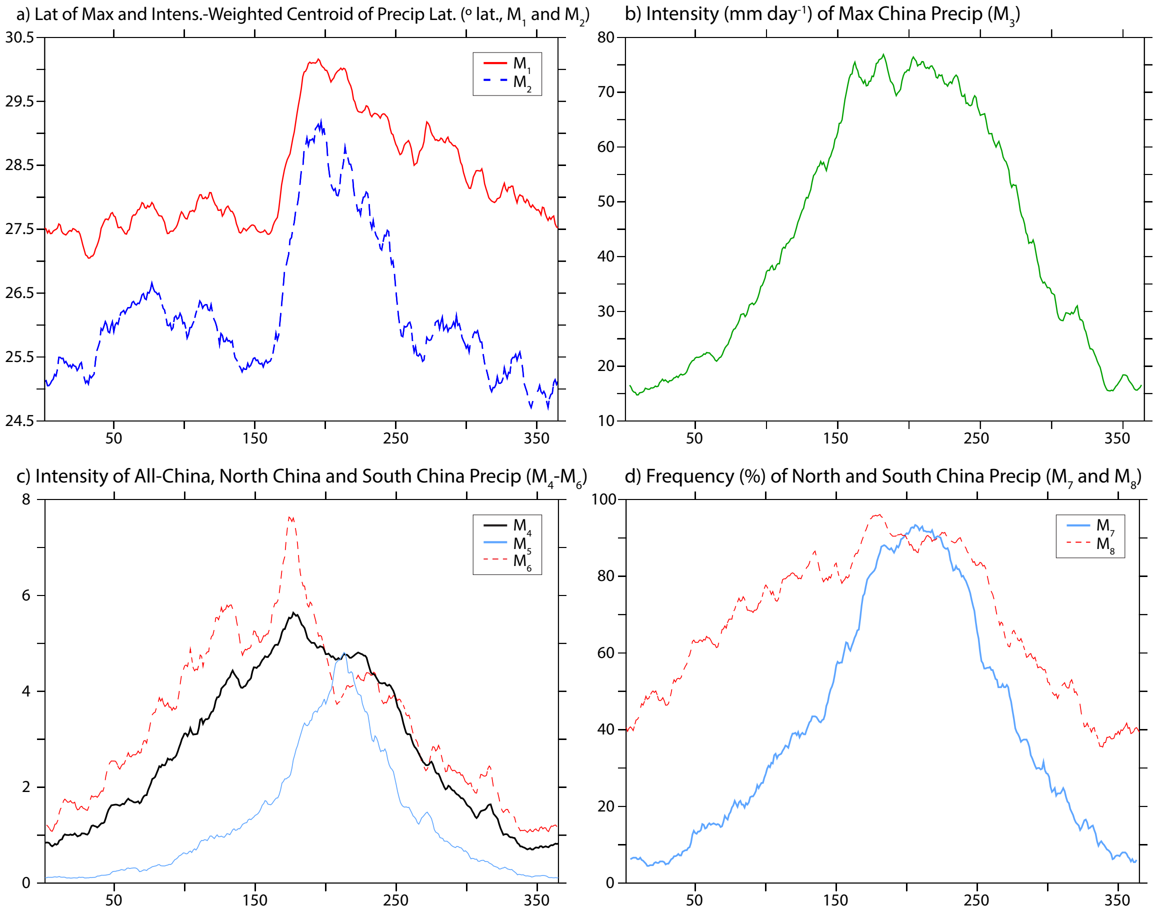

Figure 3.9: Yearly climatology of alternative metrics of China rainfall $M_1 - M_8$. a) Latitude of maximum precipitation (blue dash, M_1) and intensity-weighted centroid of precipitation latitude (red, M_2); b) Intensity of maximum precipitation over China (M_3); c) Mean intensity of China rainfall (black, M_4), North China rainfall (thin light blue, M_5) and South China rainfall (red dash, M_6); d) Frequency of North China rainfall (light blue, M_7) and South China rainfall (red, M_8). China region is defined as 105-123°E and 20-40°N, North China as 107.5-125°E and 37-42°N and South China as 107.5-122.5°E and 27-33°N.

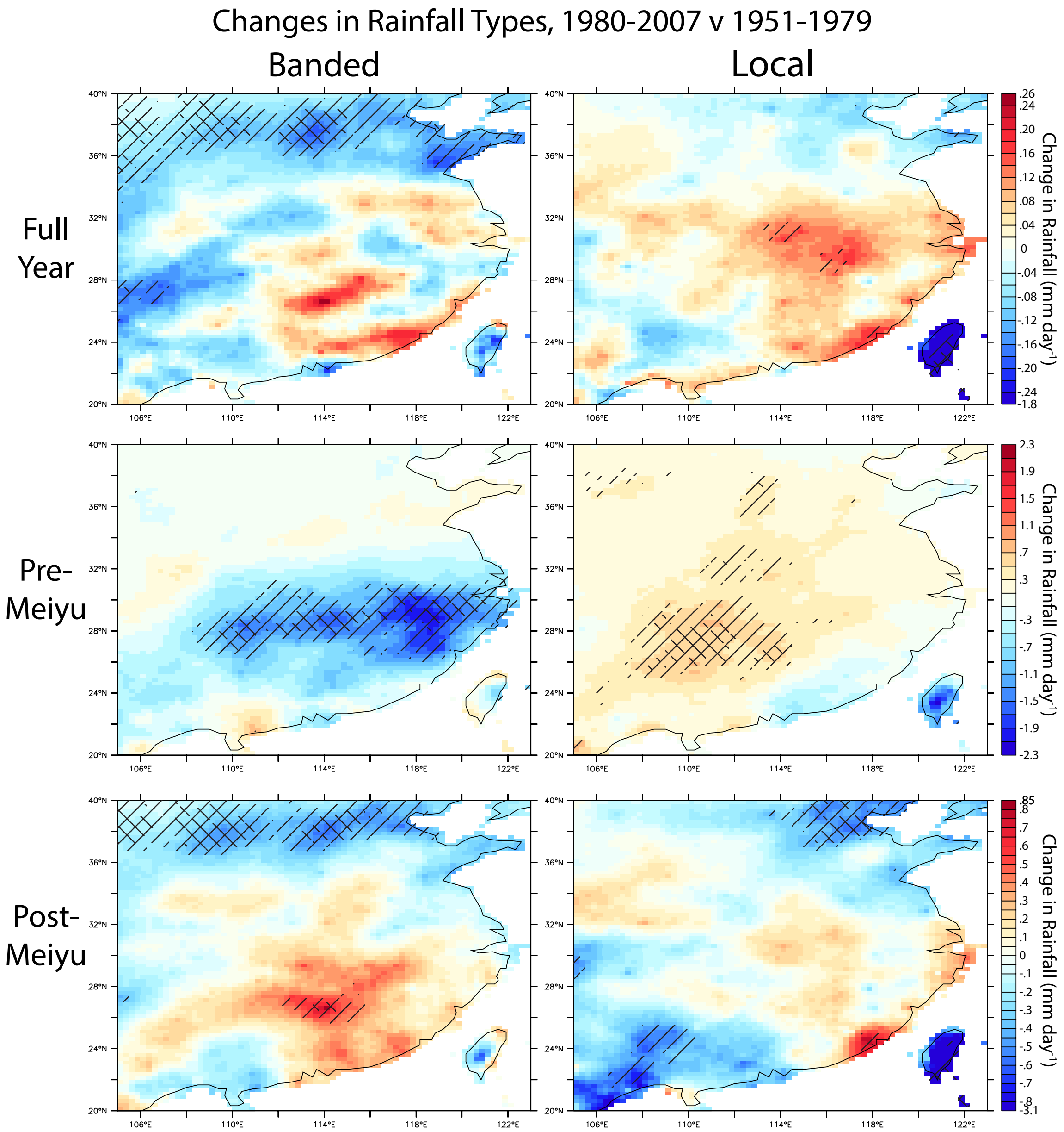

Figure 3.10: 1980-2007 versus 1951-1979 changes in banded and local rainfall for full year (a and b respectively), Pre-Meiyu (c and d) and Post-Meiyu (e and f), with significance at the 95%/99% level marked by single/double hatches. On a given day, *banded* rainfall consists of all rainfall falling within 4° of a rainband axis and rainfall at any other adjacent point exceeding 10 mm day^{-1}. *Local* rainfall includes all other rainfall.

Chapter 4

Role of Tropospheric Jet Changes in the Interannual Variability and Decadal Trend of Asian Monsoon Rainfall

4.1 Abstract

We have previously investigated the leading mode of July-August Asian monsoon variability (hereafter termed All-Asia EOF1) and argued that this mode manifests a coupling between the Himalayan Foothills and Yangtze River Valley. In this chapter, we investigate the manifestation of All-Asia EOF1 in JRA-55 reanalysis and associated atmospheric anomalies across the Northern Hemisphere. Extreme years of All-Asia EOF1 correspond to a global-scale Northern Hemisphere wavetrain known as the Circumglobal Teleconnection (CGT), leading to temperature and rainfall anomalies across the globe. Positive All-Asia EOF1 years are also correlated with a band of anomalous diabatic heating spanning the Himalayan foothills and Yangtze River valley also characterized by anomalous westerly moisture transport. Thus, JRA-55 reanalysis supports the hypothesis from Chapter 2 that changes in moisture transport across the Yunnan Plateau induce the All-Asia EOF1 pattern of rainfall response. In addition, we propose that East Asian heating can force the CGT, creating a trough and ridge pattern over central China and Siberia respectively that may contribute to the phase-locking of the CGT in summer, further strengthened by the effect of Asian high terrain.

Over East Asia, positive All-Asia EOF1 years feature a robust southward shift in the tropospheric jet, and vice-versa in negative years. We search for further links between the position of the East Asian jet and rainfall anomalies in the East Asian monsoon on an interannual and interdecadal time scale using the RDA catalog presented in Chapter 3. The frequency of banded rainfall during the Pre-Meiyu and the latitude of rainbands during the

Post-Meiyu are both found to covary with meridional shifts of the tropospheric jet. Furthermore, major late-twentieth-century changes in the frequency and latitude of frontal rainfall (the "South Flood-North Drought") are found to coincide with anomalies in East Asian jet latitude. The East Asian jet has likely responded both to decadal changes in regional temperature and to 20th-century global warming. Though the mid-latitudes force East Asian monsoon weather chaotically (the "Silk Road" pattern), idealized studies and high-resolution global climate models have begun to converge in their projections of future East Asian jet changes and the Circumglobal Teleconnection under 21st-century warming. Given the observational relationship shown herein between the East Asian jet, CGT and anomalous rainfall, the potential exists to improve projections of twenty-first-century rainfall change in China, which remained highly uncertain in the latest International Panel on Climate Change report (IPCC5).

4.2 Introduction

In many of the world's most populous regions, the duration and severity of monsoon rainfall dictates the well-being of the populace by controlling crop yields, flooding and freshwater supply. The history of monsoon study is therefore replete with attempts at its prediction dating back over a century, such as the India Meteorological Department (IMD)'s official seasonal forecast (available at `http://www.imd.gov.in/pages/monsoon_main.php`) and recent concerted efforts such as the 'Seasonal Prediction of the Indian Monsoon' (SPIM) project (Gadgil and Srinivasan, 2011). Nonetheless, IMD operational forecasts of the Indian monsoon demonstrated no skill over the years 1989-2012 (Wang et al., 2015). Past generations of global climate models have struggled even to produce a realistic mean state for the Indian monsoon (Gadgil, 2003), let alone its variability (Krishna Kumar et al., 2005).

An even bigger challenge awaits in the prediction of the future of the monsoon under global warming. Twenty-first-century changes in mean temperature and rainfall will impact the livelihood of billions (Barrios et al., 2010; Burke et al., 2015). Unfortunately, in the latest iteration of the Intergovernmental Panel on Climate Change report (IPCC5), it is acknowledged that models struggle to produce realistic patterns of rainfall in the Asian monsoon region due to the heterogeneity of high terrain (Christensen et al., 2011). Weak consensus exists between models on twenty-first-century rainfall increase in China under their RCP4.5 scenario, and only "medium confidence" in increasing rainfall during the South Asian summer monsoon. At a more fundamental level, even simplified (aquaplanet) versions of the CMIP5 models respond entirely differently under elementary climate perturbations such as a uniform 4K temperature increase, due primarily to their inability to parametrize moist convection and cloud formation in a physically realistic way (Stevens and Bony, 2013). Therefore, even in regions where the models do arrive at a consensus, it is not clear that their projections should be trusted. Meanwhile, from a theoretical standpoint, it is debated whether the future Asian monsoon could undergo nonlinear change under global warming (Zickfeld et al., 2005), or will instead evolve linearly (Boos and Storelvmo, 2016).

In this chapter, we focus on the leading mode of Asian monsoon rainfall variability, named All-Asia JA EOF1 in Day et al. (2015), and its relation to other regional and global modes of climate variability. All-Asia JA EOF1 (hereafter referred to as All-Asia EOF1 for convenience) features enhanced precipitation over the Himalayan Foothills and Yangtze River corridor in its positive phase and decreased precipitation over the Monsoon Zone, northern China and southernmost China, and vice-versa in its negative phase. We first find using composite analysis that All-Asia EOF1 is correlated with a wavelike pattern of anomalies across the Northern Hemisphere known as the Circumglobal Teleconnection (CGT). In the second, we find that the South Flood-North Drought pattern of twentieth-century rainfall change in China was also accompanied by changes in the East Asian jet. Thus, All-Asia EOF1 rainfall variability implies a corresponding set of atmospheric changes at the scale of the entire Northern Hemisphere.

The CGT and the East Asian tropospheric jet respond to global modes of climate variability and will be influenced by 21st-century global warming. The CGT is defined as the second EOF of summer midlatitude geopotential height variability (EOF1 reflects ENSO). In the past several decades, severe heat waves and droughts have been ascribed to high-wavenumber standing Rossby wave circulations (Schubert et al., 2011). In several cases, Eurasian heat waves were directly tied to South Asian monsoon extremes (Lau and Kim, 2012; Trenberth and Fasullo, 2012). Current debate investigates whether polar amplification observed in 20th-century warming will make midlatitude blocking events more frequent and severe (Francis and Vavrus, 2012), or not (Barnes, 2013; Hassanzadeh et al., 2014). The response of the the tropospheric jet to climate change has also been extensively studied. The jets marks the poleward boundary of the Hadley Cells (Bordoni and Schneider, 2008), and therefore shift in response to global changes in inter-hemispheric heating gradient(Chiang and Friedman, 2012). Therefore, it can be argued that the jet translates global climate forcings into regional climate change. Observations show a poleward shift in previous decades in response to global warming (Fu et al., 2006; Archer and Caldeira, 2008; Fu and Lin, 2011), but the opposite trend is found over East Asia (Yu and Zhou, 2007; Archer and Caldeira, 2008; Park and An, 2014b). The poleward expansion of the Hadley Cell is projected to continue under 21st-century warming (Frierson et al., 2007; Lu et al., 2007; Kang and Lu, 2012), but a recent study predicts that anomalous 21st-century heating of the eastern Pacific Ocean will continue to push the East Asian jet further equatorward (Park and An, 2014a).

In summary, much work has already been done to anticipate changes in the CGT and the tropospheric jet on a warmer planet. By showing in this chapter that both of these climate components and the All-Asia EOF1 mutually influence one another, we open the possibility of using projections of midlatitude blocking and shifting of the tropospheric jet on a warmer planet to inform projections of the 21st-century Asian monsoon.

4.3 Data and Methods

JRA-55 Reanalysis

We rely on the JRA-55 reanalysis product assembled by the Japanese Meterological Association (JMA) (Kobayashi et al., 2015; Harada et al., 2016). JRA-55 is a state-of-the-art 56-year (1958-2013) reanalysis product, the first since ERA-40 to cover the past half-century. The realism of model climate is notably improved from the previous generation product, JRA-25, due in part to a brand new assimilation scheme. Fields are calculated at a model resolution of up to 640 × 320 (.625° × .625°), with exact number of longitude points varying by latitude. The products used in this analysis are upscaled to 1.25° × 1.25°. Monthly fields at the 700-mb, 500-mb and 200-mb levels were used, as well as column-integrated values where applicable. We calculated monthly anomalies in JRA-55 fields for positive and negative composites of years (described below), and also calculated normalized anomalies by finding the monthly standard deviation of each field for each calendar month. For a field X and calendar month m, we calculate the monthly standard deviation σ_{X_m} as follows:

$$\sigma_{X_m}(x,y) = \left(\sum_{56\ years} \left(X_m(x,y,yr) - \overline{X_m(x,y)} \right)^2 \right)^{1/2}$$

Historical Precipitation and Temperature Records

We rely on the University of Delaware precipitation data set (hereafter referred to as UDEL) v4.01, available at .5° × .5° resolution (land only) for the years 1900-2014 (Matsuura and Willmott, n.d.). Data are assimilated from station records before being interpolated onto the grid, with quality control algorithms applied to weed out faulty records. For the testing of statistical significance, we use the same years as available in JRA-55, 1958-2013, which also feature higher station coverage than the first half of the 20th century.

Monthly temperature anomalies from 1958 to 2013 gridded at 1° × 1° resolution were obtained from the Berkeley Earth Surface Temperature project (hereafter referred to as BEST), freely available at `http://www.berkeleyearth.org/data/` (Rohde et al., 2012). BEST agrees closely with past historical temperature estimates, but the gridless methodology used can incorporate a wider range of temperature records (Rohde et al., 2013). According to their best estimate, global land mean temperature increased by .89 ± .06°C from 1950-1959 to 1990-1999. Therefore, in order to compare local temperature anomalies on an even footing, the temperature time series are detrended based on 1958-2013 local slope. At each point, we separate the time series into 12 separate monthly time series (each consisting of 56 Januarys, Februarys and so on) and then detrend each monthly time series based on the 56-point trend in that month.

Composite Analysis

We construct positive and negative composite anomalies for July and August from JRA-55 data, UDEL precipitation and BEST temperature. Positive composite years were chosen by selecting the five years between 1958 and 2007 when the value of All-Asia EOF1 was highest (Day et al., 2015). We then create a positive composite anomaly by averaging over fields in those five years and subtracting from the 56-year mean (1958-2013). The same procedure was repeated for the 5 most negative July All-Asia EOF1 years in the same timespan, and then the entire process repeated for the month of August. Further detail on selected years is included in Tables 4.1. Most figures in this paper show the *difference* between the positive and negative composites, or "inter-composite difference," except where otherwise stated.

Montecarlo Estimates of Statistical Significance

Two methods are used to calculate the statistical significance of inter-composite differences: An analytic calculation based on the monthly standard deviation, and a Montecarlo method that generates arbitrary composites with 10,000 iterations.

Analytic Calculation

The analytic method approximates the distribution of anomalies as Gaussian. For a field of interest X in month m, we construct positive composite X_{m+}, negative composite X_{m-} and normalized inter-composite difference Z_{X_m} with total number of observation months N and monthly standard deviation σ_{X_m}:

$$\begin{aligned}
X_{m+} &= \left(X_{m+,1} + X_{m+,2} + X_{m+,3} + X_{m+,4} + X_{m+,5}\right)/5 \\
X_{m-} &= \left(X_{m-,1} + X_{m-,2} + X_{m-,3} + X_{m-,4} + X_{m-,5}\right)/5 \\
Z_{X_m} &= \frac{N^{1/2}\left(X_{m+} - X_{m-}\right)}{\sigma_{X_m}}
\end{aligned}$$

Z_{X_m} can then be converted to a p-value assuming that anomalies are normally distributed.

Montecarlo Method

For each iteration of the Montecarlo method, we create random non-overlapping positive and negative composites of five random years each from any of the 56 Julys (and analogously for August) and then find the inter-composite difference at each spatial point. At the end of 10,000 iterations, we find an effective p-value at each point by comparing the actual composite difference to the 10,000 simulated differences. The Montecarlo method is generally found to be a much stricter test of significance. Figures showing statistical significance use Montecarlo-estimated p-values. We also calculate an additional p-value for the entire pattern, namely the probability that the total *area* exceeding a 95% confidence level could be obtained at random. Since we are particularly interested in the Northern Hemisphere midlatitudes, we sum the total significant area between 20°N and 65°N and divide by total area. This "pattern" p-value is listed on the top-right of figures when calculated with region of interest marked on each figure. Since the test statistic in this case is one-sided, a pattern p-value exceeding .95 would be significant at a 95% confidence level.

Jet Count Density

Schiemann et al. (2009) constructed a data set of jet "counts" in the Tibetan Plateau region (46° E-130° E, 17° N-58° N) from ERA-40 reanalysis for 1958-2001, where a count is defined as any local maximum in zonal wind with westerly magnitude greater than 30 m s^{-1}; further details can be found in section 2 of Schiemann et al. (2009). We show daily mean jet latitude averaged across $90° - 130°$E in Figure 4.13a and monthly anomalies in Figure 4.13b and c. Results are not sensitive to the choice of longitude range. Figure 4.10 presents contours of jet frequency estimated by a kernel density method, which estimates a probability distribution from a set of discrete data observations. The Schiemann et al. (2009) database is also tested for covariance with the Rainband Detection Algorithm (RDA) catalog from Chapter 3 as shown in Figure 4.13, with results described subsequently.

4.4 Composites of All-Asia EOF1 in JRA-55

Circumglobal Teleconnection

We build composites of the most positive and negative years of All-Asia EOF1 and find robust global change in upper-tropospheric height (Z200) across the Northern Hemisphere. The largest signal is a massive rise in geopotential height in the Tropics in the July composite, a known phenomenon in strong ENSO years (Figure 4.1), even though All-Asia EOF1 is not significantly correlated with ENSO. The absolute magnitude of anomalies in the Tropics remains less than in mid-latitudes because its variability is much lower (sidebar of Figure 4.1a). To focus on wavelike mid-latitude behavior, we subtract the zonal mean anomaly in subsequent figures where useful, as shown for instance in Figures 4.1c and 4.1d.

In July (Figure 4.2a), strong All-Asia EOF1 years are associated with a zonal wavenumber 5 standing wave spanning the entire Northern Hemisphere. Analyzing 200-mb geopotential height (Z200), pronounced positive lobes are visible over Russia, the eastern Pacific, western North America and the Azores, and negative lobes over Pakistan, northeast Asia and northern Europe. In August (Figure 4.2b), a similar pattern is obtained with some shifts: the northeast Asian lobe bifurcates into a Korean and Aleutian pair, the Siberian high strengthens and the North American high merges with that in the Eastern Pacific. Both the July and August Z200 anomaly patterns are significant at a 95% confidence level. Considering the mid-troposphere and near-surface, we find that geopotential height anomalies are mostly barotropic and remain visible at the 700-mb level, except for over Pakistan where the 200-

mb low is replaced by a surface high, and a belt from the eastern Tibetan Plateau eastward with 200-mb highs and 700-mb lows (Figure 4.5a-b). These reflect cooling over Pakistan and heating over northern India, the Yangtze River Valley and western Pacific. All patterns are significant at a 95% level except for Z700 in August.

These patterns strongly resembles the Circumglobal Teleconnection (hereafter CGT) studied in Ding and Wang (2005). Branstator (2002) originally found that, in regions of strong meridional temperature gradient such as East Asia, a pattern with zonal wavenumber 5 can extend around the globe, with the tropospheric jet serving as a waveguide favoring the zonal propagation of storms. They were able both to find evidence of such a mode in reanalysis and demonstrate its existence in a simplified model. Figure 1c of Branstator (2002) closely resembles our Figure 4.1d. Looking more closely at Figures 5b and c of Ding and Wang (2005) we find that they are practically identical to our Figures 4.2a and 4.2b (with sign inverted), including the set of changes between July and August. Furthermore, geopotential height anomalies of the studied global wavetrains in both Branstator (2002) and Ding and Wang (2005) are consistently barotropic except over India (Figure 4.2). It should be noted that the CGT was also found to operate in June and September; for our purposes, we focus on its manifestation in July and August. We conclude that the mid-latitude wavetrain associated with All-Asia EOF1 and the CGT as defined by Ding and Wang (2005) are the same pattern.

Another way of displaying the same wavetrain pattern is to consider the upper-level meridional wind (V200). Since the zonal mean of meridional wind is 0 and also near-zero in composites, waves are apparent without additional filtering (Branstator, 2002). Figure 4.3 shows V200 for the July and August composites. The number of lobes can easily be counted, and the July wavetrain appears to be of wavenumber 6 while August is of wavenumber 5. From the Aleutian Islands to the eastern United States, the pattern of meridional wind anomalies in fact reverses from July to August, while remaining largely similar over Eurasia, showing substantial change between July and August. The existence of substantial differences between the July and August wavetrain patterns was also found in Ding and Wang (2005). Although Day et al. (2015) argues that July and August All-Asia EOF1 are highly similar over the Asian monsoon region, this is evidently not true at the global scale.

Finally, we consider the global distribution of temperature and precipitation anomalies associated with All-Asia EOF1 (Figure 4.4). Positive and negative temperature composites were derived from detrended monthly temperature anomalies from BEST, while precipitation composites were obtained from University of Delaware's monthly precipitation record, as described in greater detail in the Methods section. In general, surface temperature increases are inversely correlated with precipitation, presumably because more energy is stored as latent heat in wetter years. Only a few regions outside of South and East Asia show significant anomalies. Most robustly, the Pamir and Tianshan Mountain region, including Tajikistan, Kyrgyzstan and the Taklamakan Desert of western China, moisten and become colder in positive All-Asia EOF1 years. This can be seen in the original figure showing All-Asia EOF1 in Day et al. (2015), and is likely associated with changes in the tropospheric jet shown in Figure 4.9. Robust warming is found over almost all of India, the Arabian Peninsula and the eastern Sahara in positive years, and also to the north over central Siberia, which is the site of a strong atmospheric ridge visible in Figure 4.2. Patterns are generally quite similar to Figures 7 and 9 in Ding and Wang (2005), although ours feature lower amplitude outside of the Asian monsoon.

Recent work finds an associated between high-wavenumber Northern Hemisphere summer standing wave patterns and extreme climate events such as Eurasian heat waves that may have been aggravated in recent decades by global warming (Petoukhov et al., 2013; Schubert et al., 2014). The July composite shows strong warming over Russia, cooling over the United Kingdom, northwestern Europe and southern Scandinavia, and rainfall increase over Scandinavia (Figure 4.4a). However, the general sparsity of significant anomalies and differences between July and August suggest that the phase of All-Asia EOF1 does not translate to a consistent pattern of temperature and precipitation anomalies across Eurasia.

Regional Changes Associated with All-Asia EOF1

Moisture Transport Across the Yunnan Plateau

We examine the regional dynamics within the Asian monsoon that potentially drive All-Asia EOF1-type variability. Furthermore, we can test the hypothesis in Day et al. (2015) that changes in moisture transport across the Yunnan Plateau couple the Himalayan Foothills and Yangtze River Valley and drive All-Asia EOF1. JRA-55 surpasses its predecessors in model resolution and may therefore provide a more credible picture of Asian monsoon dynamics.

We consider the distribution of diabatic heating within the South and East Asian monsoons associated with All-Asia EOF1. The column-integrated heating Q is calculated according to JRA-55 as the residual of the sum of total column upwelling and downwelling short-wave fluxes $\Delta R_S \uparrow$ and $\Delta R_S \downarrow$, upwelling and downwelling long-wave radiative fluxes $\Delta R_L \uparrow$ and $\Delta R_L \downarrow$, sensible heat flux from the surface ΔSH_{sfc} and latent heat flux $\Delta LH = L\dot{P}$, all provided as monthly products in JRA-55:

$$Q = R_{S_{top}\downarrow} - R_{S_{sfc}\downarrow} - R_{L_{sfc}\downarrow} - R_{S_{top}\uparrow} + R_{S_{sfc}\uparrow} - R_{L_{top}\uparrow} + R_{L_{sfc}\uparrow} + SH_{sfc} \uparrow + LP \tag{4.1}$$

L is the latent heat of condensation of water vapor and P precipitation. With our composite analysis, we find massive Q fluxes in the Asian monsoon region associated with our pattern (Figure 4.5). The radiative equilibrium is dominated by latent heat flux, which is an order of magnitude larger than the other terms (their magnitude generally maximizes at 10 W m^{-2}). Significantly, there are no other regions of concentrated Q-fluxes, which suggests that the Asian monsoon region is forcing the CGT in these years.

Figure 4.6 focuses on the Asian monsoon region (10°E-170°W and 5°N-50°N) and only show composite differences that are statistically significant. In both July and August, the Himalayan Foothills and the Yangtze River Valley are a site of diabatic heating, with cooling observed over the Monsoon Zone of India, the Bay of Bengal and the South China Sea (Panels a and b). Almost all anomalies in Q are again driven by anomalous latent heat fluxes. The positive heating anomaly corresponds to a coherent belt of surplus water vapor and anomalous ascent stretching from the Himalayan Foothills and the southeastern Tibetan Plateau eastward to the Yangtze River Valley, and onward to South Korea and Japan (Panels c-e). This same belt is also characterized by low- and mid-level westerly wind anomalies and enhanced eastward moisture transport. The general spatial distribution of anomalies closely matches All-Asia EOF1 in Day et al. (2015). We suggest that changes in the transport of water vapor from the Bay of Bengal supply additional energy as latent heat and drive patterns of diabatic heating.

To substantiate this claim, we separately examine column-integrated moisture transport in each of the positive and negative composites (not shown). In positive composite years, the magnitude of southward water vapor transport northward in southern China reaches 250 kg m^{-1} s^{-1} versus only about 170 kg m^{-1} s^{-1} in negative years. In addition, the eastward moisture transport in positive composite years across the Yunnan Plateau is roughly 100 kg m^{-1} s^{-1}, and near-zero in negative composite years (in fact, low-level winds are slightly easterly across the Yunnan Plateau in August per JRA-55). Therefore, JRA-55 suggests that Bay of Bengal moisture is a major summer source of moisture for the East Asian monsoon, and also highly variable. The magnitude of flux from the Bay of Bengal almost certainly does not contribute all of the latent heat flux anomaly, but may instead serve as a convective trigger leading to further diabatic reinforcement (Sampe and Xie, 2010).

We also look separately at the positive and negative composites for further information on monsoon changes associated with All-Asia EOF1 (Figures 4.7 and 4.8). In positive All-Asia EOF1 years, a tongue of air with high specific humidity stretches eastward from the Yunnan Plateau into the western Pacific (Figure 4.7a). We can also see that low-level convergence and mid-tropospheric ascent are anchored at 30°N. In negative All-Asia EOF1 years monsoonal flow penetrates much further north, reaching about 35°N, northern China becomes more convectively favorable between 35°N and 40°N and the Yangtze River Valley features only weak ascent. Figure 4.8 also appears to show southwest-northeast shifts of the West Pacific subtropical high, reminiscent of Pacific-Japan pattern variability (Kosaka et al., 2011)

Other notable changes occur elsewhere in the Asian monsoon region. The Monsoon Zone of central India features a local maximum in specific humidity in negative All-Asia EOF1 years (Figure 4.7b, about 10 g kg^{-1}) that is absent in positive years. Arid northwestern India is a location of high All-Asia EOF1 amplitude, which can be understood by considering Figures 4.7 and 4.8. In positive All-Asia EOF1 years the northwesterly winds bring hot, extremely dry air from Pakistan to northwestern India, whereas in negative years the region receives a southeasterly source from the Bay of Bengal across the Monsoon Zone. The Arabian Sea is never a source of moisture to northwestern India in spite of its proximity. Northwestern India also varies between near-zero vertical pressure velocity and being convectively favorable in positive and negative years respectively. Finally, in negative All-Asia EOF1 years, the southern Bay of Bengal and parts of southeast Asia become much more favorable to ascent, as well as the windward side of low mountain ranges such as the Ghats and the Philippines coastal range (Figure 4.8). All of the changes described in this paragraph are statistically significant according to Figure 4.6.

Meridional Shift of the East Asian Jet

Over East Asia, Figures 4.9a and b reveal that positive All-Asia EOF1 Julys and Augusts are both marked by a *robust southward shift of the jet* between 50°E-150°E, with significance of hemispheric change exceeding a 99% level. We independently examine jet position in the positive and negative composites for each of July and August (Figures 4.9c-f). In the Asian monsoon region, the climatological position of the jet (with core roughly marked by 30 m s^{-1} and 36 m s^{-1} in Figures 4.9c-f) is strongly influenced by underlying high topography. We expect high orographic barriers such as the Tibetan Plateau to force deviations in overlying circulation by conservation of potential vorticity, wherein the rotation of the earth encourages atmospheric circulation to move as sets of uniform incompressible columns (Holton, 2004b).

The high terrain of the Iranian Plateau upstream from the Tibetan Plateau induces a climatological northward meander in the jet. In positive All-Asia EOF1 years the amplitude of this deviation is small, and the jet returns southward before interacting with the Tibetan Plateau and being forced northward again, with northern apex and maximum velocity over the Taklamakan Desert. The jet then returns southward of 40°N at the longitude of Eastern China. A strong core beginning around South Korea and Japan persists well into the Northern Pacific, past the International Date Line. In negative All-Asia EOF1 years (Panel e), the northward meander around the Iranian Plateau is particularly large, and accompanied by a strong maximum velocity in the vicinity of Kazakhstan and Uzbekistan in excess of 40 m s^{-1}. The jet returns southward over the Tianshan Mountains, but then recurves northward across northeastern China, North Korea and Vladivostok. At some longitudes such as 70°E and 130°E the difference in latitude exceeds 5° (over 500 km).

In summary, the CGT corresponds to a meridional jet shift over East Asia. This shift appears zonally uniform, but a closer inspection reveals that the climatological position of the jet is strongly constrained by regional high topography in both positive and negative All-Asia EOF1 years.

East Asian forcing of the CGT

The forcing of the Circumglobal Teleconnection has been debated in the literature. Ding and Wang (2005) found that the Indian summer monsoon was a major driver of the CGT, while ENSO influence was not significant except through indirect forcing of the Indian summer monsoon. They also found that the North Atlantic jet exit (50°E), a region of high variability in geopotential height and baroclinic instability, can stimulate the CGT by conversion of mean state flow to kinetic energy. Ding and Wang (2007) further investigated the time-lagged propagation of midlatitude disturbances from the North Atlantic and found that they can trigger active and break spells in the Indian monsoon (analogous to negative and positive All-Asia EOF1 respectively), although the actual mechanism of triggering remains unclear. In their view, the diabatic heating from the Indian monsoon strengthens the Central Asian high and a Siberian high that brings anomalous rainfall to North China.

We propose a third component of CGT forcing in addition to the Indian monsoon and North Atlantic: Diabatic heating from the Himalayan Foothills and Yangtze River Valley. In positive All-Asia EOF1 years, widespread cooling over India, the Indian Ocean and southeast Asia predominates, but a coherent band of heating from 90°E to 130°E exists of order 100 W m^{-2}. As previously argued above, this heating results from increased moisture transport from the Bay of Bengal eastward across the Yunnan Plateau to central China, triggering a diabatic feedback and heating from increased latent heat flux. While the area of cooling in India and southeast Asia exceeds the total heating along this pathway, Yangtze River Valley heating predominates in East Asia and appears as a major source on the global level (Figure 4.5). Central China heating may also induce the phenomenon of "phase-locking" in the CGT, wherein the standing wave has preferred configurations. It is known that the winter analog of the CGT has no preferred phase (Branstator, 2002) but its summer component does (Ding and Wang, 2005). We propose that the surplus summer diabatic heating over central China in positive All-Asia EOF1 years creates a trough-and-ridge configuration over the Yangtze River Valley and Siberia to its northwest, which anchors the position of the CGT wavetrain over East Asia. This phase-locking is reinforced by the strong interaction of the East Asian jet with surface topography seen in Figure 4.9 which restricts the East Asian jet to particular configurations. Therefore, we propose that **the geometry of the Tibetan Plateau and Yunnan Plateau lead to the summer phase-locking of the CGT, firstly by steering moisture transport from the Himalayan Foothills to the Yangtze River Valley and inducing diabatic heating, and secondly by topographic deflection of the East Asian jet**.

4.5 East Asian Jet Shifts and the South Flood-North Drought

Overview

In the previous section, we showed that positive and negative All-Asia EOF1 years are reflected as zonally coherent southward and northward shifts of the East Asian Jet extending into the northwestern Pacific Ocean. This relation of East Asian jet latitude and rainfall in July and August leads us to investigate a link between jet position and China rainfall in other seasons using the Rainband Detection Algorithm (RDA) catalog established in Chapter 3.

It is well known that the jet plays a crucial role in the climatology of the Asian monsoon and the transport of storms to East Asia. The onset of the South Asian monsoon corresponds to the passage of the tropospheric jet north of the Tibetan Plateau (Yin, 1949; Yeh et al., 1959; Hahn and Manabe, 1975). The interaction of the jet and Tibetan Plateau produces a standing wave that encourages convergence and ascent downstream over China and the Western Pacific during Meiyu Season (Yang et al., 2002; Molnar et al., 2010; Chen and Bordoni, 2014). The jet also serves as a waveguide for storms propagating from the Eurasian interior via the "Silk Road" teleconnection (Kosaka et al., 2012), a regional manifestation of the Circumglobal Teleconnection (Hoskins and Ambrizzi, 1993; Ambrizzi and Hoskins, 1997; Park and Schubert, 1997). There is also evidence connecting shifts in the East Asian jet with anomalous rainfall over China on an interannual time scale (Liang and Wang, 1998; Du et al., 2009; Li and Zhang, 2014), and with the South Flood-North Drought pattern of decadal change in China (Yu et al., 2004; Yu and Zhou, 2007; Xuan et al., 2011).

It has previously been argued that decadal change in the East Asian jet is strictly a local response to altered heating in the East Asian monsoon (Yu and Zhou, 2007). However, the tropospheric jet shifts with meridional shifts of the Hadley Cell (Kang and Polvani, 2011), which are in turn forced by changes in interhemispheric heating gradient (Chiang and Friedman, 2012; Donohoe et al., 2013; Schneider et al., 2014). Therefore, it is reasonable to suggest that the East Asian jet may have respond to twentieth-century external climate forcing on a global scale and translate it into regional impact. We do not suggest that the jet does not exclusively control the position of rainbands in China, but rather that a mutual feedback may exist between jet position and Meiyu rainfall. Such a feedback might also help with improving projections of changes in the twenty-first-century East Asian monsoon.

Previously in Chapter 3, we used the RDA catalog to break the South Flood-North Drought down into changes in frequency, latitude and intensity during particular Meiyu stages. The most important contributors to decadal change were a decline in the frequency of fronts in May (the Pre-Meiyu), and a southward shift in rainband latitude during July-August (the Post-Meiyu). We now test whether decadal jet changes have also occurred during these stages, and more generally whether interannual changes in rainfall properties and changes in jet position are correlated.

Climatology of the East Asian Jet

The East Asian jet assumes a different configuration during each of the five rainfall stages of East Asian monsoon rainfall described in Chapter 3. A full monthly jet climatology is presented in Schiemann et al. (2009). Beginning in May, the East Asian jet moves from its winter position on the southern flank of the Tibetan Plateau to a summer latitude well north of the plateau. During this transition, the jet occupies intermediate configurations that correspond to different stages of China rainfall (Figure 4.10). Peak rainfall rates in China from May to mid-July corresponds to the months when the climatological latitude of the jet impinges on the Tibetan Plateau, because the interaction of the tropospheric jet and Tibetan Plateau strengthens convergence and rainfall downstream over China and the western Pacific Ocean (Molnar et al., 2010; Sampe and Xie, 2010; Chen and Bordoni, 2014). From May to September, the climatological latitude of rainfall, rainbands and jet density are all closely coupled, with peak jet density occurring 5 to 10 degrees north of the latitude of peak rainfall, as is expected in theory in a region of strong fronts (Holton, 2004a).

Focusing on individual stages, we can see that the Pre-Meiyu period corresponds to the beginning of the jet's northward transit from its winter configuration. During Meiyu season, the preferred latitude of the jet continues to shift northward. The period of frequent double rainband occurrence during the Post-Meiyu occurs during the jet's maximal northward extent. Finally, the jet returns southward during the Fall Rains in October and November, which produces only a weak rainfall response. Thus, the East Asian monsoon is marked by a seasonal asymmetry between the jet's northward and southward passage, the former featuring strong rainfall and the latter much weaker amounts. Figures 4.10a-e show mean rainfall, jet frequency and rainband position during each stage, as well as their zonal average (sidebars). From the Pre-Meiyu to Post-Meiyu, each northward jump in peak rainband frequency corresponds to a similar shift in jet count density.

Jet Changes, 1980-2001 Versus 1958-1979

In Figure 4.13a, we show the zonal average over $90 - 130°$E) of mean jet latitude, averaged over the years 1958-1979 (blue solid line) and 1980-2001 (dashed red line) with 95% confidence intervals overlain. In Chapter 3, we found that changes in rainband properties were concentrated during the pre-Meiyu (May) and post-Meiyu (July-August). Changes in the jet are found during both of these time periods. During the Pre-Meiyu (May), the tropospheric jet is shifted southward by almost 2° in 1980-2001 relative to 1958-1979, when its mean latitude was $\approx 41°$N. We estimate the significance of this change using a two-tailed Kolmogorov-Smirnov (K-S) test. Since the K-S test requires that all samples are independent, we first remove temporal autocorrelation due to synoptic variability by assimilating daily mean jet latitude into 4 day blocks (Figure **??**. A subsequent K-S test finds that the shift is significant at a 99% confidence level with $p = 0.003998$. During the Post-Meiyu (days 201-273), when a southward shift in rainband latitude is found in 1980-2001 relative to 1958-1979, the mean latitude of the jet is also consistently displaced southward. We assimilate daily mean jet latitude into 7-day blocks before performing a K-S test, and find a p-value of this shift of $p = 0.05667$, which is not statistically significant.

Figure 4.12 overlays changes in jet kernel density over observed rainfall changes from APHRODITE during the Pre-Meiyu and the Post-Meiyu. Rainfall changes shown are for 1980-2001 versus 1958-1979 to match the length of the Schiemann database. Significant regions of yearly rainfall change are concentrated around 30°N (increase) and 37°N, mostly agreeing with Figure 3.1. During the Pre-Meiyu (Panel b), the principal change is a decrease in jet counts around 30°N, where rainfall and rainband frequency have also decreased significantly. During the Post-Meiyu (Panel c), we observe increased rainband probability around 28°N and decreased rainfall and rainband frequency around 36°N. Jet kernel density changes follow the same southward shift but with a 5° offset northward. The Post-Meiyu changes show a coherent set of changes in rainband, rainfall and jet position, while the Pre-Meiyu jet changes are more difficult to interpret directly.

4.6 Hypothesis

A significant southward shift in the East Asian jet occurred during the Pre-Meiyu season between 1958-1979 and 1980-2001, as well as a weaker southward shift during the Post-

Meiyu that was not statistically significant. In Chapter 3, we previously found a significant decrease in rainband frequency during the Pre-Meiyu, and a southward shift in rainband latitude during the Post-Meiyu. Here we suggest that both of these phenomena may have been caused by a southward shift in the seasonal cycle of the East Asian jet. Climatologically, rainfall surges during the Pre-Meiyu, which is also when the jet begins its northward transit and first impinges on the Tibetan Plateau. We propose that the date when the jet starts shifting northward has occurred later, thereby delaying the onset of the Pre-Meiyu and leading to a decrease in rainbands and rainfall. Subsequently, because the jet's northward progression has started later, its maximal poleward latitude is also further south, therefore decreasing rainfall in northern China and increasing rainfall in central China, and producing a South Flood-North Drought response. A similar argument was presented in Chiang et al. (2015) (the "Jet Transition Hypothesis") as a template for the effect of orbital forcing on the East Asian paleomonsoon.

To test our hypothesis, we investigate the correlation of interannual anomalies in jet latitude to those of rainband properties during the Pre-Meiyu and Post-Meiyu. If interannual anomalies in jet latitude manifest as Pre-Meiyu changes in rainband frequency or Post-Meiyu changes in rainband latitude, our argument about the effect of interdecadal change in the East Asian jet becomes more plausible. Figure 4.13b shows a scatter plot of rainband *frequency* anomalies versus jet latitude anomalies in May (days 121-150). Most years with a decrease in rainband frequency feature a southward jet shift, and vice-versa, and such years occur mostly during 1980-2007. A similar relation is found between monthly anomalies in rainband *latitude* and jet latitude during July-August (days 201-260, Figure 4.13c). In the latter figure, we exclude rainbands south of 28°N from calculated anomalies, since such rainbands reflect South China Sea storms, rather than jet influence (Day et al., 2015). Together, Figures 4.13b and 4.13c suggest that interannual changes in jet latitude affect Pre-Meiyu rainband frequency and Post-Meiyu rainband latitude.

In summary, we propose that the delayed passage of the jet to the north of the Tibetan Plateau has delayed the onset of the Pre-Meiyu season, which has decreased May rainfall in central China, and restricted the northward advance of precipitation, thereby reducing Post-Meiyu rainfall in northern China.

4.7 Conclusion

The existence of a Circumglobal Teleconnection in Northern Hemisphere summer was demonstrated in models and observation in the past decade and a half. Two potential drivers of the CGT have previously been proposed: The Indian monsoon, where anomalies are baroclinic rather than barotropic and massive diabatic heating occurs, and baroclinicity in the Atlantic jet exit region, where geopotential height variability is particularly high. We propose a third source of CGT variability: Diabatic heating along the Himalayan Foothills and Yangtze River Valley of up to 100 Wm^{-2} which produces a diagonally tilted trough-ridge pattern over China and Siberia. This characteristic dipole of geopotential height anomalies may encourage the phase-locking of the CGT in summer, further strengthened by the deflection of the jet by high topography across the Asian monsoon region. The magnitude of East Asian forcing does not necessarily overshadow the influence of the Indian monsoon and North Atlantic, but rather may complement it in strong All-Asia EOF1 years.

We have shown that a significant amount of the annual and decadal variability in Meiyu front activity is accompanied by changes in the westerly jet. Both the Pre-Meiyu (May) and Post-Meiyu (July-August) seasons, during which the largest rainfall and rainband changes have occurred, feature a southward anomaly in mean jet latitude during 1980-2007 relative to 1951-1979. We argue that the previously discovered decline in Pre-Meiyu rainband frequency and southward shift in rainbands during the Post-Meiyu are both caused by an overall southward shift of the summer progression of the East Asian tropospheric jet, delaying Pre-Meiyu onset and restricting the northward range of banded rainfall. This interpretation is a modern analog of the Jet Transition Hypothesis described in Chiang et al. (2015), wherein East Asian rainfall changes on paleoclimate timescales are ascribed to modulation in the seasonal cycle of the tropospheric jet.

Composite analysis with JRA-55 also supports our chief hypothesis in Chapter 2, that changes in moisture transport across the southeastern Tibetan Plateau and Yunnan Plateau drive All-Asia EOF1 rainfall variability. According to our composite analysis, the source of Yangtze River moisture in July-August can vary from receiving a sizable Bay of Bengal component (up to 100 kg m^{-1} s^{-1}) to being entirely sourced from the South China Sea. This claim can likely be tested with present-day records of precipitation isotopes. Since the transport distance from the Bay of Bengal to the Yangtze River is long, we would expect water arriving in central China from the west to be highly depleted, and therefore that positive All-Asia EOF1 years should see negative excursions in Yangtze River δ^{18}O records. This is also a region where many speleothems are located, cave stalagmites featuring tends of thousands of years of continuous deposition from which a continuous time series of δ^{18}O can be extracted. Traditionally, speleothem δ^{18}O records are viewed as proxies of local monsoon intensity. However, recent work increasingly argues that East Asian speleothem records such as Hulu and Sanbao are primarily a record of changes in the Indian monsoon upstream that are then transported downwind (Pausata et al., 2011; Cai et al., 2015; Baker et al., 2015). Proving that changes in water vapor transport from the Bay of Bengal alter the *present-day* isotopic signature in central China would strengthen the new school of interpretation of East Asian speleothems.

In this chapter, we have shown a robust connection between Asian monsoon rainfall variability and two components of Northern Hemisphere summer climate, the Circumglobal Teleconnection and the tropospheric jet. In the case of the jet, we have shown that both interannual and decadal fluctuations in late-twentieth-century East Asian rainfall were also marked by a jet signal. The ultimate cause of the South Flood-North Drought remains unclear. Authors have suggested changes in Indian Ocean SST (Qu and Huang, 2012), decreased sensible heating from the Tibetan Plateau (Liu et al., 2012; Hu and Duan, 2015) and aerosol forcing (Song et al., 2014). We do not discuss the origin of the forcing here, but rather show that late-twentieth century change is consistently manifested across different climate elements. In particular, we open the possibility of using predictions about the tropospheric jet and the CGT under twenty-first-century global warming to improve projections of the future Asian monsoon. It is important to note that midlatitude forcing via the Silk Road teleconnection is intrinsically chaotic (Kosaka et al., 2012). Nonetheless, Lee et al. (2014) analyzed 21$^{\text{st}}$-century changes in a suite of CMIP5 models and concluded that the robust stabilization of the atmosphere in almost all models would tend to decrease the variability associated with the CGT.

For the tropospheric jet, observations show that the global annual mean latitude of the tropospheric jet has shifted poleward in tandem with the expansion of the Hadley circulation under global warming (Fu et al., 2006; Archer and Caldeira, 2008; Fu and Lin, 2011), and will continue to do so in future (Lu et al., 2007; Kang and Lu, 2012). However, the East Asian portion of the jet has shifted equatorward as found in our study and others (Yu and Zhou, 2007; Archer and Caldeira, 2008; Park and An, 2014b), and recent work proposes that the southward trend will continue (Park and An, 2014a). Liu and Chiang (2012) has already shown that transient forcing from the North Atlantic may have induced a response in the East Asian monsoon by shifting the pattern of westerlies. Based on the observed strong connections between the Circumglobal Teleconnection, East Asian Jet and Asian monsoon rainfall, we hope to use our growing knowledge of future behavior of other atmospheric components to improve the skill of projections of the twenty-first-century East Asian monsoon.

4.8 Acknowledgments

Significant portions of the current work were produced in collaboration with Jacob Edman and John Chiang and under the guidance of Inez Fung. Computer code was written in MATLAB and Ferret. The formula for column-integrated heating was retrieved from the JRA-55 climatological atlas at `http://ds.data.jma.go.jp/gmd/jra/atlas/en/D_HEATcol.html`. University of Delaware precipitation is freely downloadable at `http://climate.geog.udel.edu/~climate/html_pages/download.html`. The UCAR Climate Data guide was used on several occasions to help select appropriate data products.

4.9 Tables and Figures

Table 4.1: Years used for the positive and negative composities of All-Asia EOF1 in July (July AA+ and AA-) and August (August AA+ and August AA-), expressed in units of standard deviation. Years are chosen as the most extreme values of All-Asia EOF1 as previously published in Day et al. (2015).

All-Asia EOF1 Composites		Years	Value (Std. Devs.)
July	+	1970, 1987, 1998, 2002, 2007	1.65, 2.25, 1.47, 1.35, 1.62
	-	1959, 1973, 1976, 1978, 1994	-1.59, -1.25, -1.45, -1.40, -2.65
August	+	1958, 1965, 1993, 1998, 2005	1.85, 1.77, 2.00, 2.67, 1.49
	-	1973, 1978, 1984, 1994, 2006	-1.96, -2.04, -1.68, -1.64, -1.40

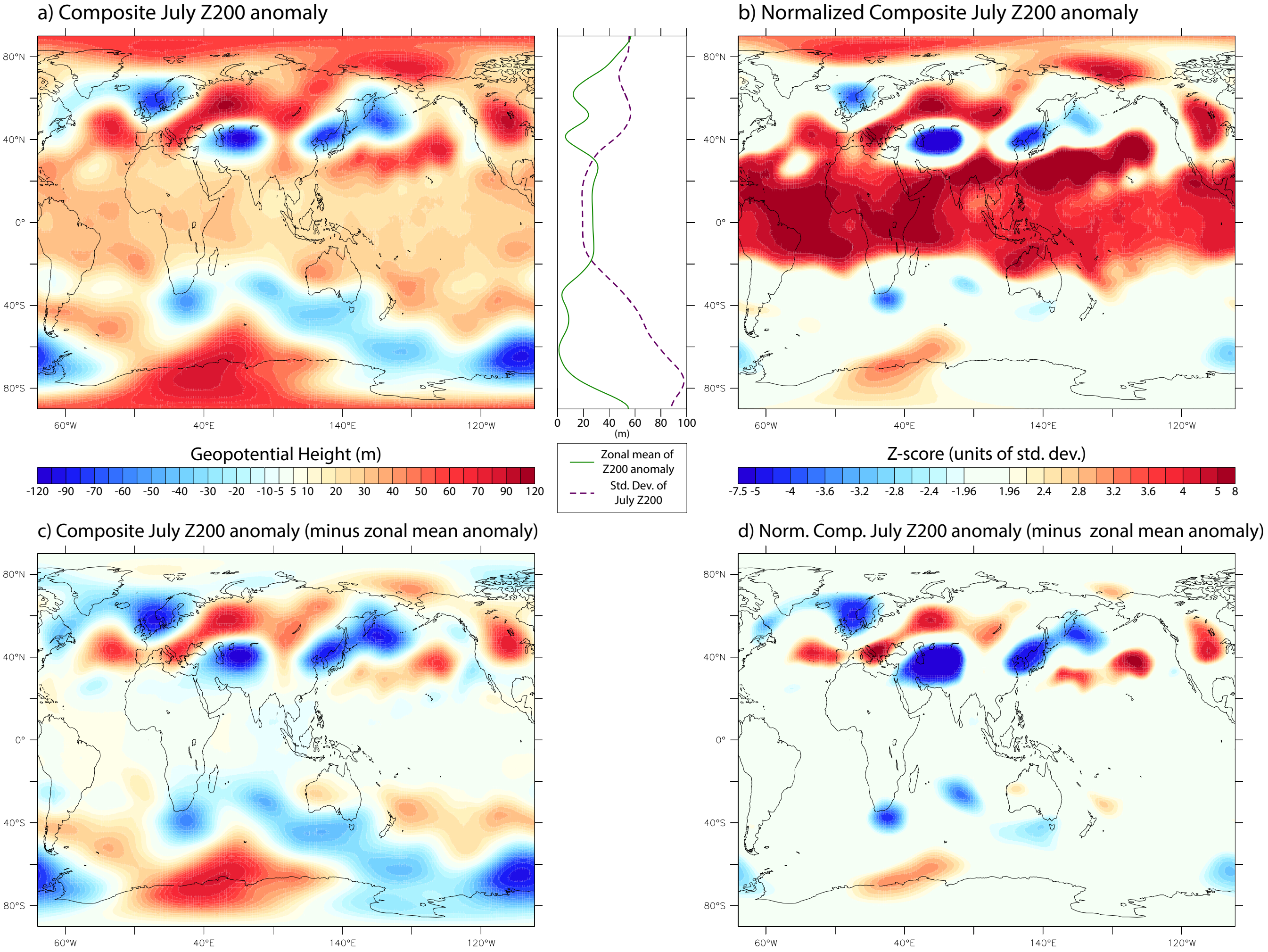

Figure 4.1: a) July composite difference in 200-mb level geopotential height (Z200) between positive and negative All-Asia EOF1 years. Sidebar: Zonal mean of composite anomaly. b) July Z200 composite anomaly expressed as Z-score (units of local std. devs.), showing massive anomaly in the Tropics. c) July Z200 composite anomaly with zonal mean removed, highlighting mid-latitude wavetrain. d) Same as Panel c, but expressed as Z-score as in panel b.

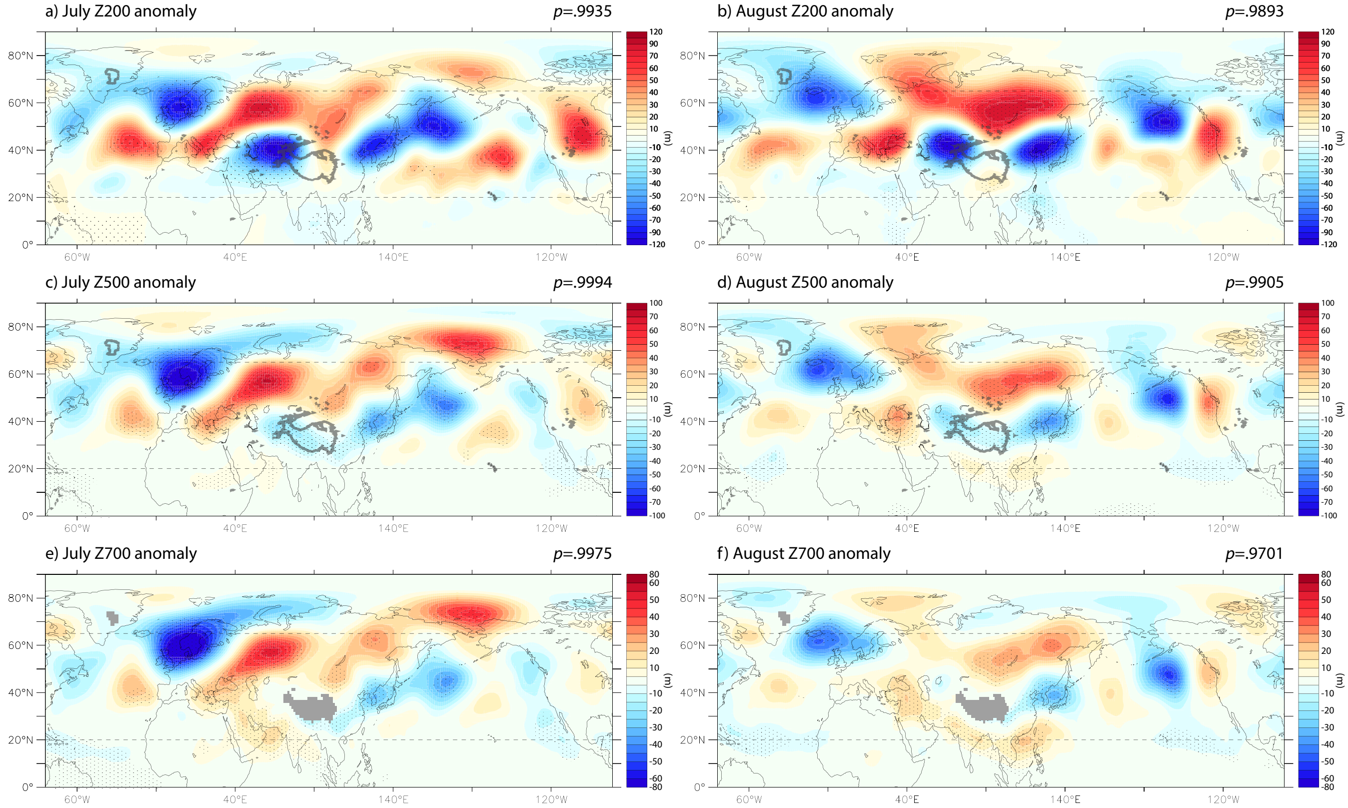

Figure 4.2: July All-Asia EOF1 composite difference in a) Z200, c) Z500 and e) Z700. Panels b, d and f are analogous to panels a, c and e except with procedure repeated for August. Local statistically significant differences at a 95% level are marked by stippling. p-values at the top-right of each plot show the likelihood via Montecarlo testing that the *amount of statistically significant area* between 20°N and 65°N (delimited on figures) could be achieved at random (given by $1 - p$). A value above .95 indicates statistical significance at a 95% confidence level.

a) Inter-composite July V200 anomaly *p*=.9792

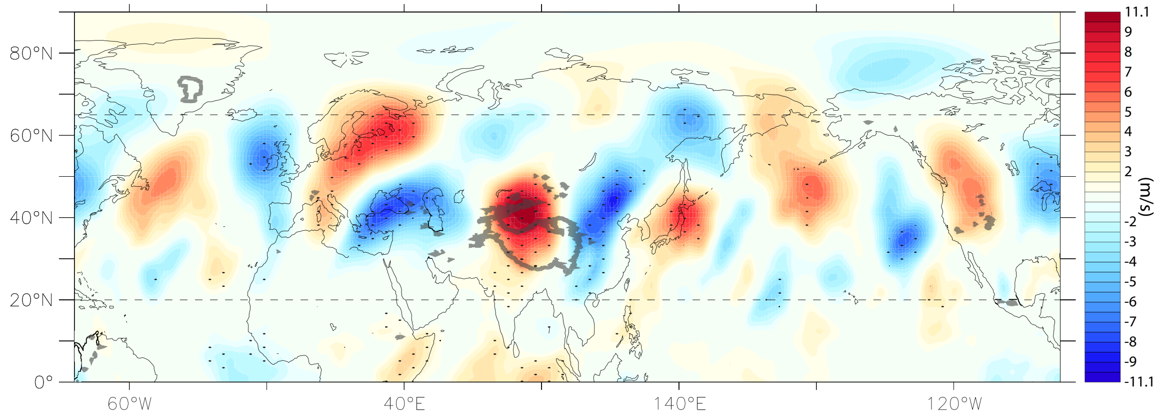

b) Inter-composite August V200 anomaly *p*=.9747

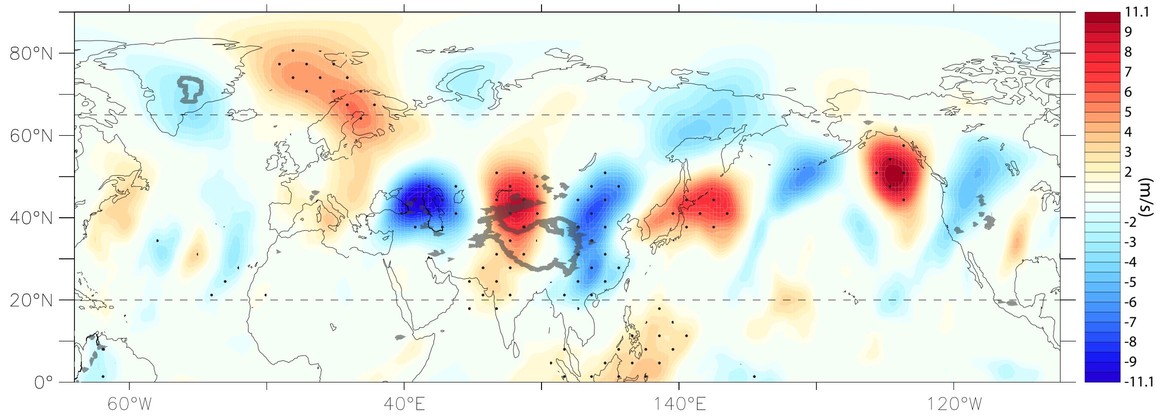

Figure 4.3: Composite anomalies in 200-mb meridional wind (V200) in a) July and b) August, both of which show a robust global mid-latitude standing wave. As explained in Figure 4.2 and in main text, *p*-values shown at top-right indicate statistical significance of entire pattern between 20°N and 65°N.

a) July Composite Temperature Anomaly (95% significant only)

b) August Composite Temperature Anomaly (95% significant only)

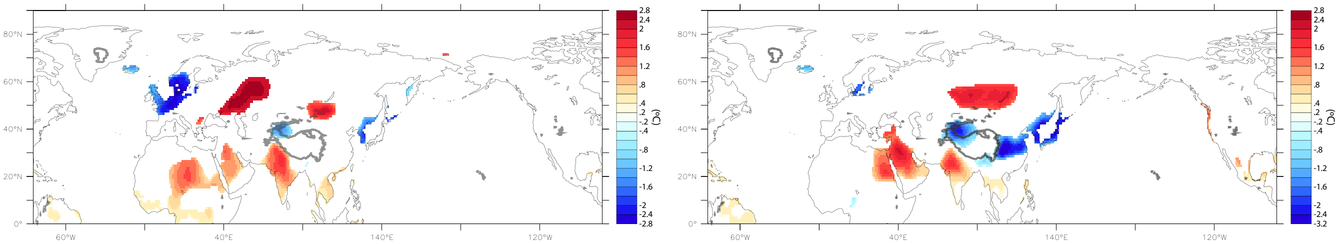

c) July Composite Precipitation Anomaly (95% significant only)

d) August Composite Precipitation Anomaly (95% significant only)

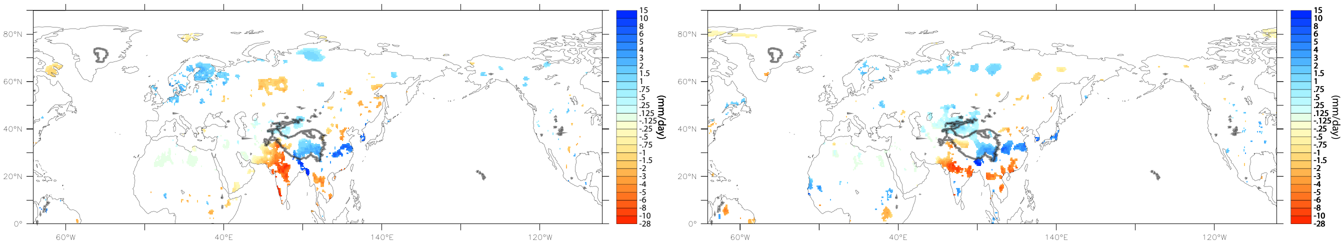

Figure 4.4: July and August inter-composite anomalies in BEST surface temperature and UDEL precipitation assimilated from weather station data. Panels a and b - temperature anomalies in K for a) July and b) August. Panels c and d - same as for panels a and c, but for precipitation. Only anomalies significant at a 95% level according to Montecarlo testing are displayed.

a) July Composite Difference of norm. Z200 anomaly-norm. Z700 anomaly

b) August Composite Difference of norm. Z200 anomaly-norm. Z700 anomaly

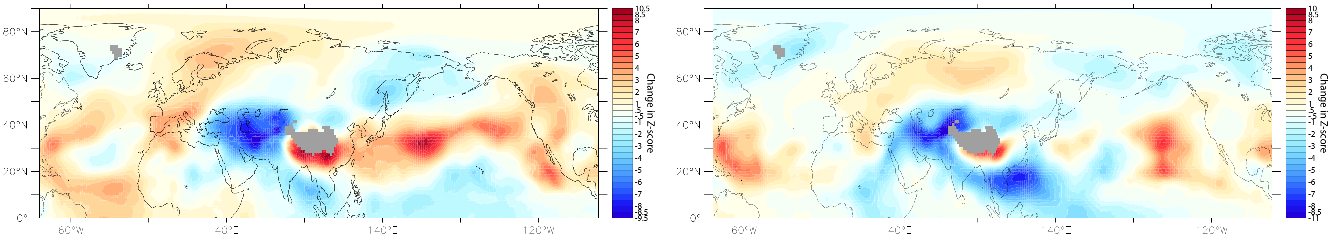

c) July Inter-composite Column Diabatic Heating anomaly (***Q***)

d) August Inter-composite Column Diabatic Heating anomaly (***Q***)

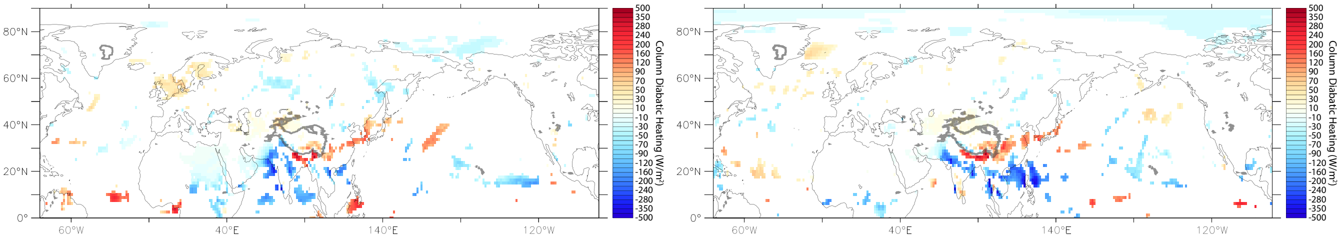

Figure 4.5: Dynamics of the CGT across the Northern Hemisphere. a-b: Change in Z-score of geopotential height between 200-mb and 700-mb levels, revealing whether upper-tropospheric wavelike disturbances are barotropic and baroclinic. The CGT consists mostly of barotropic disturbances except for a baroclinic region over northern India and Pakistan. c-d: Column diabatic heating Q for c) July and d) August, computed as residual from top-of-atmosphere and surface radiative flux terms. A coherent pattern of strong warming and cooling occurs over the Asian monsoon in a pattern resembling All-Asia EOF1.

a) July Column-Integrated Diabatic Heating **Q** (95% significant only)

c) August Column-Integrated Diabatic Heating **Q** (95% significant only)

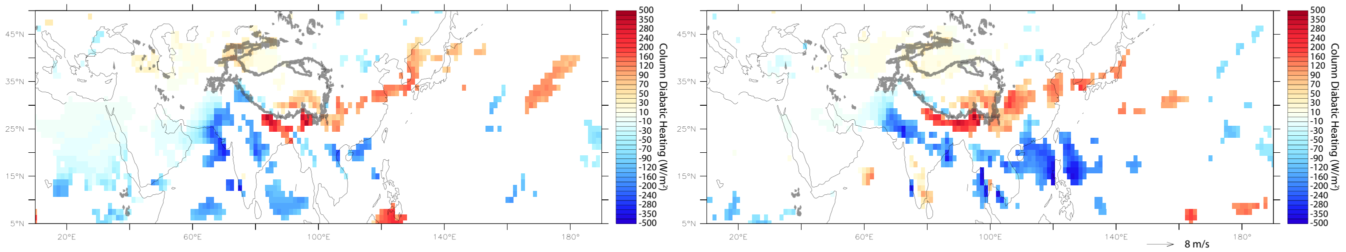

c) July Composite Diff. in e_{700} with u_{700}-v_{700} anomaly vectors (95% significant only)

d) July Composite Diff. in ω_{500} with u_{500}-v_{500} anomaly vectors (95% significant only)

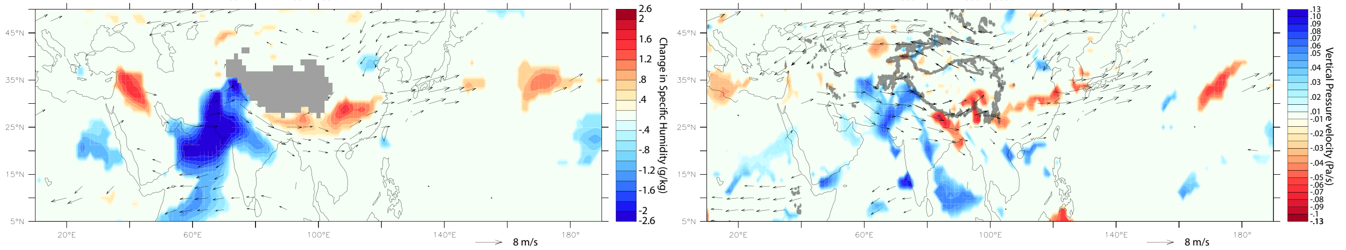

e) July Comp. Diff. in Precipitable Water and column-integrated *qu-qv* anomaly (95% only)

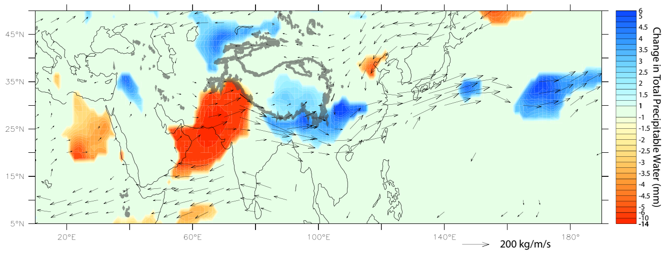

Figure 4.6: Statistically significant inter-composite differences in dynamics according to JRA-55. Top row: Column diabatic heating Q for a) July and b) August, computed as residual from top-of-atmosphere and surface radiative flux terms; c) 700-mb level specific humidity (e_{700}, shading) with 700-mb level winds overlain (vectors); d) 500-mb level vertical pressure velocity (ω_{500}, shading) with 500-mb level winds overlain (vectors); e) Total column precipitable water content (shading) with column-integrated water vapor transport overlain (vectors). Only anomalies that are statistically significant at a 95% confidence level are shown in this series of plots.

a) July e_{700} with u_{700}-v_{700} overlain, Positive Composite

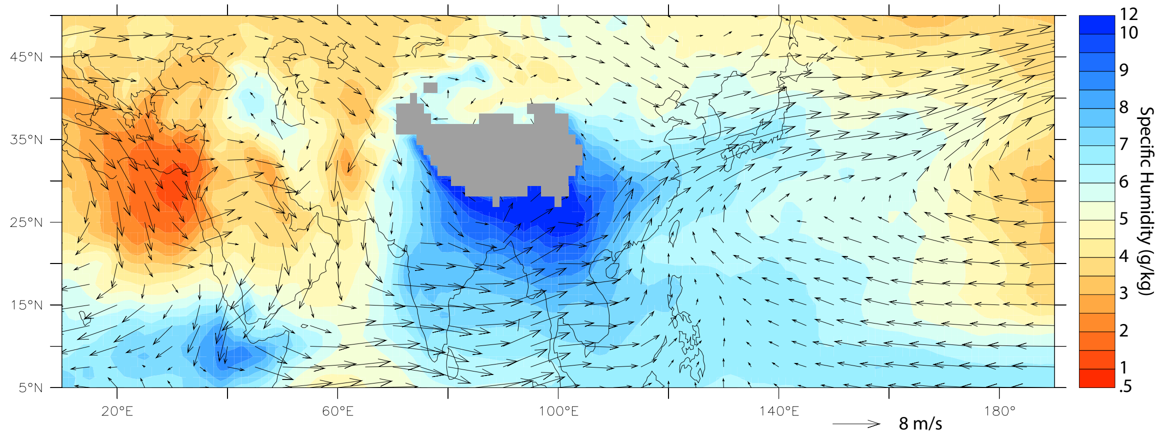

b) July e_{700} with u_{700}-v_{700} overlain, Negative Composite

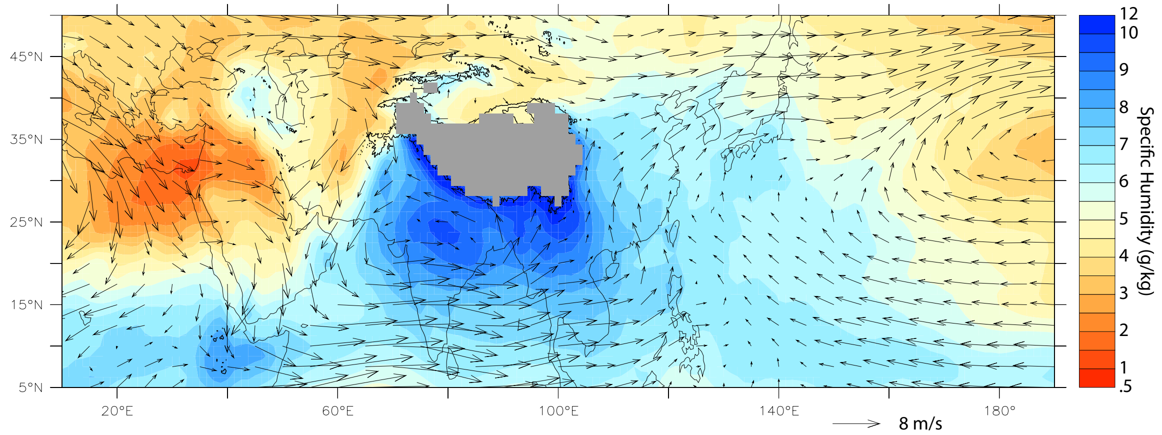

Figure 4.7: JRA-55 700-mb specific humidity (e_{700}) with 700-mb level winds superimposed in a) a composite of positive All-Asia EOF1 years and b) for the negative All-Asia EOF1 composite. Since the scale height of water vapor is only about 3 km, we expect 700-mb winds to roughly match the direction of column-integrated moisture transport $qu - qv$.

a) July ω_{500} with u_{500}-v_{500} overlain, Positive Composite

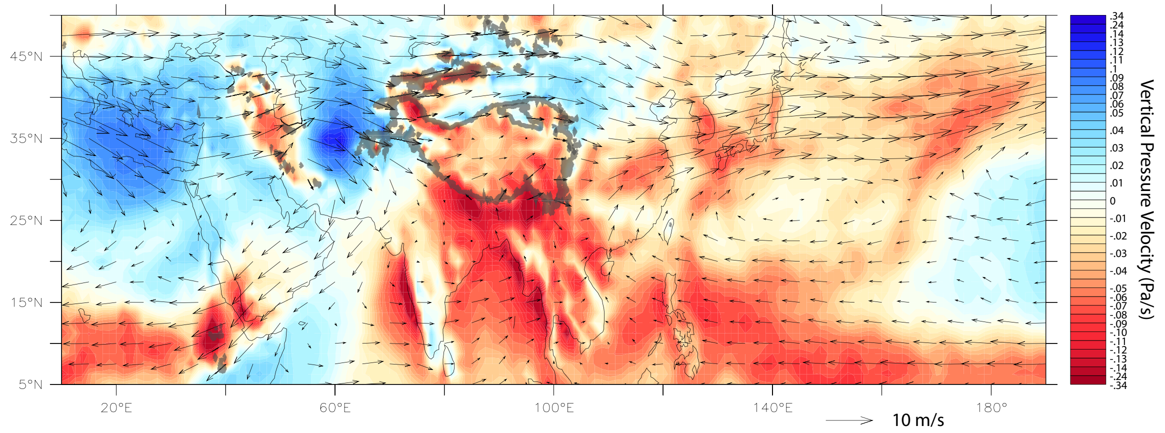

b) July ω_{500} with u_{500}-v_{500} overlain, Negative Composite

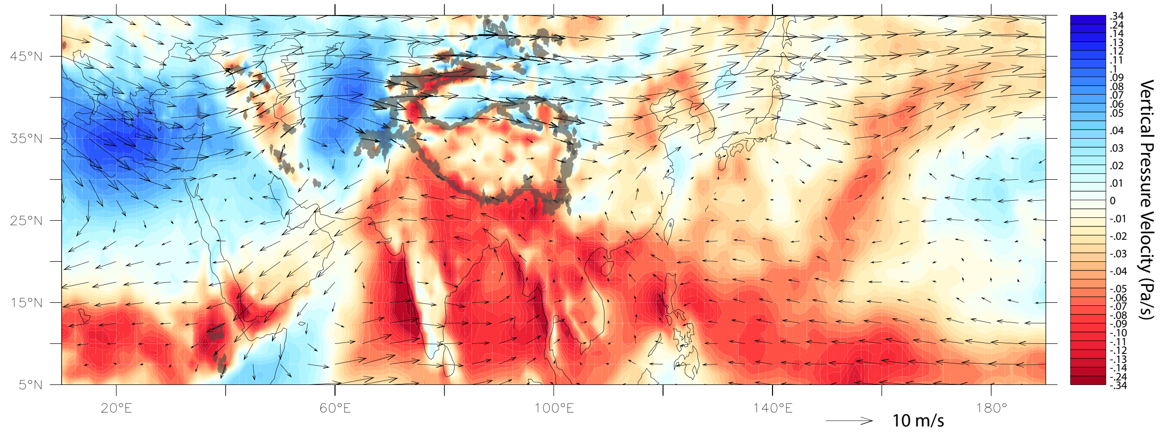

Figure 4.8: JRA-55 500-mb vertical pressure velocity ω_{500} (units of Pa/s, opposite sign from vertical velocity w) with 500-mb level winds superimposed for a) positive All-Asia EOF1 composite and b) negative All-Asia EOF1 composite.

a) Inter-composite July U200 difference *p*=.9981

b) Inter-composite August U200 difference *p*=.9957

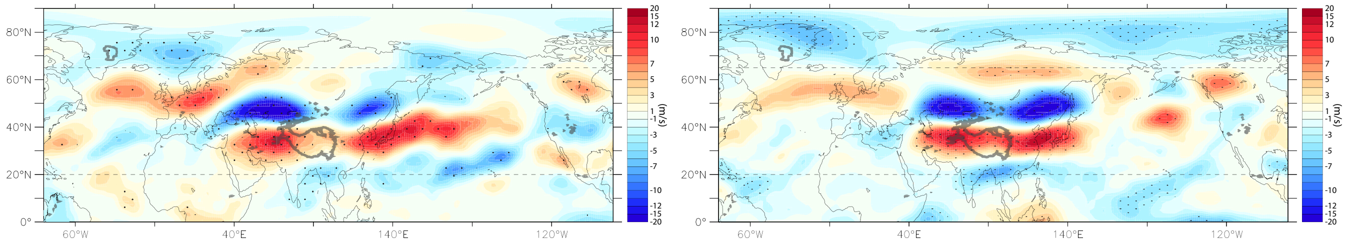

c) July U200 anomaly, Positive Composite

d) August U200 anomaly, Positive Composite

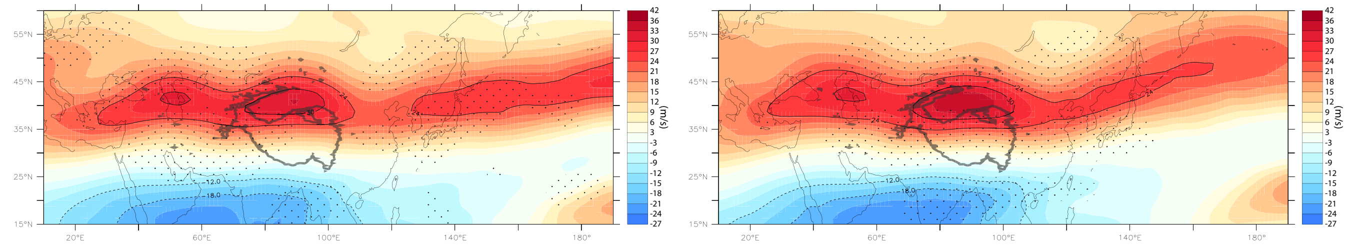

e) July U200 anomaly, Negative Composite

f) August U200 anomaly, Negative Composite

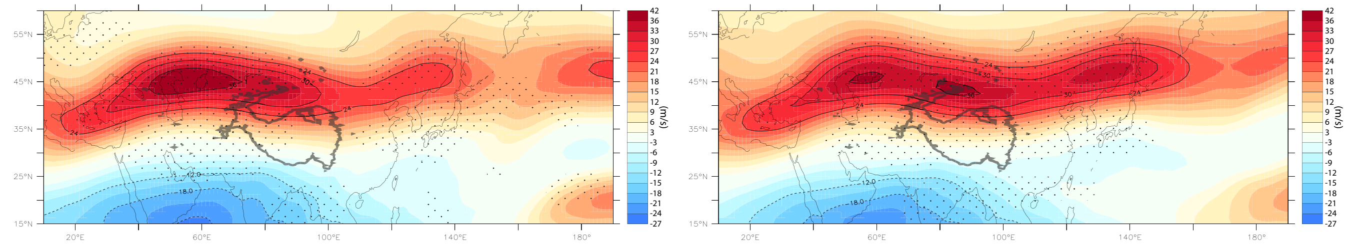

Figure 4.9: All-Asia EOF1 composite difference in JRA-55 200-mb level zonal wind (U200) for a) July and b) August. Regions of change between positive and negative All-Asia EOF1 composites that are significant at a 95% confidence level are marked by stippling. The composite difference is marked by a southward shift of the East Asian Jet in positive All-Asia EOF1 years, and vice-versa in negative years. The overall pattern of change is significant at a 99% confidence level. c) and d): JRA-55 fields of U200 in positive All-Asia EOF1 composite years for July and August respectively. e) and f): Same as Panels c and d, but for Negative All-Asia EOF1 composite years.

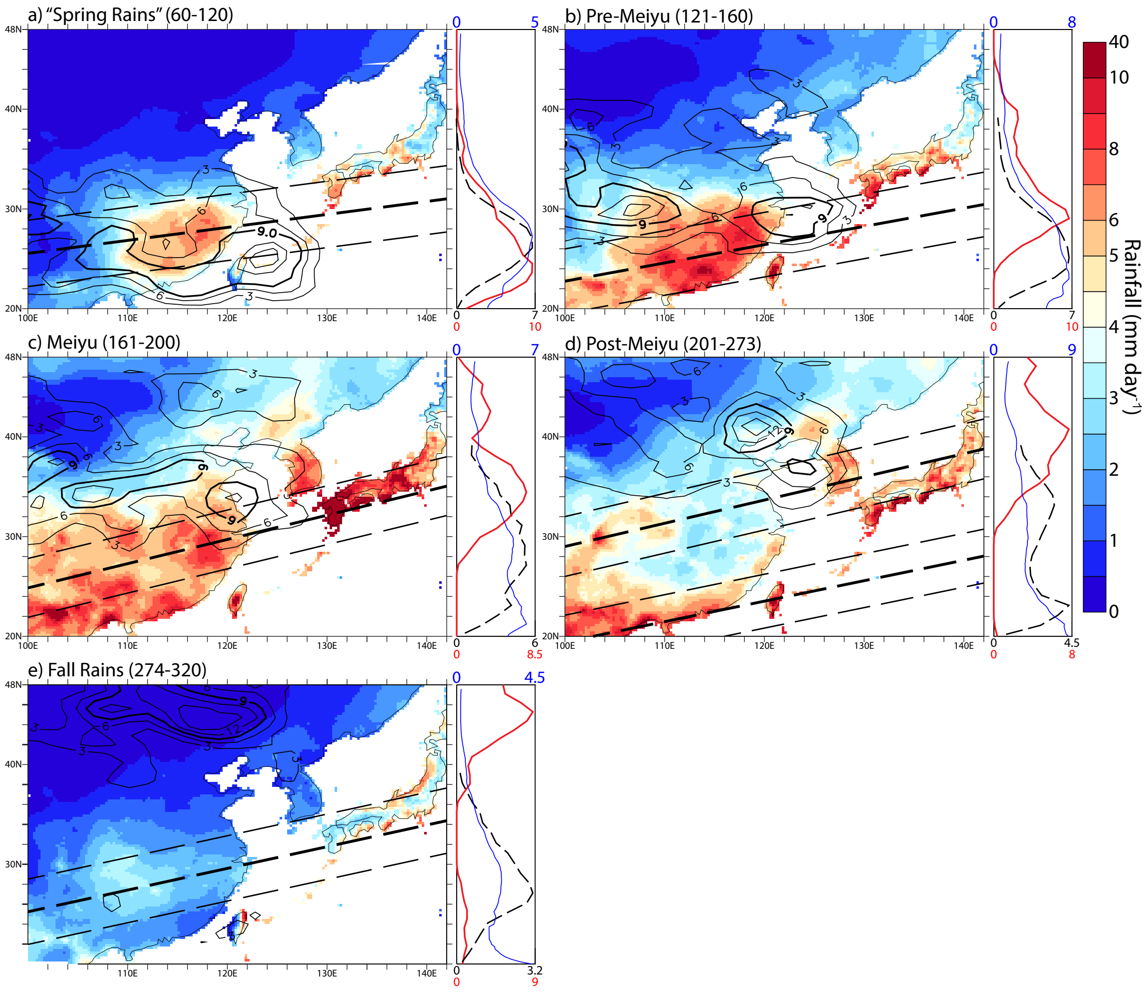

Figure 4.10: Climatology of East Asian rainfall stages showing rainfall (shading), jet kernel density (contours of probability density in units of 10^{-4}) and most common rainband position during that stage. Sidebars shows, for each time period, the longitude average over 105-123°E of rainfall (thin blue line, units of mm day^{-1}), jet kernel density (red line, units of 10^{-4}) and rainband position (dashed black line, absolute probability in %, 1-degree latitude smoothing). From the Pre-Meiyu to Post-Meiyu, a peak in preferred jet latitude consistently occurs 5 degrees north of a corresponding maximum in rainband frequency.

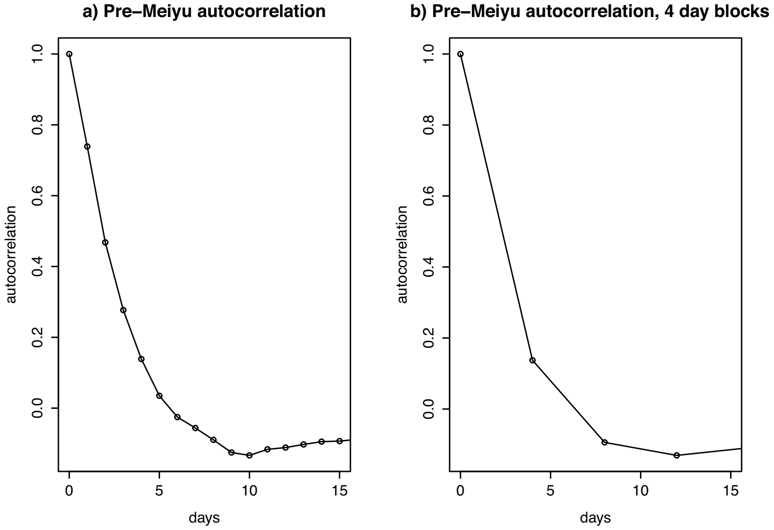

a) Pre–Meiyu autocorrelation **b) Pre–Meiyu autocorrelation, 4 day blocks**

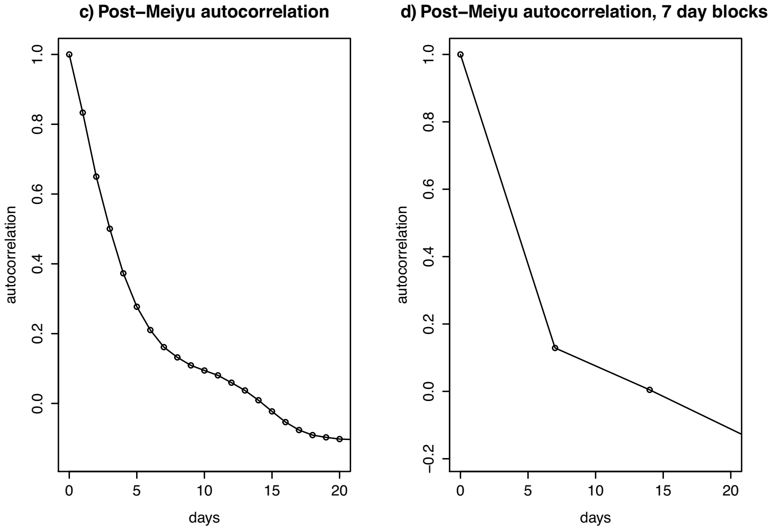

c) Post–Meiyu autocorrelation **d) Post–Meiyu autocorrelation, 7 day blocks**

Figure 4.11: The accumulation of the jet into blocks eliminates the autocorrelation from the daily mean latitude signal. During the Pre-Meiyu, mean daily jet latitude is further smoothed over 4 days (panels a and b); During the Post-Meiyu, we average over 7 days (panels c and d).

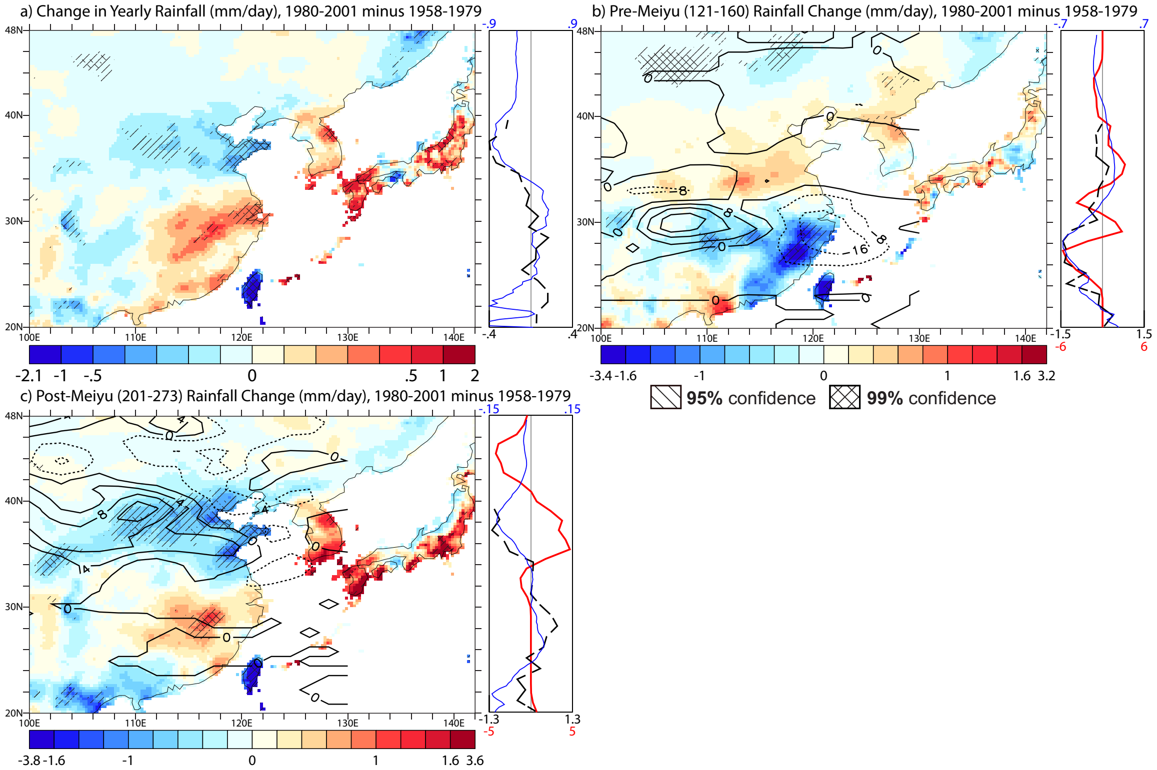

Figure 4.12: a) Whole year mean rainfall change for 1980-2001 versus 1958-1979, showing the South Flood-North Drought pattern; b) Rainfall changes during the Pre-Meiyu (days 121-160) with contours of jet density change overlain; c) Same as c, but for the Post-Meiyu (days 201-273). Statistical significance at 95%/99% level overlain with single/double hatches. Sidebars show, for each time period, the longitude average over 105-123°E of changes in rainfall (thin blue line, units of mm day^{-1}), jet kernel density (red line, units of 10^{-4}) and rainband position (dashed black line, absolute probability in %, 1-degree latitude smoothing).

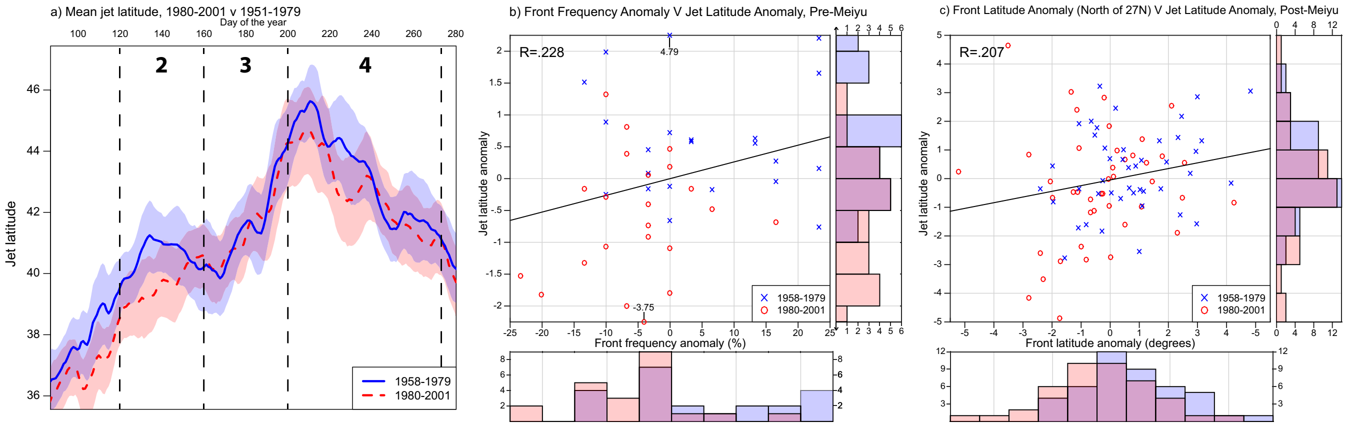

Figure 4.13: a) 7-day running mean latitude of the westerly jet in the region 90-130°E for the years 1958-1979 (blue, solid) and 1980-2001 (red, dashed). Bootstrapped 95% confidence intervals are shaded. Time periods: 2 - Pre-Meiyu; 3 - Meiyu; 4 - Post-Meiyu; b) Plot of monthly anomalies in rainband frequency versus monthly anomalies in jet latitude during days 121-150 (May) for 1958-1979 (blue X) versus 1980-2001 (red circle); c) Same as b), but showing 30-day anomalies of rainband latitudes during the Post-Meiyu (201-230 and 231-260, each set of 30 days treated as a separate point). Histograms of anomalies are also shown on the side of each figure.

Bibliography

Aksoy, Hafzullah (2000). "Use of Gamma Distribution in Hydrological Analysis". *Turkish J. Eng. Environ. Sci.*, **24**, 419–428.

Allen, Myles R. and William J. Ingram (2002). "Constraints on future changes in climate and the hydrologic cycle." *Nature*, **419**, 224–232. doi: 10.1038/nature01092.

Ambrizzi, Tércio and Brian J. Hoskins (1997). "Stationary Rossby-wave propagation in a baroclinic atmosphere". *Q. J. R. Meteorol. Soc.*, **123**, 919–928.

Annamalai, H, Jan Hafner, K P Sooraj, and P Pillai (2013). "Global Warming Shifts the Monsoon Circulation, Drying South Asia". *J. Climate*, **26**, 2701–2718. doi: 10.1175/JCLI-D-12-00208.1.

Annamalai, H and JM Slingo (2001). "Active/break cycles: Diagnosis of the intraseasonal variability of the Asian summer monsoon". *Clim. Dyn.*, **18**, 85–102.

Anttila-Hughes, Jesse K and Solomon M. Hsiang (2013). *Destruction, Disinvestment, and Death: Economic and Human Losses Following Environmental Disaster*. Working paper available at http://dx.doi.org/10.2139/ssrn.2220501. 2013.

Archer, Cristina L. and Ken Caldeira (2008). "Historical trends in the jet streams". *Geophys. Res. Lett.*, **35**, L08803. doi: 10.1029/2008GL033614.

Auffhammer, Maximilian, V. Ramanathan, and Jeffrey R. Vincent (2012). "Climate change, the monsoon, and rice yield in India". *Clim. Change*, **111**, 411–424. doi: 10.1007/s10584-011-0208-4.

Baker, Alexader J., Harald Sodemann, James U. L. Baldini, Sebastian F. M. Breitenbach, Kathleen R. Johnson, Jeroen van Hunen, and Zhang Pingzhong (2015). "Seasonality of westerly moisture transport in the East Asian summer monsoon and its implications for interpreting precipitation $\delta^{18}O$". *J. Geophys. Res. Atmos.*, **120**, 5850–5862. doi: 10.1002/2014JD022919.

Barnes, EA and DL Hartmann (2012). "The global distribution of atmospheric eddy-length scales". *J. Climate*, **25**, 3409–3416.

Barnes, Elizabeth A. (2013). "Revisiting the evidence linking Arctic amplification to extreme weather in midlatitudes". *Geophys. Res. Lett.*, **40**, 4734–4739. doi: 10.1002/grl.50880.

Barrios, Salvador, Luisito Bertinelli, and Eric Strobl (2010). "Trends in Rainfall and Economic Growth in Africa: A Neglected Cause of the African Growth Tragedy". *Rev. Econ. Stat.*, **92**, 350–366. doi: 10.1162/rest.2010.11212.

Bhat, G. S., G. A. Vecchi, and S. Gadgil (2004). “Sea surface temperature of the Bay of Bengal derived from the TRMM Microwave Imager”. *J. Atmos. Ocean. Technol.*, **21**, 1283–1290.

Biasutti, Michela, Sandra E. Yuter, Casey D. Burleyson, and Adam H. Sobel (2011). “Very high resolution rainfall patterns measured by TRMM precipitation radar: seasonal and diurnal cycles”. *Clim. Dyn.*, **39**, 239–258. doi: 10.1007/s00382-011-1146-6.

Boos, William R. and John V. Hurley (2013). “Thermodynamic Bias in the Multimodel Mean Boreal Summer Monsoon”. *J. Climate*, **26**, 2279–2287. doi: 10.1175/JCLI-D-12-00493.1.

Boos, William R. and Zhiming Kuang (2010). “Dominant control of the South Asian monsoon by orographic insulation versus plateau heating”. *Nature*, **463**, 218–222. doi: 10.1038/nature08707.

— (2013). “Sensitivity of the South Asian monsoon to elevated and non-elevated heating.” *Sci. Rep.*, **3**, 1192. doi: 10.1038/srep01192.

Boos, William R. and Trude Storelvmo (2016). “Near-linear response of mean monsoon strength to a broad range of radiative forcings”. *Proc. Natl. Acad. Sci.*, **113**, 1510–1515. doi: 10.1073/pnas.1517143113.

Bordoni, Simona and Tapio Schneider (2008). “Monsoons as eddy-mediated regime transitions of the tropical overturning circulation”. *Nat. Geosci.*, **1**, 515–519. doi: 10.1038/ngeo248.

Branstator, Grant (2002). “Circumglobal teleconnections, the jet stream waveguide, and the North Atlantic Oscillation”. *J. Climate*, **15**, 1893–1910.

Burke, Marshall, Solomon M. Hsiang, and Edward Miguel (2015). “Global non-linear effect of temperature on economic production”. *Nature*, **527**, 235–239. doi: 10.1038/nature15725.

Burney, J and V Ramanathan (2014). “Recent Climate and Air Pollution Impacts on Indian Agriculture”. *Proc. Natl. Acad. Sci.*, **111**, 16319–16324. doi: 10.1073/pnas.1317275111.

Burns, Stephen J., Dominik Fleitmann, Albert Matter, Ulrich Neff, and Augusto Mangini (2001). “Speleothem evidence from Oman for continental pluvial events during interglacial periods”. *Geology*, **29**, 623–626.

Cai, Yanjun, Hai Cheng, Zhisheng An, R. Lawrence Edwards, Xianfeng Wang, Liangcheng Tan, and Jin Wang (2010). “Large variations of oxygen isotopes in precipitation over south-central Tibet during Marine Isotope Stage 5”. *Geology*, **38**, 243–246.

Cai, Yanjun, Inez Y. Fung, R. Lawrence Edwards, Zhisheng An, Hai Cheng, Jung-Eun Lee, Liangcheng Tan, Chuan-Chou Shen, Xianfeng Wang, Jesse A. Day, Weijian Zhou, Megan J. Kelly, and John C. H. Chiang (2015). “Variability of stalagmite-inferred Indian monsoon precipitation over the past 252,000 y”. *Proc. Natl. Acad. Sci.*, **112**, 2954–2959. doi: 10.1073/pnas.1424035112.

Cai, Yanjun, Haiwei Zhang, Hai Cheng, Zhisheng An, R. Lawrence Edwards, Xianfeng Wang, Liangcheng Tan, Fuyuan Liang, Jin Wang, and Megan Kelly (2012). “The Holocene Indian monsoon variability over the southern Tibetan Plateau and its teleconnections”. *Earth Planet. Sci. Lett.*, **335-336**, 135–144. doi: 10.1016/j.epsl.2012.04.035.

Cao, Jie, Ping Yao, Lin Wang, and Kui Liu (2014). "Summer Rainfall Variability in Low-Latitude Highlands of China and Subtropical Indian Ocean Dipole". *J. Climate*, **27**, 880–892. doi: 10.1175/JCLI-D-13-00121.1.

Chan, Johnny C. L. (2006). "Comment on "Changes in Tropical Cyclone Number, Duration and Intensity in a Warming Environment"". *Science*, **311**, 1713b.

Chang, Chih-Pei, Yi-Ting Yang, and Hung-Chi Kuo (2013). "Large increasing trend of tropical cyclone rainfall in Taiwan and the roles of terrain". *J. Climate*, **26**, 4138–4147. doi: 10.1175/JCLI-D-12-00463.1.

Chelton, Dudley and Russ Davis (1982). "Monthly Mean Sea-Level Variability Along the West Coast of North America". *J. Phys. Oceanogr.*, **12**, 757–784.

Chen, George Tai-Jen (2004). "Research on the phenomena of Meiyu during the past quarter century: An overview". *East Asian Monsoon*. Ed. by Chang, C.-P. Singapore: World Scientific, 2004, 357–403.

Chen, Jau-Ming and Hui-Shan Chen (2011). "Interdecadal Variability of Summer Rainfall in Taiwan Associated with Tropical Cyclones and Monsoon". *J. Climate*, **24**, 5786–5798. doi: 10.1175/2011JCLI4043.1.

Chen, Jinqiang (2016). "Dynamics of the East Asian Summer Monsoon in Present and Future Climates Thesis". PhD thesis. California Institute of Technology, 2016.

Chen, Jinqiang and Simona Bordoni (2014). "Orographic Effects of the Tibetan Plateau on the East Asian Summer Monsoon: An Energetic Perspective". *J. Climate*, **27**, 3052–3072. doi: 10.1175/JCLI-D-13-00479.1.

Chen, Shou-Jun and Lorenzo Dell'Osso (1984). "Numerical Prediction of the Heavy Rainfall Vortex Over Eastern Asia Monsoon Region". *J. Meteorol. Soc. Japan*, **62**, 730–747.

Chen, Tsing-Chang and Jau-Ming Chen (1993). "The 10-20-Day Mode of the 1979 Indian Monsoon: Its Relation with the Time Variation of Monsoon Rainfall". *Mon. Weather Rev.*, **121**, 2465–2482.

Chen, Tsing-Chang and Shu-Ping Weng (1999). "Interannual and intraseasonal variations in monsoon depressions and their westward-propagating predecessors". *Mon. Weather Rev.*, **127**, 1005–1020.

Chen, Tsing-Chang and Jin-Ho Yoon (2000). "Some remarks on the westward propagation of the monsoon depression". *Tellus A*, **52A**, 487–499.

Chen, Tsing-Chang, Jin-Ho Yoon, and Shih-Yu Wang (2005). "Westward propagation of the Indian monsoon depression". *Tellus A*, **57A**, 758–769.

Cheng, H., P. Z. Zhang, C. Spötl, R. L. Edwards, Y. J. Cai, D. Z. Zhang, W. C. Sang, M. Tan, and Z. S. An (2012). "The climatic cyclicity in semiarid-arid central Asia over the past 500,000 years". *Geophys. Res. Lett.*, **39**, L01705. doi: 10.1029/2011GL050202.

Chiang, John C.H. and Andrew R. Friedman (2012). "Extratropical Cooling, Interhemispheric Thermal Gradients, and Tropical Climate Change". *Annu. Rev. Earth Planet. Sci.*, **40**, 383–412. doi: 10.1146/annurev-earth-042711-105545.

Chiang, John C.H., Inez Y. Fung, Chi-Hua Wu, Yanjun Cai, Jacob P. Edman, Yuwei Liu, Jesse A. Day, Tripti Bhattacharya, Yugarshi Mondal, and Clothilde A. Labrousse (2015).

"Role of seasonal transitions and westerly jets in East Asian paleoclimate". *Quat. Sci. Rev.*, **108**, 111–129. doi: 10.1016/j.quascirev.2014.11.009.

Chou, Chia, J. David Neelin, Chao-An Chen, and Jien-Yi Tu (2009). "Evaluating the "rich-get-richer" mechanism in tropical precipitation change under global warming". *J. Climate*, **22**, 1982–2005. doi: 10.1175/2008JCLI2471.1.

Christensen, J. H., K. Krishna Kumar, E. Aldrian, S.-I. An, I. F. A. Cavalcanti, M. de Castro, W. Dong, P. Goswami, A. Hall, J. K. Kanyanga, A. Kitoh, J. Kossin, N.-C. Lau, J. Renwick, D. B. Stephenson, S.-P. Xie, and Tianjun Zhou (2011). "Climate Phenomena and their Relevance for Future Regional Climate Change". *Climate Change 2013: The Physical Science Basis. Contribution of Working Group I to the Fifth Assessment Report of the Intergovernmental Panel on Climate Change.* Ed. by Stocker, T. F., D. Qin, G.-K. Plattner, M. Tignor, S. K. Allen, J. Boschung, A. Nauels, Y. Xia, V. Bex, and P. M. Midgley. Cambridge, United Kingdom and New York, NY, USA: Cambridge University Press, 2011.

Currell, Matthew J., Dongmei Han, Zongyu Chen, and Ian Cartwright (2012). "Sustainability of groundwater usage in northern China: dependence on palaeowaters and effects on water quality, quantity and ecosystem health". *Hydrol. Process.*, **26**, 4050–4066. doi: 10.1002/hyp.9208.

Dai, Aiguo, Inez Y. Fung, and Anthony D. Del Genio (1997). "Surface observed global land precipitation variations during 1900-88". *J. Climate*, **10**, 2943–2962.

Dansgaard, W. (1964). "Stable isotopes in precipitation". *Tellus*, **16**, 436–468.

Day, Jesse A., Inez Fung, and Camille Risi (2015). "Coupling of South and East Asian Monsoon Precipitation in July-August". *J. Climate*, **28**, 4330–4356. doi: 10.1175/JCLI-D-14-00393.1.

Dayem, Katherine E., Peter Molnar, David S. Battisti, and Gerard H. Roe (2010). "Lessons learned from oxygen isotopes in modern precipitation applied to interpretation of speleothem records of paleoclimate from eastern Asia". *Earth Planet. Sci. Lett.*, **295**, 219–230. doi: 10.1016/j.epsl.2010.04.003.

Ding, Qinghua and Bin Wang (2005). "Circumglobal Teleconnection in the Northern Hemisphere Summer". *J. Climate*, **18**, 3483–3505. doi: 10.1175/JCLI3473.1.

— (2007). "Intraseasonal Teleconnection between the Summer Eurasian Wave Train and the Indian Monsoon", **20**, 3751–3767. doi: 10.1175/JCLI4221.1.

Ding, Yihui and Johnny C. L. Chan (2005). "The East Asian summer monsoon: an overview". *Meteorol. Atmos. Phys.*, **89**, 117–142. doi: 10.1007/s00703-005-0125-z.

Ding, Yihui, Zunya Wang, and Ying Sun (2008). "Inter-decadal variation of the summer precipitation in East China and its association with decreasing Asian summer monsoon . Part I: Observed evidences". *Int. J. Climatol.*, **28**, 1139–1161. doi: 10.1002/joc.1615.

Donohoe, Aaron, John Marshall, David Ferreira, and David Mcgee (2013). "The relationship between ITCZ location and cross-equatorial atmospheric heat transport: From the seasonal cycle to the last glacial maximum". *J. Climate*, **26**, 3597–3618. doi: 10.1175/JCLI-D-12-00467.1.

Du, Yin, Yaocun Zhang, and Zhiqing Xie (2009). "Impacts of the Zonal Position of the East Asian Westerly Jet Core on Precipitation Distribution During Meiyu of China". *Acta Meteorol. Sin.*, **23**, 506–516.

Dykoski, Carolyn A., R. Lawrence Edwards, Hai Cheng, Daoxian Yuan, Yanjun Cai, Meiliang Zhang, Yushi Lin, Jiaming Qing, Zhisheng An, and Justin Revenaugh (2005). "A high-resolution, absolute-dated Holocene and deglacial Asian monsoon record from Dongge Cave, China". *Earth Planet. Sci. Lett.*, **233**, 71–86. doi: 10.1016/j.epsl.2005.01.036.

Eagle, Robert A., Camille Risi, Jonathan L. Mitchell, John M Eiler, Ulrike Seibt, J David Neelin, Gaojun Li, and Aradhna K Tripati (2013). "High regional climate sensitivity over continental China constrained by glacial-recent changes in temperature and the hydrological cycle." *Proc. Natl. Acad. Sci. U. S. A.*, **110**, 8813–8. doi: 10.1073/pnas.1213366110.

Emanuel, KA (1995). "On Thermally Direct Circulations in Moist Atmospheres". *J. Atmos. Sci.*, **52**, 1529–1534.

Fan, Jiwen, Daniel Rosenfeld, Yanni Ding, L. Ruby Leung, and Zhanqing Li (2012). "Potential aerosol indirect effects on atmospheric circulation and radiative forcing through deep convection". *Geophys. Res. Lett.*, **39**, 1–7. doi: 10.1029/2012GL051851.

Feng, Lei and Tianjun Zhou (2012). "Water vapor transport for summer precipitation over the Tibetan Plateau: Multidata set analysis". *J. Geophys. Res.*, **117**, D20114.

Fleitmann, Dominik, Stephen J. Burns, Ulrich Neff, Augusto Mangini, and Albert Matter (2003). "Changing moisture sources over the last 330,000 years in Northern Oman from fluid-inclusion evidence in speleothems". *Quat. Res.*, **60**, 223–232. doi: 10.1016/S0033-5894(03)00086-3.

Francis, Jennifer A. and Stephen J. Vavrus (2012). "Evidence linking Arctic amplifcation to extreme weather in mid-latitudes". *Geophys. Res. Lett.*, **39**, L06801.

Frierson, Dargan M. W., Jian Lu, and Gang Chen (2007). "Width of the Hadley cell in simple and comprehensive general circulation models". *Geophys. Res. Lett.*, **34**, L18804. doi: 10.1029/2007GL031115.

Fu, Qiang, CM Johanson, JM Wallace, and Thomas Reichler (2006). "Enhanced mid-latitude tropospheric warming in satellite measurements". *Science*, **312**, 1179.

Fu, Qiang and Pu Lin (2011). "Poleward shift of subtropical jets inferred from satellite-observed lower-stratospheric temperatures". *J. Climate*, **24**, 5597–5603. doi: 10.1175/JCLI-D-11-00027.1.

Fudeyasu, H., S. Iizuka, and T. Matsuura (2006). "Seasonality of westward-propagating disturbances over Southeast and south Asia originated from typhoons". *Geophys. Res. Lett.*, **33**, L10809. doi: 10.1029/2005GL025380.

Fujinami, Hatsuki, Daisuke Hatsuzuka, Tetsuzo Yasunari, Taiichi Hayashi, Toru Terao, Fumie Murata, Masashi Kiguchi, Yusuke Yamane, Jun Matsumoto, Md. Nazrul Islam, and Arjumand Habib (2011). "Characteristic intraseasonal oscillation of rainfall and its effect on interannual variability over Bangladesh during boreal summer". *Int. J. Climatol.*, **31**, 1192–1204. doi: 10.1002/joc.2146.

Fujinami, Hatsuki, Tetsuzo Yasunari, and Akihito Morimoto (2014). "Dynamics of distinct intraseasonal oscillation in summer monsoon rainfall over the Meghalaya-Bangladesh-western Myanmar region: covariability between the tropics and mid-latitudes”. *Clim. Dyn.*, doi: 10.1007/s00382-013-2040-1.

Gadgil, Sulochana (2003). “The Indian Monsoon and its Variability”. *Annu. Rev. Earth Planet. Sci.*, **31**, 429–467. doi: 10.1146/annurev.earth.31.100901.141251.

Gadgil, Sulochana and Siddhartha Gadgil (2006). “The Indian Monsoon, GDP and Agriculture”. *Econ. Polit. Wkly.*, **41**, 4887–4895.

Gadgil, Sulochana and K Rupa Kumar (2006). “The Asian monsoon - agriculture and economy”. *The Asian Monsoon.* 2006, 651–683. doi: 10.1007/3-540-37722-0–“˙”18.

Gadgil, Sulochana and J. Srinivasan (2011). “Seasonal prediction of the Indian monsoon”. *Curr. Sci.*, **100**, 343–353. doi: 10.1007/s00024-005-2678-7.

Gao, Jing, Valerie Masson-Delmotte, Camille Risi, You He, and Tandong Yao (2013). “What controls precipitation δ^{18}O in the southern Tibetan Plateau at seasonal and intra-seasonal scales? A case study at Lhasa and Nyalam”. *Tellus B*, **65**, 21043.

Gao, Jing, Valerie Masson-Delmotte, Tandong Yao, Lide Tian, Camille Risi, and G. Hoffmann (2011). “Precipitation Water Stable Isotopes in the South Tibetan Plateau: Observations and Modeling”. *J. Climate*, **24**, 3161–3178. doi: 10.1175/2010JCLI3736.1.

Gao, Y. C. and M. F. Liu (2013). “Evaluation of high-resolution satellite precipitation products using rain gauge observations over the Tibetan Plateau”. *Hydrol. Earth Syst. Sci.*, **17**, 837–849. doi: 10.5194/hess-17-837-2013.

Ge, QuanSheng, XiFeng Guo, JingYun Zheng, and ZhiXin Hao (2008). “Meiyu in the middle and lower reaches of the Yangtze River since 1736”. *Chinese Sci. Bull.*, **53**, 107–114. doi: 10.1007/s11434-007-0440-5.

Gemmer, Marco, Tong Jiang, Buda Su, and Zbigniew W. Kundzewicz (2008). “Seasonal precipitation changes in the wet season and their influence on flood/drought hazards in the Yangtze River Basin, China”. *Quat. Int.*, **186**, 12–21. doi: 10.1016/j.quaint.2007.10.001.

Ghude, Sachin D., Chinmay Jena, D. M. Chate, G. Beig, G. G. Pfister, Rajesh Kumar, and V. Ramanathan (2014). “Reductions in India’s crop yield due to ozone”. *Geophys. Res. Lett.*, **41**, 5685–5691. doi: 10.1002/2014GL061266.Received.

Gleeson, Tom, Yoshihide Wada, Marc F. P. Bierkens, and Ludovicus P. H. van Beek (2012). “Water balance of global aquifers revealed by groundwater footprint.” *Nature*, **488**, 197–200. doi: 10.1038/nature11295.

Gong, Dao-Yi and Chang-Hoi Ho (2002). “Shift in the summer rainfall over the Yangtze River valley in the late 1970s”. *Geophys. Res. Lett.*, **29**, 1436. doi: 10.1029/2001GL014523.

Good, Phillip (2005). *Permutation, parametric and bootstrap tests of hypotheses.* 3rd ed. New York, NY: Springer, 2005.

Hahn, Douglas G. and Syukuro Manabe (1975). “The role of mountains in the south Asian monsoon circulation”. *J. Atmos. Sci.*, **32**, 1515–1541.

Halley, E. (1686). “An Historical Account of the Trade Winds, and Monsoons, Observable in the Seas between and Near the Tropicks, with an Attempt to Assign the Phisical Cause of the Said Winds, By E. Halley”. *Philos. Trans. R. Soc. London*, **16**, 153–168. doi: 10.1098/rstl.1686.0026.

Han, Weiqing, W. Timothy Liu, and Jialin Lin (2006). "Impact of atmospheric submonthly oscillations on sea surface temperature of the tropical Indian Ocean". *Geophys. Res. Lett.*, **33**, L03609. doi: 10.1029/2005GL025082.

Hansen, James and Sergej Lebedeff (1987). "Global trends of measured surface air temperature". *J. Geophys. Res.*, **92**, 13345–13372.

Harada, Yayoi, Hirotaka Kamahori, Chiaki Kobayashi, Hirokazu Endo, Shinya Kobayashi, Yukinari Ota, Hirokatsu Onoda, Kazutoshi Onogi, Kengo Miyaoka, and Kiyotoshi Takahashi (2016). "The JRA-55 Reanalysis: Representation of atmospheric circulation and climate variability". *J. Meteorol. Soc. Japan*, **1**, doi: 10.2151/jmsj.2016-015.

Harrison, T. Mark, Peter Copeland, W. S. F. Kidd, and An Yin (1992). "Raising Tibet". *Science*, **255**, 1663–1670. doi: 10.1126/science.255.5052.1663.

Hassanzadeh, Pedram, Zhiming Kuang, and Brian F. Farrell (2014). "Responses of midlatitude blocks and wave amplitude to changes in the meridional temperature gradient in an idealized dry GCM". *Geophys. Res. Lett.*, **41**, 5223–5232. doi: 10.1002/2014GL060764.

Held, IM and BJ Soden (2006). "Robust responses of the hydrological cycle to global warming". *J. Climate*, **19**, 5686–5699.

Hoerling, Martin, Arun Kumar, and Min Zhong (1997). "El Nino, La Nina, and the Nonlinearity of Their Teleconnections". *J. Climate*, **10**, 1769–1786.

Holton, James R. (2004a). *An Introduction to Dynamic Meteorology.* 4th. Academic Press, 2004, 269–278.

— (2004b). *An Introduction to Dynamic Meteorology.* 4th. Academic Press, 2004, 86–115.

Hoskins, Brian J. and Tercio Ambrizzi (1993). "Rossby Wave Propagation on a Realistic Longitudinally Varying Flow". *J. Atmos. Sci.*, **50**, 1661–1671.

Hourdin, Frédéric, Jean-Yves Grandpeix, Catherine Rio, Sandrine Bony, Arnaud Jam, Frédérique Cheruy, Nicolas Rochetin, Laurent Fairhead, Abderrahmane Idelkadi, Ionela Musat, Jean-Louis Dufresne, Alain Lahellec, Marie-Pierre Lefebvre, and Romain Roehrig (2012). "LMDZ5B: the atmospheric component of the IPSL climate model with revisited parameterizations for clouds and convection". *Clim. Dyn.*, **40**, 2193–2222. doi: 10.1007/s00382-012-1343-y.

Hourdin, Frédéric, Ionela Musat, Sandrine Bony, Pascale Braconnot, Francis Codron, Jean-Louis Dufresne, Laurent Fairhead, Marie-Angèle Filiberti, Pierre Friedlingstein, Jean-Yves Grandpeix, Gerhard Krinner, Phu LeVan, Zhao-Xin Li, and François Lott (2006). "The LMDZ4 general circulation model: climate performance and sensitivity to parametrized physics with emphasis on tropical convection". *Clim. Dyn.*, **27**, 787–813. doi: 10.1007/s00382-006-0158-0.

Hsiang, Solomon M and Amir S Jina (2014). *The causal effect of environmental catastrophe on long-run economic growth: Evidence from 6,700 cyclones.* National Bureau of Economic Research Working Paper No. 20352. 2014. doi: 10.3386/w20352.

Hu, Jun and Anmin Duan (2015). "Relative contributions of the Tibetan Plateau thermal forcing and the Indian Ocean Sea surface temperature basin mode to the interannual variability of the East Asian summer monsoon". *Clim. Dyn.*, doi: 10.1007/s00382-015-2503-7.

Hu, Zeng-Zhen (1997). “Interdecadal variability of summer climate over East Asia and its association with 500 hPa height and global sea surface temperature”. *J. Geophys. Res.*, **102**, 19403. doi: 10.1029/97JD01052.

Hurley, John V. and William R. Boos (2013). “Interannual variability of monsoon precipitation and subcloud equivalent potential temperature”. *J. Climate*, **26**, 9507–9527.

Husak, Gregory J., Joel Michaelsen, and Chris Funk (2007). “Use of the gamma distribution to represent monthly rainfall in Africa for drought monitoring applications”. *Int. J. Climatol.*, **27**, 935–944. doi: 10.1002/joc.

Iguchi, Toshio, Toshiaki Kozu, John Kwiatkowski, Robert Meneghini, Jun Awaka, and Ken’ichi Okamoto (2009). “Uncertainties in the Rain Profiling Algorithm for the TRMM Precipitation Radar”. *J. Meteorol. Soc. Japan*, **87A**, 1–30. doi: 10.2151/jmsj.87A.1.

Ihara, Chie, Yochanan Kushnir, Mark A. Cane, and Victor H. De La Peña (2007). “Indian summer monsoon rainfall and its link with ENSO and Indian Ocean climate indices”. *Int. J. Climatol.*, **187**, 179–187. doi: 10.1002/joc.

Jhun, Jong-Ghap and Eun-Jeong Lee (2004). “A new East Asian winter monsoon index and associated characteristics of the winter monsoon”. *J. Climate*, **17**, 711–726.

Jiménez Cisneros, Blanca E., Taikan Oki, Nigel W. Arnell, Gerardo Benito, J. Graham Cogley, Petra Döll, Tong Jiang, Shadrack S. Mwakalila, Thomas Fischer, Dieter Gerten, Regina Hock, Shinjiro Kanae, Xixi Lu, Luis José Mata, Claudia Pahl-Wostl, Kenneth M. Strzepek, Buda Su, B. van den Hurk, Pavel Kabat, Zbigniew Kundzewicz, and Asako Nishijima (2014). “Freshwater Resources”. *Climate Change 2014: Impacts, Adaptation and Vulnerability. Part A: Global and Sectoral Aspects. Contribution of Working Group II to the Fifth Assessment Report of the Intergovernment Panel on Climate Change.* Ed. by Field, C.B., V.R. Barros, D.J. Dokken, K.J. Mach, M.D. Mastrandrea, T.E. Bilir, M. Chatterjee, K.L. Ebi, Y.O. Estrada, R.C. Genova, B. Girma, E.S. Kissel, A.N. Levy, S. MacCracken, P.R. Mastrandrea, and L.L. White. October 2013. Cambridge, United Kingdom and New York, NY, USA: Cambridge University Press, 2014.

Kaiser, Henry F. (1958). “The Varimax Criterion for Analytic Rotation in Factor Analysis”. *Psychometrika*, **23**, 187–200.

Kang, Sarah M. and Jian Lu (2012). “Expansion of the Hadley Cell under Global Warming: Winter versus Summer”. *J. Climate*, **25**, 8387–8393. doi: 10.1175/JCLI-D-12-00323.1.

Kang, Sarah M. and Lorenzo M. Polvani (2011). “The interannual relationship between the latitude of the eddy-driven jet and the edge of the Hadley cell”. *J. Climate*, **24**, 563–568. doi: 10.1175/2010JCLI4077.1.

Kansakar, Sunil R., David M. Hannah, John Gerrard, and Gwyn Rees (2004). “Spatial pattern in the precipitation regime of Nepal”. *Int. J. Climatol.*, **24**, 1645–1659. doi: 10.1002/joc.1098.

Kennedy, J. J., N. A. Rayner, R. O. Smith, D. E. Parker, and M. Saunby (2011a). “Reassessing biases and other uncertainties in sea surface temperature observations measured in situ since 1850: 1. Measurement and sampling”. *J. Geophys. Res.*, **116**, D14103. doi: 10.1029/2010JD015218.

Kennedy, J. J., N. A. Rayner, R. O. Smith, D. E. Parker, and M. Saunby (2011b). "Reassessing biases and other uncertainties in sea surface temperature observations measured in situ since 1850: 2. Biases and homogenization". *J. Geophys. Res.*, **116**, D14104. doi: 10.1029/2010JD015220.

Kobayashi, Shinya, Yukinari Ota, Yayoi Harada, Ayataka Ebita, Masami Moriya, Hirokatsu Onoda, Kazutoshi Onogi, Hirotaka Kamahori, Chiaki Kobayashi, Hirokazu Endo, Kengo Miyaoka, and Kiyotoshi Takahashi (2015). "The JRA-55 Reanalysis: General Specifications and Basic Characteristics". *J. Meteorol. Soc. Japan*, **93**, 5–48. doi: 10.2151/jmsj.2015-001.

Kosaka, Yu, J. S. Chowdary, Shang-Ping Xie, Young-Mi Min, and June-Yi Lee (2012). "Limitations of Seasonal Predictability for Summer Climate over East Asia and the Northwestern Pacific". *J. Climate*, **25**, 7574–7589. doi: 10.1175/JCLI-D-12-00009.1.

Kosaka, Yu, Shang-Ping Xie, and Hisashi Nakamura (2011). "Dynamics of Interannual Variability in Summer Precipitation over East Asia". *J. Climate*, **24**, 5435–5453. doi: 10.1175/2011JCLI4099.1.

Krishna Kumar, K., Martin Hoerling, and Balaji Rajagopalan (2005). "Advancing dynamical prediction of Indian monsoon rainfall". *Geophys. Res. Lett.*, **32**, L08704.

Krishna Kumar, K., K. Rupa Kumar, R. G. Ashrit, N. R. Deshpande, and J. W. Hansen (2004). "Climate impacts on Indian agriculture". *Int. J. Climatol.*, **24**, 1375–1393. doi: 10.1002/joc.1081.

Krishnamurthy, V. and R. S. Ajayamohan (2010). "Composite Structure of Monsoon Low Pressure Systems and Its Relation to Indian Rainfall". *J. Climate*, **23**, 4285–4305. doi: 10.1175/2010JCLI2953.1.

Krishnamurthy, V. and Jagadish Shukla (2000). "Intraseasonal and Interannual Variability of Rainfall over India". *J. Climate*, **13**, 4366–4377.

Krishnamurti, T. N. and Philip Ardanuy (1980). "The 10 to 20-day westward propagating mode and Breaks in the Monsoon". *Tellus*, **32**, 15–26.

Krishnan, R and M Sugi (2001). "Baiu Rainfall Variability and Associated Monsoon Teleconnections". *J. Meteorol. Soc. Japan*, **79**, 851–860.

Krishnan, R., C. Zhang, and M. Sugi (2000). "Dynamics of Breaks in the Indian Summer Monsoon". *J. Atmos. Sci.*, **57**, 1354–1372.

Kumar, K. Krishna, Balaji Rajagopalan, Martin Hoerling, Gary Bates, and Mark Cane (2006). "Unraveling the mystery of Indian monsoon failure during El Niño". *Science*, **314**, 115–119. doi: 10.1126/science.1131152.

Kumar, Vinay and R. Krishnan (2005). "On the association between the Indian summer monsoon and the tropical cyclone activity over northwest Pacific". *Curr. Sci.*, **88**, 602–612.

Kwon, MinHo, Jong-Ghap Jhun, and Kyung-Ja Ha (2007). "Decadal change in east Asian summer monsoon circulation in the mid-1990s". *Geophys. Res. Lett.*, **34**, L21706. doi: 10.1029/2007GL031977.

Lau, KM, KM Kim, and S Yang (2000). "Dynamical and boundary forcing characteristics of regional components of the Asian summer monsoon". *J. Climate*, **13**, 2461–2482.

Lau, William K. M. and Kyu-Myong Kim (2012). “The 2010 Pakistan Flood and Russian Heat Wave: Teleconnection of Hydrometeorological Extremes”. *J. Hydrometeor.*, **13**, 392–403. doi: 10.1175/JHM-D-11-016.1.

Lee, June Yi, Bin Wang, Kyong Hwan Seo, Jong Seong Kug, Yong Sang Choi, Yu Kosaka, and Kyung Ja Ha (2014). “Future change of Northern Hemisphere summer tropical-extratropical teleconnection in CMIP5 models”. *J. Climate*, **27**, 3643–3664.

Lee, Jung-Eun, Camille Risi, Inez Y. Fung, John Worden, Remco A. Scheepmaker, Benjamin Lintner, and Christian Frankenberg (2012). “Asian monsoon hydrometeorology from TES and SCIAMACHY water vapor isotope measurements and LMDZ simulations: Implications for speleothem climate record interpretation”. *J. Geophys. Res.*, **117**, D15112. doi: 10.1029/2011JD017133.

Lei, Yonghui, Brian Hoskins, and Julia Slingo (2014). “Natural variability of summer rainfall over China in HadCM3”. *Clim. Dyn.*, **42**, 417–432. doi: 10.1007/s00382-013-1726-8.

Li, Chengfeng and Michio Yanai (1996). “The Onset and Interannual Variability of the Asian Summer Monsoon in Relation to Land-Sea Thermal Contrast”. *J. Climate*, **9**, 358–375.

Li, Kaizhong, Shaohong Wu, Erfu Dai, and Zhongchun Xu (2012). “Flood loss analysis and quantitative risk assessment in China”. *Nat. Hazards*, **63**, 737–760. doi: 10.1007/s11069-012-0180-y.

Li, Li and Yaocun Zhang (2014). “Effects of Different Configurations of the East Asian Subtropical and Polar Front Jets on Precipitation during the Mei-Yu Season”. *J. Climate*, **27**, 6660–6672. doi: 10.1175/JCLI-D-14-00021.1.

Li, Zhanqing, Kwon Ho Lee, Yuesi Wang, Jinyuan Xin, and Wei Min Hao (2010). “First observation-based estimates of cloud-free aerosol radiative forcing across China”. *J. Geophys. Res. Atmos.*, **115**, D00K18. doi: 10.1029/2009JD013306.

Li, Zhi, Weidong Yu, Tim Li, V. S. N. Murty, and Fredolin Tangang (2013). “Bimodal Character of Cyclone Climatology in the Bay of Bengal Modulated by Monsoon Seasonal Cycle”. *J. Climate*, **26**, 1033–1046. doi: 10.1175/JCLI-D-11-00627.1.

Liang, Xin-Zhong and Wei-Chyung Wang (1998). “Associations between China monsoon rainfall and tropospheric jets”. *Q. J. R. Meteorol. Soc.*, **124**, 2597–2623.

Lintner, Benjamin and J. David Neelin (2007). “A prototype for convective margin shifts”. *Geophys. Res. Lett.*, **34**, L05812. doi: 10.1029/2006GL027305.

Liu, K. S. and Johnny C. L. Chan (2003). “Climatological characteristics and seasonal forecasting of tropical cyclones making landfall along the South China coast”. *Mon. Weather Rev.*, **131**, 1650–1662.

Liu, Y. and J. C. H. Chiang (2012). “Coordinated Abrupt Weakening of the Eurasian and North African Monsoons in the 1960s and Links to Extratropical North Atlantic Cooling”. *J. Climate*, **25**, 3532–3548. doi: 10.1175/JCLI-D-11-00219.1.

Liu, Yimin, Guoxiong Wu, Jieli Hong, Buwen Dong, Anmin Duan, Qing Bao, and Linjiong Zhou (2012). “Revisiting Asian monsoon formation and change associated with Tibetan Plateau forcing: II. Change”. *Clim. Dyn.*, **39**, 1183–1195. doi: 10.1007/s00382-012-1335-y.

Liu, YunYun and YiHui Ding (2008). “Teleconnection between the Indian summer monsoon onset and the Meiyu over the Yangtze River Valley”. *Sci. China Ser. D Earth Sci.*, **51**, 1021–1035. doi: 10.1007/s11430-008-0073-9.

Liu, Zhengyu, Xinyu Wen, E.C. Brady, B. Otto-Bliesner, Ge Yu, Huayu Lu, Hai Cheng, Yongjin Wang, Weipeng Zheng, Yihui Ding, R.L. Edwards, Jun Cheng, Wei Liu, and Hao Yang (2014). “Chinese cave records and the East Asia Summer Monsoon”. *Quat. Sci. Rev.*, **83**, 115–128. doi: 10.1016/j.quascirev.2013.10.021.

Livezey, Robert E. and W. Y. Chen (1983). “Statistical Field Significance and its Determination by Monte Carlo Techniques”. *Mon. Weather Rev.*, **111**, 46–59.

Lorenz, Edward N. (1956). *Empirical orthogonal functions and statistical weather prediction.* Statistical Forecasting Project Sci. Rep. No. 1. Massachusetts Institute of Technology, 1956, 49.

Lu, Jian, Gabriel A. Vecchi, and Thomas Reichler (2007). “Expansion of the Hadley cell under global warming”. *Geophys. Res. Lett.*, **34**, L06805. doi: 10.1029/2006GL028443.

Luo, Yali, Renhe Zhang, Weimiao Qian, Zhengzhao Luo, and Xin Hu (2011). “Intercomparison of Deep Convection over the Tibetan Plateau-Asian Monsoon Region and Subtropical North America in Boreal Summer Using CloudSat/CALIPSO Data”. *J. Climate*, **24**, 2164–2177. doi: 10.1175/2010JCLI4032.1.

Magee, Darrin (2011). “Moving the River? China’s South-North Water Transfer Project”. *Engineering Earth.* Ed. by Brunn, Stanley D. Vol. 53. Dordrecht: Springer Netherlands, 2011. Chap. 85, 1499–1514. doi: 10.1007/978-90-481-9920-4.

Maher, B.A. (2008). “Holocene variability of the East Asian summer monsoon from Chinese cave records: a re-assessment”. *The Holocene*, **18**, 861–866. doi: 10.1177/0959683608095569.

Mantua, Nathan J. and Steven R. Hare (2002). “The Pacific Decadal Oscillation”. *J. Oceanogr.*, **58**, 35–44.

Matsuura, Kenji and Cort J. Willmott. *Terrestrial Precipitation: 1900-2014 Gridded Monthly Time Series.* `http://climate.geog.udel.edu/~climate/html_pages/download.html` . Accessed: 2016-03-23. N.d.

Medina, Socorro, Robert A. Houze, Anil Kumar, and Dev Niyogi (2010). “Summer monsoon convection in the Himalayan region: terrain and land cover effects”. *Q. J. R. Meteorol. Soc.*, **136**, 593–616. doi: 10.1002/qj.601.

Menon, Surabi, James Hansen, Larissa Nazarenko, and Yunfeng Luo (2002). “Climate effects of black carbon aerosols in China and India.” *Science*, **297**, 2250–2253.

Mishra, Vimal, Brian V Smoliak, Dennis P Lettenmaier, and John M Wallace (2012). “A prominent pattern of year-to-year variability in Indian Summer Monsoon Rainfall”. *Proc. Natl. Acad. Sci. U. S. A.*, **109**, 7213–7. doi: 10.1073/pnas.1119150109.

Molnar, Peter, William R. Boos, and David S. Battisti (2010). “Orographic Controls on Climate and Paleoclimate of Asia: Thermal and Mechanical Roles for the Tibetan Plateau”. *Annu. Rev. Earth Planet. Sci.*, **38**, 77–102. doi: 10.1146/annurev-earth-040809-152456.

Molnar, Peter and Kerry A. Emanuel (1999). “Temperature Profiles in Radiative-Convective Equilibrium above Surfaces at different heights”. *J. Geophys. Res.*, **104**, 24265–24271.

Molnar, Peter, Philip England, and Joseph Martinod (1993). “Mantle dynamics, uplift of the Tibetan Plateau, and the Indian Monsoon”. *Rev. Geophys.*, **31**, 357–396. doi: 10.1029/93RG02030.

Mooley, Diwakar A. (1973). “Gamma Distribution Probability Model for Asian Summer Monsoon Monthly Rainfall”. *Mon. Weather Rev.*, **101**, 160–176.

Muller, Caroline J., Paul A. O’Gorman, and Larissa E. Back (2011). “Intensification of Precipitation Extremes with Warming in a Cloud-Resolving Model”. *J. Climate*, **24**, 2784–2800. doi: 10.1175/2011JCLI3876.1.

Murakami, Takio and Wen-Gen Huang (1984). “Orographic effects of the Tibetan Plateau on the rainfall variations over central China during the 1979 summer”. *J. Meteorol. Soc. Japan*, **62**, 895–909.

Naylor, Rosamond L., David S. Battisti, Daniel J. Vimont, Walter P. Falcon, and Marshall B. Burke (2007). “Assessing risks of climate variability and climate change for Indonesian rice agriculture”. *Proc. Natl. Acad. Sci. U. S. A.*, **104**, 7752–7757.

Nie, Ji, William R. Boos, and Zhiming Kuang (2010). “Observational Evaluation of a Convective Quasi-Equilibrium View of Monsoons”. *J. Climate*, **23**, 4416–4428.

Nigam, Sumant, Yongjing Zhao, and Tianjun Zhou (2013). “The south-flood north-drought pattern over Eastern China and the drying of the Gangetic Plain”. *Climate Change: Multidecadal and Beyond*. Ed. by Michael Ghil, Mojif Latif, Mike Wallace and C.P. Chan. Vol. 1. World Press, 2013.

Norris, Joel R. and Martin Wild (2009). “Trends in aerosol radiative effects over China and Japan inferred from observed cloud cover, solar “dimming,” and solar “brightening””. *J. Geophys. Res. Atmos.*, **114**, D00D15. doi: 10.1029/2008JD011378.

North, Gerald R., Thomas L. Bell, Robert F. Cahalan, and Fanthune J. Moeng (1982). “Sampling Errors in the Estimation of Empirical Orthogonal Functions”. *Mon. Weather Rev.*, **110**, 699–706.

O’Gorman, Paul A. (2012). “Sensitivity of tropical precipitation extremes to climate change”. *Nat. Geosci.*, **5**, 697–700. doi: 10.1038/ngeo1568.

O’Gorman, Paul A. and Tapio Schneider (2009). “Scaling of precipitation extremes over a wide range of climates simulated with an idealized GCM”. *J. Climate*, **22**, 5676–5685. doi: 10.1175/2009JCLI2701.1.

Park, Chung-Kyu and Siegfried D. Schubert (1997). “On the nature of the 1994 East Asian summer drought”. *J. Climate*, **10**, 1056–1070.

Park, Jae-Heung and Soon-Il An (2014a). “Southward displacement of the upper atmosphere zonal Jet in the eastern north Pacific due to global warming”. *Geophys. Res. Lett.*, **41**, 7861–7867. doi: 10.1002/2014GL062175.

— (2014b). “The impact of tropical western Pacific convection on the North Pacific atmospheric circulation during the boreal winter”. *Clim. Dyn.*, **43**, 2227–2238.

Parthasarathy, B, AA Munot, and DR Kothawale (1994). “All-India Monthly and Seasonal Rainfall Series : 1871-1993”. *Theor. Appl. Climatol.*, **224**, 217–224.

Pausata, Francesco S. R., David S. Battisti, Kerim H. Nisancioglu, and Cecilia M. Bitz (2011). “Chinese stalagmite δ^{18}O controlled by changes in the Indian monsoon during a simulated Heinrich event”. *Nat. Geosci.*, **4**, 474–480. doi: 10.1038/ngeo1169.

Peña-Arancibia, Jorge L., Albert I. J. M. van Dijk, Luigi J. Renzullo, and Mark Mulligan (2013). “Evaluation of Precipitation Estimation Accuracy in Reanalyses, Satellite Products, and an Ensemble Method for Regions in Australia and South and East Asia”. *J. Hydrometeor.*, **14**, 1323–1333. doi: 10.1175/JHM-D-12-0132.1.

Pendergrass, Angeline G and Dennis L Hartmann (2014). “Changes in the distribution of rain frequency and intensity in response to global warming”. *J. Climate*, **27**, 8372–8383. doi: 10.1175/JCLI-D-14-00183.1.

Peng, Shaobing, Jianliang Huang, John E. Sheehy, Rebecca C. Laza, Romeo M. Visperas, Xuhua Zhong, Grace S. Centeno, Gurdev S. Khush, and Kenneth G. Cassman (2004). “Rice yields decline with higher night temperature from global warming.” *Proc. Natl. Acad. Sci. U. S. A.*, **101**, 9971–9975. doi: 10.1073/pnas.0403720101.

Petoukhov, Vladimir, Stefan Rahmstorf, Stefan Petri, and Hans Joachim Schellnhuber (2013). “Quasiresonant amplification of planetary waves and recent Northern Hemisphere weather extremes”. *Proc. Natl. Acad. Sci.*, **110**, 5336–5341. doi: 10.1073/pnas.1222000110.

Plumb, R. Alan and Arthur Y. Hou (1992). “Response of a Zonally Symmetric Atmosphere to Subtropical Thermal Forcing”. *J. Atmos. Sci.*, **49**, 1790–1799.

Preisendorfer, Rudolph W., Francis W. Zwiers, and Tim P. Barnett (1981). “Foundations of principal component selection rules”. *SIO Ref. Ser.*, **81-4**,

Privé, Nikki C. and R. Alan Plumb (2007a). “Monsoon Dynamics with Interactive Forcing. Part I: Axisymmetric Studies”. *J. Atmos. Sci.*, **64**, 1417–1430. doi: 10.1175/JAS3916.1.

— (2007b). “Monsoon Dynamics with Interactive Forcing. Part II: Impact of Eddies and Asymmetric Geometries”. *J. Atmos. Sci.*, **64**, 1431–1442. doi: 10.1175/JAS3917.1.

Qiu, Jane (2013). “Monsoon melee”. *Science*, **340**, 1400–1401.

Qu, Xia and Gang Huang (2012). “Impacts of tropical Indian Ocean SST on the meridional displacement of East Asian jet in boreal summer”. *Int. J. Climatol.*, **32**, 2073–2080. doi: 10.1002/joc.2378.

Rajagopalan, Balaji and Peter Molnar (2013). “Signatures of Tibetan Plateau heating on Indian summer monsoon rainfall variability”. *J. Geophys. Res. Atmos.*, **118**, 1170–1178. doi: 10.1002/jgrd.50124.

Rajeevan, M., Jyoti Bhate, J. D. Kale, and B. Lal (2006). “High resolution daily gridded rainfall data for the Indian region: Analysis of break and active monsoon spells”. *Curr. Sci.*, **91**, 296–306.

Risi, Camille, Sandrine Bony, Françoise Vimeux, and Jean Jouzel (2010). “Water-stable isotopes in the LMDZ4 general circulation model: Model evaluation for present-day and past climates and applications to climatic interpretations of tropical isotopic records”. *J. Geophys. Res.*, **115**, D12118. doi: 10.1029/2009JD013255.

Rodriguez, Mathieu, Nicolas Chamot-Rooke, Philippe Huchon, Marc Fournier, and Matthias Delescluse (2014). “The Owen Ridge uplift in the Arabian Sea: Implications for the sedimentary record of Indian monsoon in Late Miocene". *Earth Planet. Sci. Lett.*, **394**, 1–12.

Rodwell, M. J. and B. J. Hoskins (2001). "Subtropical anticyclones and summer monsoons". *J. Climate*, **14**, 3192–3211.

Roe, Gerard (2009). "On the interpretation of Chinese loess as a paleoclimate indicator". *Quat. Res.*, **71**, 150–161. doi: 10.1016/j.yqres.2008.09.004.

Rohde, Robert, Richard Muller, Robert Jacobsen, Eizabeth Muller, Donald Groom, and Charlotte Wickham (2012). "A New Estimate of the Average Earth Surface Land Temperature Spanning 1753 to 2011". *Geoinfor Geostat*, **1**, 1–7. doi: 10.4172/gigs.1000101.

Rohde, Robert, Richard Muller, Robert Jacobsen, Saul Perlmutter, Arthur Rosenfeld, Jonathan Wurtele, Judith Curry, Charlotte Wickham, and Steven Mosher (2013). "Berkeley Earth Temperature Averaging Process". *Geoinfor Geostat*, **1**, 1–13. doi: 10.4172/gigs.1000103.

Romatschke, Ulrike and Robert A. Houze (2011). "Characteristics of Precipitating Convective Systems in the South Asian Monsoon". *J. Hydrometeor.*, **12**, 3–26.

Saha, Kshudiram, Frederick Sanders, and Jagadish Shukla (1981). "Westward propagating predecessors of monsoon depressions". *Mon. Weather Rev.*, **109**, 330–343.

Saji, N. H., B. N. Goswami, P. N. Vinayachandran, and T. Yamagata (1999). "A dipole mode in the tropical Indian Ocean". *Nature*, **401**, 360–363. doi: 10.1038/43854.

Sampe, Takeaki and Shang-Ping Xie (2010). "Large-Scale Dynamics of the Meiyu-Baiu Rainband: Environmental Forcing by the Westerly Jet". *J. Climate*, **23**, 113–134. doi: 10.1175/2009JCLI3128.1.

Schiemann, Reinhard, Daniel Lüthi, and Christoph Schär (2009). "Seasonality and Interannual Variability of the Westerly Jet in the Tibetan Plateau Region". *J. Climate*, **22**, 2940–2957. doi: 10.1175/2008JCLI2625.1.

Schlenker, Wolfram and Michael J Roberts (2009). "Nonlinear temperature effects indicate severe damages to U.S. crop yields under climate change". *Proc. Natl. Acad. Sci.*, **106**, 15594–15598. doi: 10.1073/pnas.0906865106.

Schneider, Tapio, Tobias Bischoff, and Gerald H. Haug (2014). "Migrations and dynamics of the intertropical convergence zone". *Nature*, **513**, 45–53. doi: 10.1038/nature13636.

Schneider, Tapio and Simona Bordoni (2008). "Eddy-Mediated Regime Transitions in the Seasonal Cycle of a Hadley Circulation and Implications for Monsoon Dynamics". *J. Atmos. Sci.*, **65**, 915–934. doi: 10.1175/2007JAS2415.1.

Schubert, Siegfried, Hailan Wang, Randal Koster, Max Suarez, and Pavel Groisman (2014). "Northern Eurasian Heat Waves and Droughts". *J. Climate*, **27**, 3169–3207.

Schubert, Siegfried, Hailan Wang, and Max Suarez (2011). "Warm season subseasonal variability and climate extremes in the northern hemisphere: The role of stationary Rossby waves". *J. Climate*, **24**, 4773–4792. doi: 10.1175/JCLI-D-10-05035.1.

Shen, Yan, Ping Zhao, Yang Pan, and Jingjing Yu (2014). "A high spatiotemporal gauge-satellite merged precipitation analysis over China". *J. Geophys. Res. Atmos.*, **119**, doi: 10.1002/2013JD020686.

Sikka, D. R. (1977). "Some aspects of the life history, structure and movement of monsoon depressions". *Pure Appl. Geophys.*, **115**, 1501–1529. doi: 10.1007/BF00874421.

Singh, Deepti, Michael Tsiang, Bala Rajaratnam, and Noah S. Diffenbaugh (2014). "Observed changes in extreme wet and dry spells during the South Asian summer monsoon season". *Nat. Clim. Chang.*, **4**, 456–461. doi: 10.1038/NCLIMATE2208.

Smith, Thomas M., Richard W. Reynolds, Thomas C. Peterson, and Jay Lawrimore (2008). "Improvements to NOAA's Historical Merged Land-Ocean Surface Temperature Analysis (1880-2006)". *J. Climate*, **21**, 2283–2296. doi: 10.1175/2007JCLI2100.1.

Song, Fengfei, Tianjun Zhou, and Yun Qian (2014). "Responses of East Asian summer monsoon to natural and anthropogenic forcings in the 17 latest CMIP5 models". *Geophys. Res. Lett.*, **41**, 596–603. doi: 10.1002/2013GL058705.Received.

Stevens, Bjorn and Sandrine Bony (2013). "Climate change. What are climate models missing?" *Science*, **340**, 1053–1054. doi: 10.1126/science.1237554.

Streets, David G., Drew T. Shindell, Zifeng Lu, and Greg Faluvegi (2013). "Radiative forcing due to major aerosol emitting sectors in China and India". *Geophys. Res. Lett.*, **40**, 4409–4414. doi: 10.1002/grl.50805.

Sun, Youbin, Jun Chen, Steven C. Clemens, Qingsong Liu, Junfeng Ji, and Ruiji Tada (2006). "East Asian monsoon variability over the last seven glacial cycles recorded by a loess sequence from the northwestern Chinese Loess Plateau". *Geochemistry, Geophys. Geosystems*, **7**, 1–16. doi: 10.1029/2006GC001287.

Tao, Shi-Yen and Yi-Hui Ding (1981). "Observational evidence of the influence of the Qinghai-Xizang (Tibet) Plateau on the occurrence of heavy rain and severe convective storms in China". *Bull. Am. Meteorol. Soc.*, **62**, 23–30.

Tian, Shao-Fen and Tetsuzo Yasunari (1998). "Climatological Aspects and Mechanism of Spring Persistent Rains over Central China". *J. Meteorol. Soc. Japan*, **76**, 57–71.

Tong, Kai, Fengge Su, Daqing Yang, Leilei Zhang, and Zhenchun Hao (2014). "Tibetan Plateau precipitation as depicted by gauge observations, reanalyses and satellite retrievals". *Int. J. Climatol.*, **34**, 265–285. doi: 10.1002/joc.3682.

Trenberth, Kevin E. (1991). "Climate Diagnostics from Global Analyses: Conservation of Mass in ECMWF Analyses". *J. Climate*, **4**, 707–722.

Trenberth, Kevin E., Aiguo Dai, Roy M. Rasmussen, and David B. Parsons (2003). "The Changing Character of Precipitation". *Bull. Am. Meteorol. Soc.*, **84**, 1205–1217. doi: 10.1175/BAMS-84-9-1205.

Trenberth, Kevin E. and John T. Fasullo (2012). "Climate extremes and climate change: The Russian heat wave and other climate extremes of 2010". *J. Geophys. Res. Atmos.*, **117**, D17103. doi: 10.1029/2012JD018020.

Tu, Jien T., Chia Chou, and Pao Shin Chu (2009). "The abrupt shift of typhoon activity in the vicinity of Taiwan and its association with western North Pacific-East Asian climate change". *J. Climate*, **22**, 3617–3628. doi: 10.1175/2009JCLI2411.1.

Turner, Andrew G. and H. Annamalai (2012). "Climate change and the South Asian summer monsoon". *Nat. Clim. Chang.*, **2**, 587–595. doi: 10.1038/nclimate1495.

Vecchi, GA and DE Harrison (2002). "Monsoon breaks and subseasonal sea surface temperature variability in the Bay of Bengal". *J. Climate*, **15**, 1485–1493.

Von Storch, Hans and Francis W. Zwiers (1999). *Statistical Analysis in Climate Research.* Cambridge, UK: Cambridge University Press, 1999, 371–374.

Wang, Bin, Fei Huang, Zhiwei Wu, Jing Yang, Xiouhua Fu, and Kazuyoshi Kikuchi (2009). "Multi-scale climate variability of the South China Sea monsoon: A review". *Dyn. Atmos. Ocean.*, **47**, 15–37. doi: 10.1016/j.dynatmoce.2008.09.004.

Wang, Bin and LinHo (2002). "Rainy Season of the Asian-Pacific Summer Monsoon". *J. Climate*, **15**, 386–398.

Wang, Bin, Baoqiang Xiang, Juan Li, Peter J. Webster, Madhavan N. Rajeevan, Jian Liu, and Kyung-Ja Ha (2015). "Rethinking Indian monsoon rainfall prediction in the context of recent global warming". *Nat. Commun.*, **6**, 7154. doi: 10.1038/ncomms8154.

Wang, Chung-Chieh, George Tai-Jen Chen, Hsiao-Ling Huang, Richard E. Carbone, and Sau-Wa Chang (2012). "Synoptic Conditions Associated with Propagating and Nonpropagating Cloud/Rainfall Episodes during the Warm Season over the East Asian Continent". *Mon. Weather Rev.*, **140**, 721–747. doi: 10.1175/MWR-D-11-00067.1.

Wang, Ruifang, Liguang Wu, and Chao Wang (2011). "Typhoon track changes associated with global warming". *J. Climate*, **24**, 3748–3752. doi: 10.1175/JCLI-D-11-00074.1.

Wang, Shih-Yu and Robert R. Gillies (2012). "Influence of the Pacific quasi-decadal oscillation on the monsoon precipitation in Nepal". *Clim. Dyn.*, **40**, 95–107. doi: 10.1007/s00382-012-1376-2.

Wang, Y. J., H. Cheng, R. L. Edwards, Z. S. An, J. Y. Wu, C.-C. Shen, and J. A. Dorale (2001). "A High-Resolution Absolute-Dated Late Pleistocene Monsoon Record from Hulu Cave , China". *Science*, **294**, 2345–2348. doi: 10.1126/science.1064618.

Wang, Yongjin, Hai Cheng, R. Lawrence Edwards, Xinggong Kong, Xiaohua Shao, Shitao Chen, Jiangyin Wu, Xiouyang Jiang, Xianfeng Wang, and Zhisheng An (2008). "Millennial- and orbital-scale changes in the East Asian monsoon over the past 224,000 years." *Nature*, **451**, 1090–1093. doi: 10.1038/nature06692.

Wehner, Michael, Prabhat, Kevin A. Reed, Dáithí Stone, William D. Collins, and Julio Bacmeister (2015). "Resolution Dependence of Future Tropical Cyclone Projections of CAM5.1 in the U.S. CLIVAR Hurricane Working Group Idealized Configurations". *J. Climate*, **28**, 3905–3925. doi: 10.1175/JCLI-D-14-00311.1.

Westervelt, D. M., L. W. Horowitz, V. Naik, and D. L. Mauzerall (2015). "Radiative forcing and climate response to projected 21st century aerosol decreases". *Atmos. Chem. Phys. Discuss.*, **15**, 9293–9353. doi: 10.5194/acpd-15-9293-2015.

Wilks, David S. (2006). "Statistical methods in the atmospheric sciences". 2nd. Burlington, MA; London: Academic Press, 2006. Chap. Principal, 463–508.

Wu, Chi-Hua and Huang-Hsiung Hsu (2016). "Role of the Indochina Peninsula Narrow Mountains in Modulating the East Asian-Western North Pacific Summer Monsoon". *J. Climate*, doi: 10.1175/JCLI-D-15-0594.1.

Wu, Chi-Hua, Huang-Hsiung Hsu, and Ming-Dah Chou (2014). "Effect of the Arakan Mountains in the northwestern Indochina Peninsula on the late May Asian monsoon transition". *J. Geophys. Res. Atmos.*, **119**, 10769–10779. doi: 10.1002/2014JD022024.

Wu, Guoxiong, Yimin Liu, Bian He, Qing Bao, Anmin Duan, and Fei-Fei Jin (2012). "Thermal controls on the Asian summer monsoon." *Sci. Rep.*, **2**, 404. doi: 10.1038/srep00404.

Wu, Guoxiong, Yimin Liu, Qiong Zhang, Anmin Duan, Tongmei Wang, Rijin Wan, Xin Liu, Weiping Li, Zaizhi Wang, and Xiaoyun Liang (2007). "The Influence of Mechanical and Thermal Forcing by the Tibetan Plateau on Asian Climate". *J. Hydrometeor.*, **8**, 770–789. doi: 10.1175/JHM609.1.

Wu, Huawu, Xinping Zhang, Xiaoyan Li, Guang Li, and Yimin Huang (2015). "Seasonal variations of deuterium and oxygen-18 isotopes and their response to moisture source for precipitation events in the subtropical monsoon region". *Hydrol. Process.*, **29**, 90–102. doi: 10.1002/hyp.10132.

Wu, Renguang, Zhiping Wen, Song Yang, and Yueqing Li (2010). "An Interdecadal Change in Southern China Summer Rainfall around 1992/93". *J. Climate*, **23**, 2389–2403. doi: 10.1175/2009JCLI3336.1.

Xie, Shang-Ping, Kaiming Hu, Jan Hafner, Hiroki Tokinaga, Yan Du, Gang Huang, and Takeaki Sampe (2009). "Indian Ocean Capacitor Effect on Indo-Western Pacific Climate during the Summer following El Niño". *J. Climate*, **22**, 730–747.

Xie, Shang-Ping, Haiming Xu, N. H. Saji, Yuqing Wang, and W. Timothy Liu (2006). "Role of Narrow Mountains in Large-Scale Organization of Asian Monsoon Convection". *J. Climate*, **19**, 3420–3429.

Xin, Xiaoge, Rucong Yu, Tianjun Zhou, and Bin Wang (2006). "Drought in late spring of South China in recent decades". *J. Climate*, **19**, 3197–3206. doi: 10.1175/JCLI3794.1.

Xu, Weixin and Edward J. Zipser (2011). "Diurnal Variations of Precipitation, Deep Convection, and Lightning over and East of the Eastern Tibetan Plateau". *J. Climate*, **24**, 448–465. doi: 10.1175/2010JCLI3719.1.

Xu, Weixin, Edward J. Zipser, and Chuntao Liu (2009). "Rainfall Characteristics and Convective Properties of Mei-Yu Precipitation Systems over South China, Taiwan, and the South China Sea. Part I: TRMM Observations". *Mon. Weather Rev.*, **137**, 4261–4275. doi: 10.1175/2009MWR2982.1.

Xuan, Shouli, Qingyun Zhang, and Shuqing Sun (2011). "Anomalous midsummer rainfall in Yangtze River-Huaihe River valleys and its association with the East Asia westerly jet". *Adv. Atmos. Sci.*, **28**, 387–397. doi: 10.1007/s00376-010-0111-3.

Yang, S, KM Lau, and KM Kim (2002). "Variations of the East Asian Jet Stream and Asian-Pacific-American Winter Climate Anomalies." *J. Climate*, **15**, 306–325.

Yang, Shiling, Zhongli Ding, Yangyang Li, Xu Wang, Wenying Jiang, and Xiaofang Huang (2015). "Warming-induced northwestward migration of the East Asian monsoon rain belt from the Last Glacial Maximum to the mid-Holocene". *Proc. Natl. Acad. Sci.*, **112**, 13178–13183. doi: 10.1073/pnas.1504688112.

— (2016). "Reply to Yu et al.: Global temperature change as the ultimate driver of the shift in the summer monsoon rain belt in East Asia". *Proc. Natl. Acad. Sci.*, doi: 10.1073/pnas.1601768113.

Yang, Xiaoxin, Baiqing Xu, Wei Yang, and Dongmei Qu (2011a). "The Indian monsoonal influence on altitude effect of $\delta^{18}O$ in surface water on southeast Tibetan Plateau". *Sci. China Earth Sci.*, **55**, 438–445. doi: 10.1007/s11430-011-4342-7.

Yang, Xiaoxin, Tandong Yao, Wulin Yang, Wusheng Yu, and Dongmei Qu (2011b). "Co-existence of temperature and amount effects on precipitation δ 18 O in the Asian monsoon region". *Geophys. Res. Lett.*, **38**, L21809. doi: 10.1029/2011GL049353.

Yao, Tandong, Valerie Masson-Delmotte, Jing Gao, Wusheng Yu, Xiaoxin Yang, Camille Risi, Christophe Sturm, Martin Werner, Huabiao Zhao, You He, and Wei Ren (2013). "A review of climatic controls on δ^{18}O in precipitation over the Tibetan Plateau: Observations and simulations". *Rev. Geophys.*, **51**, 525–548. doi: 10.1002/rog.20023.

Yao, TanDong, Hang Zhou, and XiaoXin Yang (2009). "Indian monsoon influences altitude effect of δ18O in precipitation/river water on the Tibetan Plateau". *Chinese Sci. Bull.*, **54**, 2724–2731. doi: 10.1007/s11434-009-0497-4.

Yasunari, Tetsuzo and Takeshi Miwa (2006). "Convective cloud systems over the Tibetan Plateau and their impact on meso-scale disturbances in the Meiyu/Baiu frontal zone - a case study in 1998". *J. Meteorol. Soc. Japan*, **84**, 783–803.

Yatagai, Akiyo, Kenji Kamiguchi, Osamu Arakawa, Atsushi Hamada, Natsuko Yasutomi, and Akio Kitoh (2012). "APHRODITE: Constructing a Long-Term Daily Gridded Precipitation Dataset for Asia Based on a Dense Network of Rain Gauges". *Bull. Am. Meteorol. Soc.*, **93**, 1401–1415. doi: 10.1175/BAMS-D-11-00122.1.

Yeh, Tu-Cheng, Shih-Yen Dao, and Mei-Ts'un Li (1959). "The Abrupt Change of Circulation over the Northern Hemisphere during June and October". *The Atmosphere and the Sea in Motion.* Ed. by Bolin, B. Rockefeller Institute Press, 1959, 249–267.

Yim, So-Young, Bin Wang, and MinHo Kwon (2013). "Interdecadal change of the controlling mechanisms for East Asian early summer rainfall variation around the mid-1990s". *Clim. Dyn.*, **42**, 1325–1333. doi: 10.1007/s00382-013-1760-6.

Yin, Maung Tun (1949). "Synoptic-aerologic study of the onset of the summer monsoon over India and Burma". *J. Meteorol.*, **6**, 393–400.

Yoon, Jin-Ho and Tsing-Chang Chen (2005). "Water vapor budget of the Indian monsoon depression". *Tellus A*, **57A**, 770–782.

Yu, Rucong, Jian Li, Weihua Yuan, and Haoming Chen (2010). "Changes in characteristics of late-summer precipitation over eastern China in the past 40 years revealed by hourly precipitation data". *J. Climate*, **23**, 3390–3396.

Yu, Rucong, Bin Wang, and Tianjun Zhou (2004). "Tropospheric cooling and summer monsoon weakening trend over East Asia". *Geophys. Res. Lett.*, **31**, L22212.

Yu, Rucong and Tianjun Zhou (2007). "Seasonality and Three-Dimensional Structure of Interdecadal Change in the East Asian Monsoon". *J. Climate*, **20**, 5344–5355.

Yu, Shaocai, Pengfei Li, Liqiang Wang, Peng Wang, Si Wang, Shucheng Chang, Weiping Liu, and Kiran Alapaty (2016). "Anthropogenic aerosols are a potential cause for migration of the summer monsoon rain belt in China". *Proc. Natl. Acad. Sci.*, doi: 10.1073/pnas.1601104113.

Zhang, Renhe, Akimasa Sumi, and Masahide Kimoto (1999). "A Diagnostic Study of the Impact of El Niño on the Precipitation in China". *Adv. Atmos. Sci.*, **16**, 229–241.

Zhang, Yuwei, Donghai Wang, Panmao Zhai, Guojun Gu, and Jinhai He (2013). "Spatial Distributions and Seasonal Variations of Tropospheric Water Vapor Content over the Tibetan Plateau". *J. Climate*, **26**, 5637–5654. doi: 10.1175/JCLI-D-12-00574.1.

Zhao, Ping, Song Yang, and Rucong Yu (2010). "Long-Term Changes in Rainfall over Eastern China and Large-Scale Atmospheric Circulation Associated with Recent Global Warming". *J. Climate*, **23**, 1544–1562. doi: 10.1175/2009JCLI2660.1.

Zhao, Tianbao and Akiyo Yatagai (2013). "Evaluation of TRMM 3B42 product using a new gauge-based analysis of daily precipitation over China". *Int. J. Climatol.*, **34**, 2749–2762. doi: 10.1002/joc.3872.

Zhou, Tianjun, Daoyi Gong, Jian Li, and Bo Li (2009). "Detecting and understanding the multi-decadal variability of the East Asian Summer Monsoon - Recent progress and state of affairs". *Meteorol. Zeitschrift*, **18**, 455–467. doi: 10.1127/0941-2948/2009/0396.

Zhou, Tianjun, Rucong Yu, Haoming Chen, Aiguo Dai, and Yang Pan (2008). "Summer Precipitation Frequency, Intensity, and Diurnal Cycle over China: A Comparison of Satellite Data with Rain Gauge Observations". *J. Climate*, **21**, 3997–4010.

Zickfeld, K., B. Knopf, V. Petoukhov, and H. J. Schellnhuber (2005). "Is the Indian summer monsoon stable against global change?" *Geophys. Res. Lett.*, **32**, L15707.

Zou, Xukai and Fumin Ren (2015). "Changes in Regional Heavy Rainfall Events in China during 1961-2012", **32**, 704–714. doi: 10.1007/s00376-014-4127-y.1.